Estimating Reflection Coefficients: Theory and Application to Microseismic Waveform Data

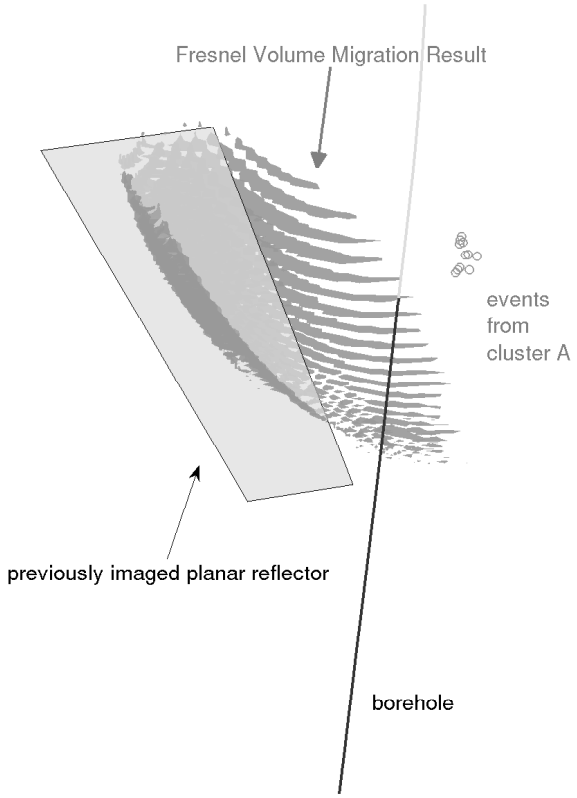

vorgelegt von

Dipl.-Phys. Antonia Oelke

Berlin 2016

Dissertation zur Erlangung des Grades
Doktor der Naturwissenschaften
am Fachbereich Geowissenschaften,
Fachrichtung Geophysik, der Freien Universität Berlin

Gutachter:	Prof. Dr. Serge A. Shapiro Prof. Dr. Marco Bohnhoff
Tag der Abgabe:	27.09.2016
Tag der Disputation:	29.11.2016

Erklärung

Hiermit versichere ich, dass ich die vorliegende Arbeit selbstständig angefertigt und keine ausser der angegebenen Quellen und Hilfsmittel verwendet habe.

Zusammenfassung

Wellenformen mikroseismischer Beben enthalten eine Fülle an Informationen über den Untergrund. Dieser lässt sich durch die Auswertung und Analyse der Beben hinsichtlich verschiedener Eigenschaften detailliert beschreiben. In der vorliegenden Arbeit zeige ich, dass fluid-gefüllte Klüfte, welche beim *Hydraulic Fracturing*, bei der Erschließung von Geothermie-Reservoiren und in natürlichen Riss-Systemen auftreten, hohe Reflektivität hervorrufen können.

In der vorliegenden Arbeit präsentiere ich ein Modell, welches diese relativ signifikanten Reflexionen erklärt. Eine zwischen zwei elastischen Halbräumen eingebettete dünne Fluid-Schicht beschreibt dabei den Hydrofrac. Ich leite mit diesem Modell die analytische Lösung für den Reflexionskoeffizienten als Funktion der elastischen Parameter des umgebenden Gesteins sowie des Fluids her. Diese analytische Lösung wird mithilfe numerischer Modellierung von Wellenfeldern bestätigt.

In der vorliegenden Arbeit schlage ich ein Schema vor, nach welchem Reflexionskoeffizienten aus mikroseismischen Wellenformen extrahiert werden können und demonstriere diese Arbeitsschritte an drei realen Datensätzen. In dem ersten Datenbeispiel evaluiere ich Mikroerdbeben des Basel Enhanced Geothermal System. Diese Beben treten in einem homogenen und isotropen Gestein auf und werden auch in dieser Gesteins-Schicht registriert. Ich bilde die von einem Ereignis-Cluster beleuchtete Struktur im Untergrund ab und erhalte so Informationen zur Lage des Reflektors. Aus den Wellenformen schätze ich den *apparent* (scheinbaren, lokal gemessenen) Reflexionskoeffizienten ab. Mit dem Wissen zur Lage des Reflektors berechne ich Korrektur-Terme, welche die unterschiedlichen Strahl-Laufwege der direkten und der reflektierten Welle berücksichtigen. Diese unterschiedlichen Laufwege resultieren in unterschiedlicher sphärischer Divergenz (räumliche Ausbreitung) und Dämpfung. Auch die unterschiedlichen Amplituden aufgrund der verschiedenen Abstrahlrichtungen von dem Ereignis zum Empfänger beziehungsweise zum Reflektor werden berücksichtigt. Es ergibt sich ein *true* (wahrer) Reflexionskoeffizient von $R = 0.13$. Unter der Annahme, dass es sich bei dem abgebildeten Reflektor um eine fluid-gefüllte Kluft handelt, lässt sich seine Mächtigkeit abschätzen. Aus dem Vergleich mit dem theoretisch zu erwartenden Reflexionskoeffizienten schließe ich auf eine effektive Klufthöhe von 0.05 m. Anschließend lokalisiere ich mit der Auswertung weiterer

Ereignis-Cluster zwei zusätzliche Strukturen in der Nähe des Bohrlochs und weise diesen Strukturen jeweils einen Reflexionskoeffizienten und damit eine bestimmte Mächtigkeit zu. Zusätzlich kann ich das Reservoir durch eine abgeleitete Berechnung der *normal compliance* zu $|\eta_{\mathrm{N}}| = 2.06 \cdot 10^{-11} \frac{m}{Pa}$ mit anderen Reservoiren vergleichen.

Im zweiten Realdaten-Beispiel wende ich die oben genannten Arbeitsschritte auf die Wellenform eines mikroseismischen Bebens an der San Andreas Störung an. Dieses Beben wurde an einer Kette von Bohrloch-Geophonen registriert. Ich vereinfache das heterogene isotrope Geschwindigkeitsmodell. Damit kann ich einen vorläufigen Reflexionskoeffizienten von $R = 0.31$ abschätzen. Auch hier wurden die Amplitudenveränderungen aufgrund der unterschiedlichen räumlichen Ausbreitung, des Einflusses des Herdmechanismus und der unterschiedlichen Dämpfung bereits korrigiert. Der vorläufigen Reflexionskoeffizient lässt mich auf eine Kluft-Mächtigkeit von $1 - 7$ m schließen. Um das Ergebnis besser einzugrenzen, also die Mächtigkeit genauer abzuschätzen, müssten die Wellenfelder weiterer Ereignisse mit dem genauen Geschwindigkeitsmodell ausgewertet werden.

Das dritte Realdaten-Beispiel stammt aus dem Horn River Basin. Hier zeige ich eine Vorstudie um die Wellenfelder von Ereignissen bezüglich ihrer Reflexionskoeffizienten auszuwerten, die in einem heterogenen und anisotropen Gestein registriert wurden. Ich untersuche mithilfe numerischer Simulationen den Einfluss von Anisotropie sowie starker Kontraste der elastischen Parameter des Gesteins auf die Wellenausbreitung. Ich zeige, dass mit den gegeben Parametern ein nicht zu vernachlässigendes *Shear Wave Splitting* auftritt und die Kontraste der elastischen Parameter zu Reflexionen und Konversionen führen. Diese mitunter signifikanten Signale innerhalb der Wellenformen dürfen bei der Auswertung von Reflexionskoeffizienten nicht mit den Reflexionen an fluid-gefüllten Klüften verwechselt werden.

Meine Arbeit zeigt, dass an fluid-gefüllten Klüften hohe Reflexionskoeffizienten auftreten können. Die in meiner Arbeit vorgestellten Arbeitsschritte zur Abschätzung und Auswertung der Reflexionskoeffizienten sind auf einfache Fallbeispiele bereits anwendbar und auch in komplexeren Anordnungen durchführbar.

Summary

Microseismic data contain a great deal of subsurface information. This subsurface can be described through a careful analysis of the events and their wavefields. In this work, I show that the presence of fluids in hydraulic fracturing experiments, geothermal exploitation, or fluid pathways at natural fault systems, can result in regions of high reflectivity. Appropriate analysis of reflected seismic signals yields additional information about the subsurface. I present an approach for quantitative evaluation of reflections within microseismic waveforms, which allows us to better characterize the subsurface.

I present a theoretical model, which explains that the presence of fluid within a fracture can produce relatively high reflection coefficients. A thin fluid layer represents a feasible model of a hydraulic fracture and I give an analytical solution for the reflection coefficient as a function of the elastic parameters of the fracture itself and the surrounding rock matrix. I verify this theoretical solution through numerical modeling of reflections produced by a single fluid layer.

I demonstrate the theoretical approach for the extraction of reflection coefficients from microseismic waveform data, and proceed to apply this approach to three real data sets. In the first example I evaluate event clusters from the Basel Enhanced Geothermal System, which occur and are recorded in a homogeneous and isotropic granitic rock environment. In this relatively 'simple' acquisition geometry, I evaluate one example cluster. I extract an apparent reflection coefficient directly from the waveforms. I then image the reflected waveforms and locate the structure which is illuminated by the cluster. From the locations of the structure I calculate correction terms which account for the changes in amplitude due to different geometrical spreading and attenuation of the direct and reflected wave. I also account for changes in amplitude caused by the double couple radiation pattern of the event. Amplitudes from the event to the receiver are typically different than from the event to the reflector. By including these corrections I find the true reflection coefficient to be $R = 0.13$. Through my theoretical analysis, this value yields an effective fracture width of 0.05 m. Furthermore, I generate a map of illuminated structures in the vicinity of the borehole from the evaluation of two other clusters and assign a value of reflectivity and effective fracture width to each structure. The normal compliance of the rock matrix can be computed from these quantities to be

$|\eta_{\mathrm{N}}| = 2.06 \cdot 10^{-11} \frac{m}{Pa}$ which, in comparison to other studies, is a reasonable value.

In the second real data example I apply the workflow to a single microseismic event recorded at the San Andreas Fault by a receiver array. I simplify the heterogeneous velocity model and obtain a preliminary estimate for the reflection coefficient of $R = 0.31$. Here the correction terms accounting for the different travel paths of direct and reflected waves are already included. This value yields a fracture width of $1 - 7$ m. In order to better constrain the width, I suggest evaluation of further events, using the full heterogeneous velocity model.

In the last real data example I present a pre-study with the aim to extract reflection coefficients from wave fields recorded in a heterogeneous anisotropic environment at the Horn River Basin. This study is required in order to interpret the complex wave field properly, and to identify reflections from hydraulic fractures. I numerically investigate the influence of anisotropy and velocity interfaces. The numerical modelling shows that due to anisotropy a strong shear wave splitting exists. Additionally strong contrasts of elastic properties in the layered velocity model cause reflections and conversions. Both shear wave splitting, reflections and conversions at velocity contrasts generate additional strong signals in the recorded wave field and should not to be mixed with reflections at hydraulic fractures.

This work shows that it is feasible to extract and interpret reflection coefficients at hydraulic fractures. The procedure outlined herein demonstrably works for simple cases, and is also applicable to more complex experiments.

Contents

1. Introduction

Earthquakes occur every day. Despite the damage that they can cause, they provide us with a great deal of information about the earth's interior on a global, regional, and local scale. For example, we learn about the velocity distribution at depth, about structures in the subsurface, and about processes at depth. With increasingly sophisticated technology the detection threshold for events has decreased, and so the detection rate of small events has increased. As a consequence, the field of 'microseismicity' has obtained growing attention, especially in the context of geothermal or hydrocarbon exploitation. Microseismic events can be natural earthquakes, but are also often induced by fluid-injections, where fluids are injected into the rock in order to increase the hydraulic permeability. The recording and analysis of microseismicity heavily contributes to subsurface characterisation.

Shapiro et al. (2002) use the seismicity-based reservoir characterisation approach in order to describe the large-scale permeability of the reservoir. The authors state that randomly distributed near-failure equilibrium locations within the rock react to small pore-pressure perturbations by releasing a microseismic event. These pore-pressure perturbations can be caused by fluids injected into the rock. The pore-pressure and thus the triggering front propagates like a diffusive process. This means that the spatio-temporal evolution of the microseismicity can be used to reconstruct the permeability tensor, which describes the large-scale permeability of the reservoir. That the seismicity is triggered by the relaxation process of stress and pore-pressure perturbations is shown by Hajati et al. (2015). The authors analyze inter-event times and injected fluid volumes to find this relation. They further suggest that no aftershock triggering needs to be included in the statistical model, since the stress transfer for triggering subsequent events is insignificant. The occurrence of microseismicity is related to elastic rock heterogeneity and strongly correlates to rock sections with a low Poisson's ratio and high Young's modulus, as reported by Langenbruch and Shapiro (2015). The authors have compared the occurrence of microseismicity to rock heterogeneity as measured by borehole logging. Another approach to reservoir characterisation using the occurrence of seismicity is presented by Shapiro et al. (2010), whereby data from different geothermal and hydrocarbon reservoirs has been evaluated. The authors show that fluid-induced microseismicity follows Poisson statistics and is controlled by the injection rate of the fluid and a site-dependent seismogenic

index. The above mentioned studies provide methods to assess seismic risk.

The analysis of microseismic waveforms can also resolve structures within a reservoir. Stuermer et al. (2011) analyze waveform similarity between different events. The authors introduce the measure of correlation of seismic traces and the measure of inter-event S-P travel time differences, and identify clusters of seismic events without prior knowledge of the event locations. They state that, if the waveform similarity of an event pair is high even though their relative S-P travel time difference is high, the events occur within the same geological regime. Identification of multiplets (a number of events with high waveform similarity) allows the identification of geological structures. Kummerow (2010) provides an algorithm to perform a high precision microseismic event location which is based on waveform similarities. The structure of the microseismic event cloud provides clues to the geological structure. Using an automatic, iterative arrival time optimization and waveform similarities, Kummerow et al. (2012) compute local Vp/Vs ratios in the vicinity of the borehole of the Basel geothermal reservoir. Reshetnikov et al. (2015) use microseismic events as passive seismic sources. They apply a focusing depth migration algorithm and image structures in the vicinity of the borehole at the same Basel reservoir with high precision. These structures with high reflectivity are interpreted as fluid path ways: natural re-opened fractures or newly opened fractures.

There arise two main questions which I will address in this thesis: (i) Do hydraulic fractures, which are much thinner than the wavelength of the illuminating event, produce detectable reflected signals, and (ii) If so, can we quantitatively describe the value of reflectivity. In this thesis I show that high reflectivity can occur at hydraulic fractures. I present an approach of a quantitative evaluation of reflections within microseismic waveforms. Imaged zones of high reflectivity are analyzed quantitatively. One can extract reflection coefficients from microseismic waveform data and evaluate the reflection coefficient in terms of fracture properties and thus reservoir properties. In this thesis I present a theoretical model which explains even relatively high reflection coefficients at hydraulic fractures, and I confirm the theoretical description by numerical modeling. I extract reflection coefficients from real microseismic waveform data, and interpret the reflections in terms of fracture width. For this I suggest the following workflow:

- Identification of reflected phases within waveforms
- Imaging of reflected phases
- Calculation of *apparent* reflection coefficient
- Correction for geometrical spreading, radiation pattern, and attenuation $\rightarrow$ *true* reflection coefficient

- Comparison to theoretical reflection coefficient
  $\rightarrow$ reflector width

The real data examples are from the different areas at which microseismicity is of scientific, economic, and public interest. I evaluate data from an active plate boundary, a geothermal reservoir, and a shale gas reservoir. For each of these data sets, I am able to extract, and interpret significant reflection signals.

In Chapter 2 I introduce the theoretical background. A thin fluid layer, embedded between two elastic half spaces, represents a feasible model of a hydraulic fracture. I derive an analytical formula of the reflection coefficient as a function of the elastic parameters of the fracture itself and the surrounding rock matrix. I then discuss the properties of the reflection coefficient in the context of microseismicity. I show that high values of reflectivity can occur even at fractures where the width is significantly smaller than the wavelength of the illuminating event. The reflection coefficient for a fracture at slip contact is compared to the Linear Slip Model.

The theoretical description is also confirmed by numerical modeling results as I show in Chapter 3. Using a Finite Difference algorithm I compute the wave field that is reflected by a thin fluid layer. I show in a simulation that the zero incidence reflection coefficient, extracted from the modeled wave field, is in agreement with the theoretical value. In another simulation, I find that the angle dependent reflection coefficient is in agreement with the theoretical predicted value. Finally, I show that a plane wave simplification sufficiently describes the wave front of a microseismic event, for our purposes.

In the following chapters, Chapters 4, 5, and 6, I estimate the reflection coefficients from waveform data recorded at a geothermal reservoir, a natural fault zone, and a shale reservoir. In the beginning of each chapter I briefly motivate why this kind of data is of public, economic, and scientific interest. In Chapter 4 I evaluate event clusters from the Basel Enhanced Geothermal System which occur and are recorded in a homogeneous and isotropic granite. In this relatively 'simple' acquisition geometry, I demonstrate the reflection coefficient estimation process in detail. The procedure is applied to two other clusters and I generate a map of illuminated structures in the vicinity of the borehole, and assign a value of reflectivity and effective fracture width to each structure. Using the Linear Slip Model, I compute the normal compliance of the rock matrix, and find it to be a reasonable value.

In Chapter 5 I apply the workflow to a single microseismic event recorded at the San Andreas Fault by a receiver array. I simplify the heterogeneous velocity model and obtain a preliminary reflection coefficient. In order to infer an effective fracture (fault) width further events must be evaluated in a more realistic (heterogeneous) velocity model.

Chapter 6 serves as a pre-study in order to extract reflection coefficients from wave fields recorded in a heterogeneous anisotropic environment at the Horn River Basin. I numerically investigate the influence of anisotropy and velocity interfaces. This pre-study is required in order to interpret the complex wave field and identify reflections from hydraulic fractures which are not to be confused with splitting shear waves or signatures from velocity interfaces.

A summary and a conclusion are given in the last part of this thesis, in Chapter 7.

2. Theory: Reflection Coefficients from a Fluid-Filled Fracture

In this chapter I analyze the angle-dependent reflectivity of microseismic wavefields at a hydraulic fracture, which I model as an ideal thin fluid layer embedded in an elastic, isotropic solid rock. I present full analytical solutions for the reflections of an incident P wave, the P-P and P-S reflection coefficients, as well as for an incident S wave, the S-S and S-P reflection coefficients.

The rather complex analytical solutions are then approximated and I show that these zero-thickness limit approximations are in good agreement with the Linear Slip Model, representing a fracture at slip contact. I later compare the analytical solutions for the P-P reflections with synthetic data that is derived using Finite Difference modeling and find that the modeling confirms the theoretical results.

I find that for typical parameters which are found in microseismic monitoring of hydraulic fracturing: a layer thickness of $h = 0.001 - 0.01$ m and frequencies of $f = 50 - 400$ Hz, the reflection coefficients depend on the Poisson's ratio. Furthermore the reflection coefficients of an incident S wave are remarkably high.

My theoretical results suggest that it is feasible to image hydraulic fractures using microseismic events as a source and to solve the inverse problem and resolve the extracted reflection coefficient for the fracture width. This means to interpret reflection coefficients extracted from microseismic data in terms of reservoir properties.

2.1 Introduction

In the understanding of subsurface structures, especially in reservoirs, hydraulic fractures play a significant role. Several authors have used microseismic events in order to image potential fractures. Soma et al. (2000) use the acoustic emission reflection method in time-frequency domain and estimate the subsurface structure at an artificial geothermal reservoir in Soultz-sous-Forêts, France. Examination of hodograms of S to S wave reflections provides

images of the subsurface structures. Using microseismic data from the Basel geothermal reservoir, Dyer et al. (2008) derive a velocity model and locate microseismic events. Potential reflections in the microseismic data from these located events are migrated and afterward stacked, separately for P and S waves. Based on the consistency between P and S wave images they suggest the presence of several reflectors.

Investigating natural faults, Chavarria et al. (2003) use Kirchhoff Depth Migration to reflection seismic data from microseismic events at the San Andreas Fault. In addition to illuminating the surface fault-trace, they image other scattering modes which they interpret as the presence of cracks or fluid. Deploying the Fresnel Volume Migration approach and using microseismic events, Reshetnikov et al. (2010a) image the subsurface region at the San Andreas Fault with a high resolution. Reshetnikov et al. (2010b) use the same passive seismic imaging approach in order to construct subsurface images at the German Continental Deep Drilling program (KTB). They observe relatively high reflectivity, thus high reflection coefficients. Considering the general properties of the experimental site, a possible explanation for such high reflection coefficients might be the reflection at hydraulic fractures.

Groenenboom and Fokkema (1998) use a thin fluid layer as a model for a hydraulic fracture. They indirectly measure the width of the fracture by evaluating the dispersion of the transmitted signal. They model waveforms by convolving the original source signal with the transmission response. In their conclusion, it is possible to make assumptions about the fluid layer's thickness, even though it is beyond the classical limit of resolution. Groenenboom and Fokkema (1998) verify their results by small scale laboratory experiments in MHz range. They compare their theory to the Linear Slip Model (LSM). The Linear Slip Model, introduced by Schoenberg (1980), is commonly used in ultrasonic non-destructive material property evaluation (Nagy, 1992) as well as in seismology over fractured rocks (Grechka et al., 2000) to explain effects at fluid-filled fractures.

In the frame of wave propagation at a thin layer numerous papers already exist. For example Krauklis (1962) introduced the slow fluid wave, recently referred to as Krauklis wave (Korneev et al., 2012), which has a large amplitude, high dispersion and propagates with low velocity at low frequencies. Korneev (2010) explores the Krauklis wave within a viscous fluid crack in an elastic medium. Quintal et al. (2009) investigate the reflectivity of a viscoelastic layer for the 1-D case and confirm the theoretical prediction with numerical results. For this case, they show that the contrast in attenuation yields significant reflections. In his paper, Fehler (1982) assumes a thin fluid layer to be filled with a viscous fluid and analyzes the interaction of seismic waves with this layer.

I show that high reflectivity may occur at hydraulic fractures and thus by

reflection seismic imaging microseismic data, it is possible to image hydraulic fractures. Considering hydraulic fractures, the other main goal of this work is to create a basis of inferring for fracture properties from the reflection coefficient. This means, using the knowledge of source and reflector location, and knowledge of a microseismic source mechanism, I can estimate the reflection coefficients. I can then interpret these reflection coefficients in terms of reservoir and fracture properties.

In my model the hydraulic fracture is represented by a thin fluid layer filled with water. I derive an analytical solution which describes the reflection coefficients for an incident P wave, the P-P and P-S reflection coefficients, as well as for an incident S wave, the S-S and S-P reflection coefficients, and show that under certain circumstances strong reflections may occur.

First, I illustrate the derivation of an analytical solution for the reflection coefficients of any incident wave that propagates through a thin fluid layer embedded in an elastic solid. I then give the full solution for all possible reflections (P-P, P-S, S-P, S-S) and analyze their reflection coefficients considering different parameters such as layer thickness or frequency as they occur in microseismic context. In the paragraph 'Validity' I comment on why I can in this case neglect viscosity and state the frequency range of the derived formulas. Furthermore I derive an approximation for the reflection coefficients at a zero thickness limit, representing a fracture with slip contact. This will be discussed and compared to the Linear Slip Model.

In the Chapter 3 I then show reflection coefficients from synthetic data that has been calculated using a Finite Difference (FD) method (Saenger et al., 2000). Reflections at a thin fluid layer are modeled for incident plane P waves at zero incidence angle in order to show the validity of the modeling approach. In a next step the plane wave is replaced by a spherical (cylindrical) wave emitted by an explosion source. Evenly distributed receivers allow to resolve angle dependency of the recorded signal. The synthetic data is evaluated with respect to reflection coefficients and I show that the plane wave approach is valid. By that I also show that it is justified to use plane wave reflection coefficients to interpret data from real microseismic events.

2.2 Analytical Solutions for Reflection Coefficients

The simplest model to describe a hydraulic fracture is a thin layer filled with an ideal fluid. The fluid layer is embedded between two solid elastic half spaces. In the following, these half spaces are assumed to have identical properties.

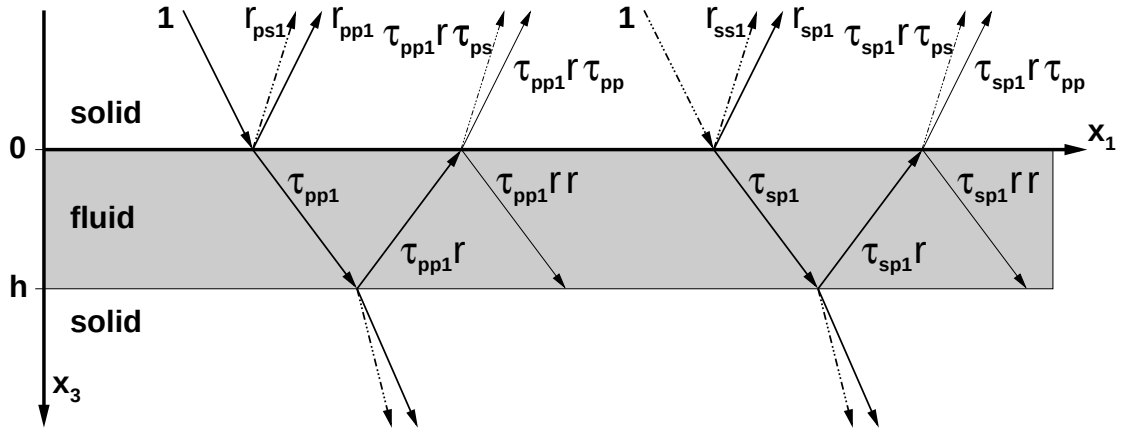

Figure 2.1: *A thin fluid layer of thickness h is embedded between two identical solid elastic half spaces. Illustrate here on the left is the incident P wave and on the right the incident S wave. The figure shows multiple reflections within the fluid layer, labelled corresponding to their origin.*

The quantities describing the solid media are their P wave velocity v_{p}, their S wave velocity v_{s} and their density ρ_{s}. Analogously, the velocity within the fluid v_{f} and the density ρ_{f} are describing the ideal fluid.

2.2.1 Theory

A straightforward way to derive the formulas for each reflection coefficient is to find the wavefield within each medium and use the boundary conditions, as the continuity of stress, traction, and the wavefield, to solve for the reflection coefficients. Per definition the reflection coefficient is the ratio of the displacement or the energy of the reflected wave to the corresponding quantity of the incident wave. However, considering the displacement, an alternative derivation for the reflection coefficient is sketched in the following.

I consider every reflection and refraction at an interface as a separate event and derive the resulting reflected wave as a superposition of reflections and refractions at single interfaces as sketched in Figure 2.1.

I assume that the incident harmonic wave has an amplitude equal to unity and that an (inclined) plane wave is propagating in positive x_3-direction. At the upper interface of the fluid layer, a P and S wave are reflected, and also a P wave is transmitted. Then this transmitted P wave is partly reflected again at the lower boundary of the fluid layer, such that this time at the first interface a P and S wave are transmitted while a P wave is reflected again and so on.

I obtain the amplitude of each wave by multiplication with the reflection or refraction coefficient, corresponding to the type of event as sketched for an

incident P wave and an incident S wave in Figure 2.1. If a wave experiences multiple reflections within the fluid layer, I have to take into account the time delay for the P wave within the fluid to travel from the first interface to the second and back. This is expressed by the complex exponent:

$$e^{\mathrm{i}\omega 2h\beta_{\mathrm{f}}}, \tag{2.1}$$

where β_{f} denotes the vertical slowness within the fluid, ω is the angular frequency (recall that the frequency f is related by $\omega = 2\pi f$), and h the fracture width.

The full reflected P wavefield of the incident P wave, thus the reflection coefficient R_{pp}, can be written as a sum of P waves which are multiply reflected within the fluid layer. The resulting geometric series can be further simplified, so the P-P reflection coefficient R_{pp} is found to be:

$$\begin{aligned} R_{\mathrm{pp}} &= r_{\mathrm{pp1}} + \tau_{\mathrm{pp1}}\tau_{\mathrm{pp}} r e^{\mathrm{i}\omega 2h\beta_{\mathrm{f}}} + \tau_{\mathrm{pp1}}\tau_{\mathrm{pp}} r r^2 e^{\mathrm{i}\omega 4h\beta_{\mathrm{f}}} + \dots \\ &= r_{\mathrm{pp1}} + \tau_{\mathrm{pp1}}\tau_{\mathrm{pp}} r \sum_{j=1}^{\infty} (r^2)^{j-1} e^{2\mathrm{i}\omega h\beta_{\mathrm{f}} j} \\ &= r_{\mathrm{pp1}} + \tau_{\mathrm{pp1}}\tau_{\mathrm{pp}} r e^{2\mathrm{i}\omega h\beta_{\mathrm{f}}} (1 - r^2 e^{2\mathrm{i}\omega h\beta_{\mathrm{f}}})^{-1}. \end{aligned} \tag{2.2}$$

Here r_{pp1} denotes the P-P reflection at a solid fluid interface, while the transmission coefficient at this interface is represented by τ_{pp1} and the transmission coefficient from a fluid to solid transmission is given by τ_{pp}. The reflection coefficient of the P wave at the fluid solid interface is denoted by r. Similarly to the above, the P-SV reflection coefficient R_{ps} is found. In the case of an incident S wave, the same method gives the reflection coefficients R_{sp} and R_{ss}; however, one has to keep in mind that for an incident P wave, the horizontal slowness is $\zeta_{\mathrm{p}} = v_{\mathrm{p}}^{-1} \sin\theta$ while for an incident S wave it is $\zeta_{\mathrm{s}} = v_{\mathrm{s}}^{-1} \sin\theta$ and thus also vertical slowness and coefficients at single interfaces change. If I replace the single interface reflection and transmission coefficients by their respective definitions, I can further simplify the reflection coefficients to the following form:

$$R_{\mathrm{pp}} = 1 - \frac{(\beta_{\mathrm{s}}^2 - \zeta_{\mathrm{p}}^2)^2}{R} \left[1 + \frac{r(1 - e^{2\mathrm{i}\omega h\beta_{\mathrm{f}}})}{1 - r^2 e^{2\mathrm{i}\omega h\beta_{\mathrm{f}}}}\right], \tag{2.3}$$

$$R_{\mathrm{ps}} = \frac{2v_{\mathrm{p}}\beta_{\mathrm{p}}\zeta_{\mathrm{p}}(\beta_{\mathrm{s}}^2 - \zeta_{\mathrm{p}}^2)}{v_{\mathrm{s}} R} \left[1 + \frac{r(1 - e^{2\mathrm{i}\omega h\beta_{\mathrm{f}}})}{1 - r^2 e^{2\mathrm{i}\omega h\beta_{\mathrm{f}}}}\right], \tag{2.4}$$

$$R_{\mathrm{sp}} = -\frac{2v_{\mathrm{s}}\beta_{\mathrm{s}}\zeta_{\mathrm{s}}(\beta_{\mathrm{s}}^2 - \zeta_{\mathrm{s}}^2)}{v_{\mathrm{p}} R} \left[1 + \frac{r(1 - e^{2\mathrm{i}\omega h\beta_{\mathrm{f}}})}{1 - r^2 e^{2\mathrm{i}\omega h\beta_{\mathrm{f}}}}\right], \tag{2.5}$$

$$R_{\mathrm{ss}} = \frac{4\beta_{\mathrm{s}}\beta_{\mathrm{p}}\zeta_{\mathrm{s}}^2}{R} \left[1 + \frac{r(1 - e^{2\mathrm{i}\omega h\beta_{\mathrm{f}}})}{1 - r^2 e^{2\mathrm{i}\omega h\beta_{\mathrm{f}}}}\right] - 1, \tag{2.6}$$

where ζ_i denotes the horizontal slowness which is constant on the contrary to

the vertical slowness $\beta_i = \sqrt{\frac{1}{v_i^2} - \zeta_i^2}$. R is the Rayleigh function:

$$r = (a-b)(a+b)^{-1}, \quad a = \rho_{\mathrm{s}} v_{\mathrm{s}}^4 \beta_f R, \quad b = \rho_{\mathrm{f}} \beta_{\mathrm{p}}, \tag{2.7}$$

$$R = \left(\frac{1}{v_{\mathrm{s}}^2} - 2\zeta^2\right)^2 + 4\beta_{\mathrm{p}}\beta_{\mathrm{s}}\zeta^2. \tag{2.8}$$

2.2.2 Validity

In principle the above derived formulas 2.3 – 2.6 are valid for all frequencies. However, since the main goal is to investigate reflections from microseismic events, I restrict myself to frequencies between $f = 50 - 400$ Hz.

This frequency restriction becomes crucial when justifying the assumption of a non-viscous fluid filler. In my model, I assume an ideal water fluid layer to describe a hydraulic fracture. Of course, in nature fillers are viscous. In this case one has to has to consider different wave types within the fluid. Following Biot (1956) the ideal fluid is justified though. Considering my restriction of frequencies in the range from $f = 50 - 400$ Hz, the fracture width h is still big enough so that it is in the order of the quarter wavelength of the boundary layer and Poiseuille flow breaks down. Therefore I don't have to consider reflections at a viscous fluid filler.

2.2.3 Reflection Coefficients in the Microseismic Context

In this section I will discuss the properties of the reflection coefficients in microseismic context. 'Microseismic context' refers to typical properties of passive seismic data recorded at reservoirs or in hydraulic fracturing experiments. In the following I assume the P wave velocity to be $v_{\mathrm{p}} = 4500$ m/s in the solid at a density of $\rho_{\mathrm{s}} = 3000\ \mathrm{kg/m^3}$. The S wave velocity is varied from $v_{\mathrm{s}} = 1500 - 3000$ m/s. The ideal fluid is represented by water with a P wave velocity of $v_{\mathrm{f}} = 1500$ m/s and a density of $\rho_{\mathrm{f}} = 1000\ \mathrm{kg/m^3}$.

The waves emitted by microseismic events usually radiate with in a frequency range between $f = 50 - 400$ Hz. I choose a dominant frequency of $f = 100$ Hz.

A typical value for a thickness of an hydraulic fracture is $h = 0.001 - 0.01$ m. I choose the layer to be $h = 0.001$ m thick. This gives $f \cdot h = 0.1$ m/s in the complex exponent given in equation 2.1.

In Figure 2.2 all four reflection coefficients R_{pp}, R_{ps}, R_{sp} and R_{ss} are illustrated for different $v_{\mathrm{p}}/v_{\mathrm{s}}$ ratios of the solid that translate into the Poisson's ratio σ as

$$\sigma = \frac{(v_{\mathrm{p}}/v_{\mathrm{s}})^2 - 2}{2(v_{\mathrm{p}}/v_{\mathrm{s}})^2 - 2}.$$

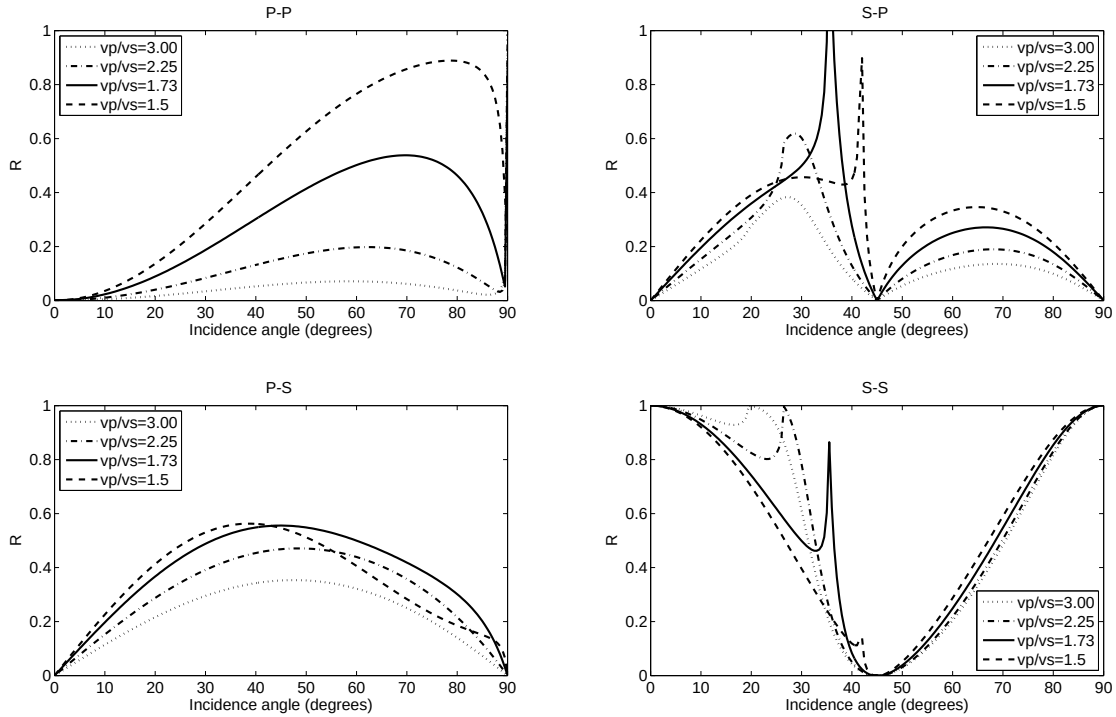

Figure 2.2: *All four reflection coefficients at a thin fluid layer R_{pp}, R_{ps}, R_{sp} and R_{ss}. The parameters are in the range of microseismic needs: $v_{\mathrm{p}} = 4500$ m/s, $\rho_{\mathrm{s}} = 3000$ kg/m^3, $v_{\mathrm{s}} = 1500 - 3000$ m/s, $\rho_{\mathrm{f}} = 1000$ kg/m^3, $f = 100$ Hz, and $h = 0.001$ m, thus $f \cdot h = 0.1$ m/s. In each plot the S wave velocity is varied in order to represent different Poisson's ratios.*

For changes of $f \cdot h$ within one order of magnitude the reflection coefficients do not change significantly. However, as one can see, changes of Poisson's ratio have a great impact on the magnitude of the reflection coefficient for incidence angles of $\theta \geq 5°$. For the S-S reflection, there is a maximum caused by the total internal reflection within the fluid layer. The reflection coefficient increases with the ratio $v_{\mathrm{p}}/v_{\mathrm{s}}$.

An interesting feature of the reflection from the incident S wave is that both reflected waves show a minimum at about $\theta = 45°$. For the reflected S-S wave and for large exponents there actually exist two minima around $\theta = 45°$. However, for microseismic frequency and layer thickness ranges, which means small exponents $f \cdot h$, the distance between both minima decreases until the two minima coincide at $\theta = 45°$. In the case of an S wave with $\theta = 45°$ incidence angle, the quantity $\left(\frac{1}{v_{\mathrm{s}}^2} - 2\zeta_{\mathrm{s}}^2\right)$, which is part of the Rayleigh function R, vanishes as $\zeta_{\mathrm{s}}(45°) = \frac{1}{v_{\mathrm{s}}} \cdot \frac{1}{\sqrt{2}}$. This feature is independent of the respective velocities.

2.3 Approximation at Slip Contact

For microseismic needs it is helpful to use an approximation of the reflection coefficients. Typical quantities are $h = 0.001 - 0.1$ m thick fractures and waves in the frequency range of $f = 50 - 400$ Hz (e.g. Reshetnikov et al. (2010b); Rentsch (2007)). If the value of an exponent is sufficiently small, the exponential function can be approximated using its power series. Taking this into account, the reflection coefficients are represented by the following approximations:

$$R_{\mathrm{pp}} = 1 - \frac{(\beta_{\mathrm{s}}^2 - \zeta_{\mathrm{p}}^2)^2}{R}, \tag{2.9}$$

$$R_{\mathrm{ps}} = \frac{2v_{\mathrm{p}}\beta_{\mathrm{p}}\zeta_{\mathrm{p}}(\beta_{\mathrm{s}}^2 - \zeta_{\mathrm{p}}^2)}{v_{\mathrm{s}}R}, \tag{2.10}$$

$$R_{\mathrm{sp}} = -\frac{2v_{\mathrm{s}}\beta_{\mathrm{s}}\zeta_{\mathrm{s}}(\beta_{\mathrm{s}}^2 - \zeta_{\mathrm{s}}^2)}{v_{\mathrm{p}}R}, \tag{2.11}$$

$$R_{\mathrm{ss}} = \frac{4\beta_{\mathrm{s}}\beta_{\mathrm{p}}\zeta_{\mathrm{s}}^2}{R} - 1. \tag{2.12}$$

The obtained approximations present the zero thickness limit and correspond to the exact reflection coefficients at a slip interface between two elastic half-spaces (Pod'yapolsky, 1963; Schoenberg, 1980). In Figure 2.3 I compare the approximated reflection coefficients with the exact formulas for the case $f \cdot h = 4$ m/s , the upper limit of the approximation. There are visible differences only for P-P and S-S reflection coefficients.

It can be seen, that the smaller the value of $f \cdot h$, the smaller is the relative error. This is equivalent to the condition that I used to obtain the approximations. Further, I see the very small values of relative error for incidence angles $0 - 20^\circ$ in the case of P-S, S-P, and S-S approximations.

2.3.1 Comparison to Linear Slip Model

The Linear Slip Model (LSM), introduced by Schoenberg (1980), is commonly used in ultrasonic non-destructive material property evaluation (Nagy, 1992) as well as in seismology over fractured rocks (Grechka et al., 2000). Experimental verification of the LSM applicability have been carried out in laboratory tests (Pyrak-Nolte et al., 1990) and in numerical studies (Lombard and Piraux, 2006). I adapt the LSM to microseismic scale and confirm the slip contact approximation. Other than in the previous section, where I have derived expressions for reflection coefficients at slip contact by an approximation of the exact solution, here, boundary conditions are approximated. Taking into account the specifics of the studied process as well, a useful seismic model is found.

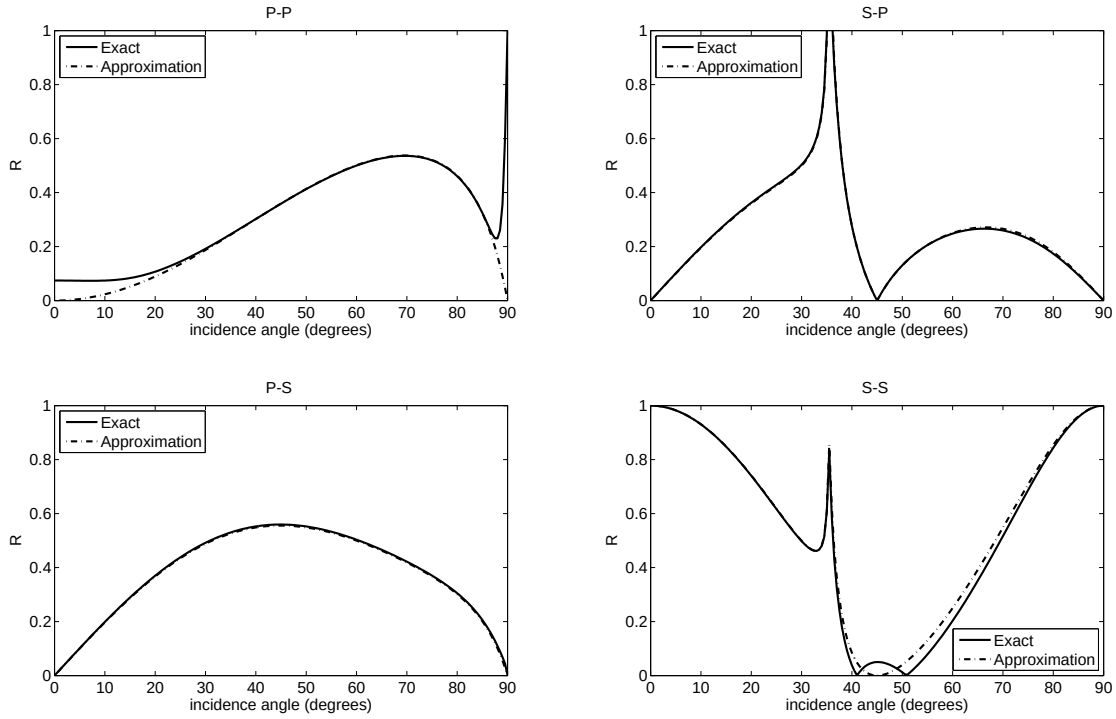

Figure 2.3: *Comparison of approximated (dashed line) reflection coefficients with the respective exact formulas (solid line). The parameters are* $v_\mathrm{p} = 4500$ *m/s,* $v_\mathrm{s} = 2598$ *m/s (Poisson's ratio is 0.25),* $\rho_\mathrm{s} = 3000$ *kg/m*^{3}*,* $v_\mathrm{f} = 1500$ *m/s,* $\rho_\mathrm{f} = 1000$ *kg/m*^{3}*,* $f \cdot h = 4$ *m/s.*

The key idea of the LSM is a linear slip condition between two elastic media at an imperfectly bonded interface. While the stress vector $(\boldsymbol{\sigma} \cdot \vec{n})$ is continuous across the boundary, the displacement $\vec{u}$, which is linearly related to the stress, is not required to be continuous. Assuming a rotational invariant and linearly elastic isotropic interlayer (physical values connected to the interlayer are denoted by superscript il, h describing its width), the following boundary conditions are valid:

$$[\boldsymbol{\sigma} \cdot \vec{n}] = 0, \tag{2.13}$$

$$[\vec{u}] = \begin{pmatrix} \eta_\mathrm{T} & 0 & 0 \\ 0 & \eta_\mathrm{T} & 0 \\ 0 & 0 & \eta_\mathrm{N} \end{pmatrix} \cdot \boldsymbol{\sigma} \cdot \vec{n} \tag{2.14}$$

containing the real and frequency independent tangential and normal compliances η_T and η_N, respectively. $[\vec{u}]$ denotes the jump of $\vec{u}$ across the linear slip interface. These boundary conditions are derived on the assumption of a quasistatic loading of the perfectly bonded interlayer and its great compliance. The loading of the layer can be considered as quasistatic if the wavelength within the interlayer is large compared to the layer's width, $\lambda_\mathrm{p}^{il} \gg h$.

This hypothesis gives rise to a linear slip behavior in the simple case of a normal incident P wave. In this case the only non-zero components of the displacement and stress are u_z and σ_{zz}:

$$u_z^0 = exp[i\omega(t - z/v_{\mathrm{p}})] \tag{2.15}$$

and

$$\sigma_{zz}^{il} = \left(\rho^{il} v_p^{il\,2}\right) \frac{\partial u_z}{\partial z}. \tag{2.16}$$

Any particular component of the displacement and stress vector at the bottom of the layer ($z = h$) can be expressed by their series expansions for thin fractures. For example, the displacement becomes:

$$u_z^{il}(h) = u_z^{il}(0) + h \cdot \left.\frac{\partial u_z^{il}}{\partial z}\right|_{z=0} + O\left[\left(\frac{h}{\lambda_{\mathrm{p}}^{il}}\right)^2\right]. \tag{2.17}$$

A similar expression can be found for σ_{zz}.
The quasistatic assumption allows us to neglect second order terms, thus I obtain:

$$[u_z] = h \left.\frac{\partial u_z}{\partial z}\right|_{z=0} \tag{2.18}$$

and

$$[\sigma_{zz}] = \left.\frac{\partial \sigma_{zz}}{\partial z}\right|_{z=0}. \tag{2.19}$$

Taking into account the harmonic form of the incident wave, and equations 2.16, 2.18, and 2.19, the relative changes of traction $[\sigma_{zz}]/\sigma_{zz}^0(0)$ and displacement $[u_z]/u_z^0(0)$ during the passage of the wave through the layer can be obtained. It can be shown that $Z^{il}/Z_{\mathrm{p}} = v_{\mathrm{p}}\rho_{\mathrm{s}}$, where Z^{il} denotes the acoustic impedance of the interlayer and Z_p denotes the acoustic impedance of the medium (L. M. Brekhovskikh and O. A. Godin, 1990). If the acoustic contrast is high, the traction can be considered continuous across the interlayer, which explains the boundary condition 2.13. The combination of equations 2.16, 2.18, and 2.14, gives the specific compliances:

$$\eta_{\mathrm{N}} = \frac{h}{\rho^{\mathrm{il}} v_{\mathrm{p}}^{\mathrm{il}\,2}}; \qquad \eta_{\mathrm{T}} = \frac{h}{\rho^{\mathrm{il}} v_{\mathrm{s}}^{\mathrm{il}\,2}} \tag{2.20}$$

with the dimension length/stress. For viscous or viscoelatic material the specific compliances become complex and frequency dependent (Tleukenov, 1991).

Applying the LSM to the model of a thin fracture filled with an ideal fluid I can calculate the reflection coefficient. Since the shear modulus of a perfect fluid is zero, $\eta_{\mathrm{T}} \to \infty$. If I compare the bulk modulus $\rho_{\mathrm{f}} v_{\mathrm{f}}^2$ with a feasible fracture width, in a zero-order approximation $\eta_{\mathrm{N}} \to 0$ and the reflection coefficient at a slip boundary R_{SB} can be approximated. This approach gives the same result

as the previously presented approximation at slip contact (equ. 2.9-2.12).

An accurate result at thin fractures can be obtained when I let the normal compliance be the small and exact parameter $\eta_{\mathrm{N}} = \frac{h}{\rho_{\mathrm{f}} v_{\mathrm{f}}^2}$. Considering a monochromatic wave interaction with the LSM boundary, the reflection coefficient for zero degree incidence angle near the linear slip interface $R_{\mathrm{LSM}}(0^\circ)$ (Schoenberg, 1980) is:

$$R_{\mathrm{LSM}}(0^\circ) = \frac{\mathrm{i}\omega\eta_{\mathrm{N}} Z_{\mathrm{p}}}{2 - \mathrm{i}\omega\eta_{\mathrm{N}} Z_{\mathrm{p}}}. \tag{2.21}$$

As one can see η_{N} occurs in a combination $\omega\eta_{\mathrm{N}} Z_{\mathrm{p}}$, which is the proper parameter in an asymptotic expansion. Because this is a dimensionless parameter, it is more convenient to use this combination.

In the case of an incident shear wave, η_{N} has to be replaced by η_{T}. As mentioned above, $\eta_{\mathrm{T}} \to \infty$ for a perfect fluid, and thus $R_{\mathrm{SS}}^{\mathrm{LSM}} \to -1$, which is the same result as the exact solution or approximation at slip contact gives. Angle dependent more accurate solutions for the reflection coefficients at a fluid interlayer coincide with the exact solutions with an accuracy of $\sim 1\%$.

3. Comparison to Synthetic Data Using Finite Difference Modeling

In this chapter I will deploy an algorithm based the rotated staggered grid (RSG) to calculate synthetic wavefields and extract reflection coefficients from the modeled wavefield. In this section I will briefly specify the advantages of the algorithm, since I will use the forward modeling also in later sections of my thesis.

The analytical solution of the elastic wave equation can describe only rather simple models. Ray tracing methods can also be applied in order to describe the wave propagation within these models. However, as soon as the setup gets more complex, the computing time for the ray tracing drastically increases whereas it remains the same for Finite Difference (FD) methods. FD methods provide a numerical solution of differential equations. In geophysical forward modeling problems, this differential equation is most likely the displacement equation for wave propagation:

$$\rho(\mathbf{r})\ddot{u}_i(\mathbf{r}) = (c_{ijkl}(\mathbf{r})u_{k,l}(\mathbf{r}))_{,j} + f_i(\mathbf{r}),$$

whereas c_{ijkl} is the elasticity tensor, u_i is the wavefield, and f are the forces applied (e.g. Aki and Richards (2002)). In the FD forward modeling process, the time is discretized. The wavefield $u(t + \Delta t)$ is calculated from the wavefield $u(t)$ and the wavefield at the time step before, $u(t - \Delta t)$:

$$u_i(t + \Delta t) = 2u_i(t) - u_i(t - \Delta t) + \Delta t^2 \ddot{u}_i(t).$$

Here, a Taylor polynomial for the time update is deployed and the derivatives have to be approximated using numerical operators.

The stiffness tensor c_{ijkl}, the density ρ, and the wavefield u are discretized on a grid. In the standard staggered grid approaches, strong fluctuations of elastic properties, such as cracks or pores, cause inaccurate results or instability problems. Spatial derivatives and thus some modeling parameters are calculated on inter-grid positions and therefore have to be averaged. Saenger et al. (2000) proposed the RSG approach to model the elastic wave propagation in arbitrary heterogeneous, and also anisotropic media. In the RSG approach, all medium parameters are defined at their appropriate position

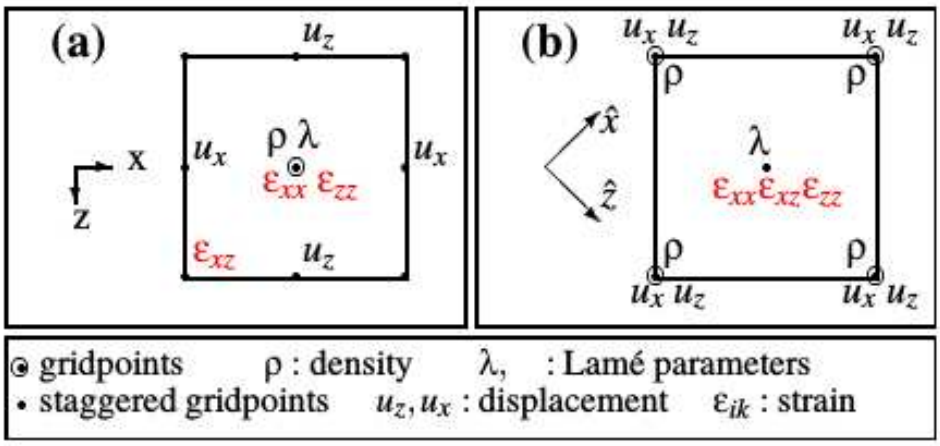

Figure 1.1: Elementary cells with locations where strains, displacement and elastic parameters are defined. **(a)** Locations are shown on a standard staggered grid if no averaging of medium parameters is performed. **(b)** Elementary cell of the rotated staggered grid. Spatial derivatives are performed along the $\hat{x}$- and $\hat{z}$-axes.

Figure 3.1: *Principle of the RSG in comparison to the standard staggered grid from Saenger (2000).*

within a cell, see Figure 3.1. The computation time in comparison to the standard staggered grid remains the same.

Saenger et al. (2000) have performed a Von-Neuman-stability analysis to show the stability of their introduced RSG algorithm. Dispersion errors (frequency-dependent velocity errors) can not be excluded completely but were reduced to an acceptable degree. The authors have applied the RSG FD modeling to two numerical examples: a 2D crack model to show the capability to model high contrasts, and a 3D aluminium plate model to demonstrate the high contrast case in three dimensions.

The RSG algorithm is capable of modeling arbitrary high contrasts in all kinds of anisotropic media accurate and fast for complex modeling configurations. It therefore is an appropriate method for my concerns: Single fluid filled fractures in elastic, isotropic, and anisotropic rock environment are such arbitrary high contrast inhomogeneities which can be modeled using the RSG method.

3.1 Zero Incidence

Even though the accuracy of the Rotated Staggered Grid Finite Difference algorithm, introduced by Saenger et al. (2000), for thin fractures has been shown before (Krüger et al., 2005), I model 1-D reflections at a thin fluid layer

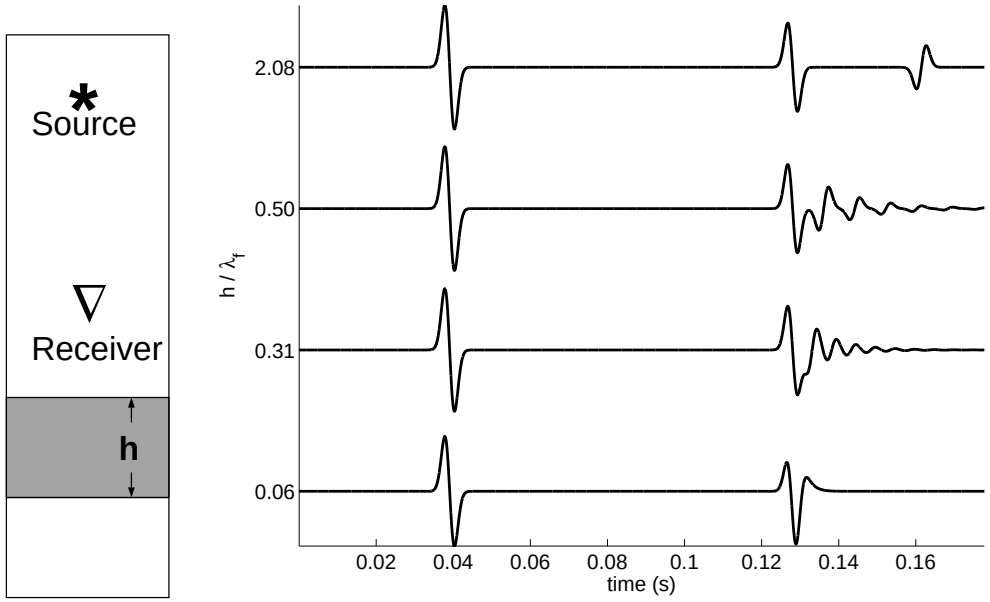

(a) Model setup to derive 1-D reflection coefficients.

(b) Seismograms for different layer thicknesses recorded above the fluid layer. After 0.03 s arrives the direct wave, at 0.12 s follows the reflected wave.

Figure 3.2: *Modeling of the zero incidence reflection coefficient.*

(incidence angle of $\theta = 0°$) in order to show its applicability.

The reflection coefficient in the case of $0°$ incidence angle simplifies to:

$$R_{\mathrm{pp}} = \frac{r(e^{2i\frac{\omega h}{v_{\mathrm{f}}}} - 1)}{1 - r^2 e^{2i\frac{\omega h}{v_{\mathrm{f}}}}}. \tag{3.1}$$

3.1.1 Model Setup

I assume typical quantities that are used in microseismic context. For this particular model (Figure 3.2(a)) I use a dominant frequency of $f = 125$ Hz. The grid spacing is $dh = 0.05$ m.

I generate a plane P wave hitting the fluid layer with $\theta = 0°$ incidence angle. The infinite x-dimension can be realized using only a few grid points since periodic boundary conditions are applied while z-dimension contains 10.000 grid points. The wave propagates a few wavelengths through the medium before it hits the layer.

The plane wave starts propagating below the upper border of the model and is registered at six evenly distributed geophones along z-direction (in Figure 3.2(a) exemplary only one receiver is plotted) and at $\theta = 0°$ incidence angle.

The fluid layer starts at a fixed depth, the lower boundary of the model is varied in different models in order to simulate different layer thicknesses.

The wavelength in the solid is $\lambda_{\mathrm{s}} = 37$ m while it is $\lambda_{\mathrm{f}} = 12$ m in the fluid layer.

The model is calculated using a time increment of $dt = 8.9 \cdot 10^{-6}$s.

3.1.2 Seismograms

The resulting seismograms for 4 different layer thicknesses are plotted in Figure 3.2(b). Since there is no spherical divergence, all 6 receivers above the fluid layer register the same signal. However, the signal is plotted for only one receiver for each case, since the signal at different receivers only differs in time delay. As I expect for a layer that is significantly thicker than the wavelength within the fluid, the reflections from the upper and lower interface are clearly separated. This is illustrated in Figure 3.2(b) for a layer thickness of $h = 25$ m, while the wavelength within the fluid is $\lambda_{\mathrm{f}} = 12$ m, which gives $h/\lambda = 2.08$. Hence, I expect the reflection coefficient to be equal to the reflection at a single solid - fluid interface.

If the layer thickness is within the same order of magnitude as λ_{f}, the signals overlap (second and third seismogram of Figure 3.2(b)). Multiple reflections cause an oscillating of the signal that makes it difficult to determine the complete reflected signal.

If the thickness of the layer is considerably smaller than λ_{f} ($h/\lambda = 0.06$), as sketched in Figure 3.2(b) at the fourth seismogram, the reflected signals from both interfaces appear to be caused by a single interface because the reflections from upper and lower interface are indistinguishable. This means, that the derived formulas 2.3 – 2.6, which in principle are valid for all frequencies but constrained by me to the range of microseismic context, are valid for $\lambda_{\mathrm{f}} \gg h$.

3.1.3 Results

The evaluation of the signals is carried out in Fourier space. The resulting reflection coefficients for $\theta = 0^{\circ}$ incidence angle are plotted in Figure 3.3. As expected for layer thicknesses larger than λ_{f}, the reflection coefficient is equal to a reflection at a single solid-fluid interface.

Reflection coefficients for thin layers are determined quite well. However, for $\lambda_{\mathrm{f}}/2 < h < \lambda_{\mathrm{f}}$ the picking of the reflected signal is difficult, due to the oscillation that is mentioned before. In this case the synthetic reflection coefficients are

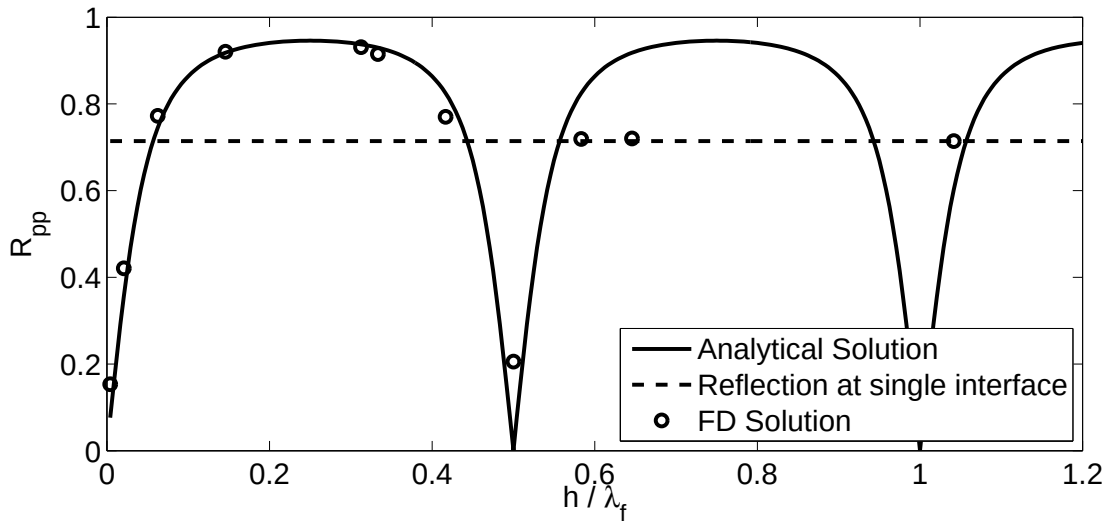

Figure 3.3: *Reflection coefficient as a function of layer thickness.*

not in a good agreement with the analytical solution.

An evaluation of the respective frequency spectra yields an interesting result. For layers much thicker than the wavelength, only the amplitude of the signal decreases, while for layers much smaller than the wavelength, the frequency maximum of the reflected signal shifts to higher frequencies. For wavelengths in the same range as the layer thickness, some frequencies cancel out (Figure 3.4).

3.2 Angle Dependent Reflections

In reality, the rather complex sources and their radiation pattern has to be taken into account. Thus, in this section, I replace the plane wave by a cylindrical wave and investigate the applicability of the analytical approach in comparison to other type than plane wave and other than zero degrees incidence angle.

The setup is sketched in Figure 3.5. A fluid layer is embedded between equal half spaces. An explosion source is deployed 65 m above the interface and receivers are distributed along the x-direction in order to resolve angular dependency. The properties of the solid and the fluid layer are defined in Table 3.1.

The main idea is that I assume the source, reflector and receiver to be at a sufficient distance to each other, such that the wave can be treated as a plane wave.

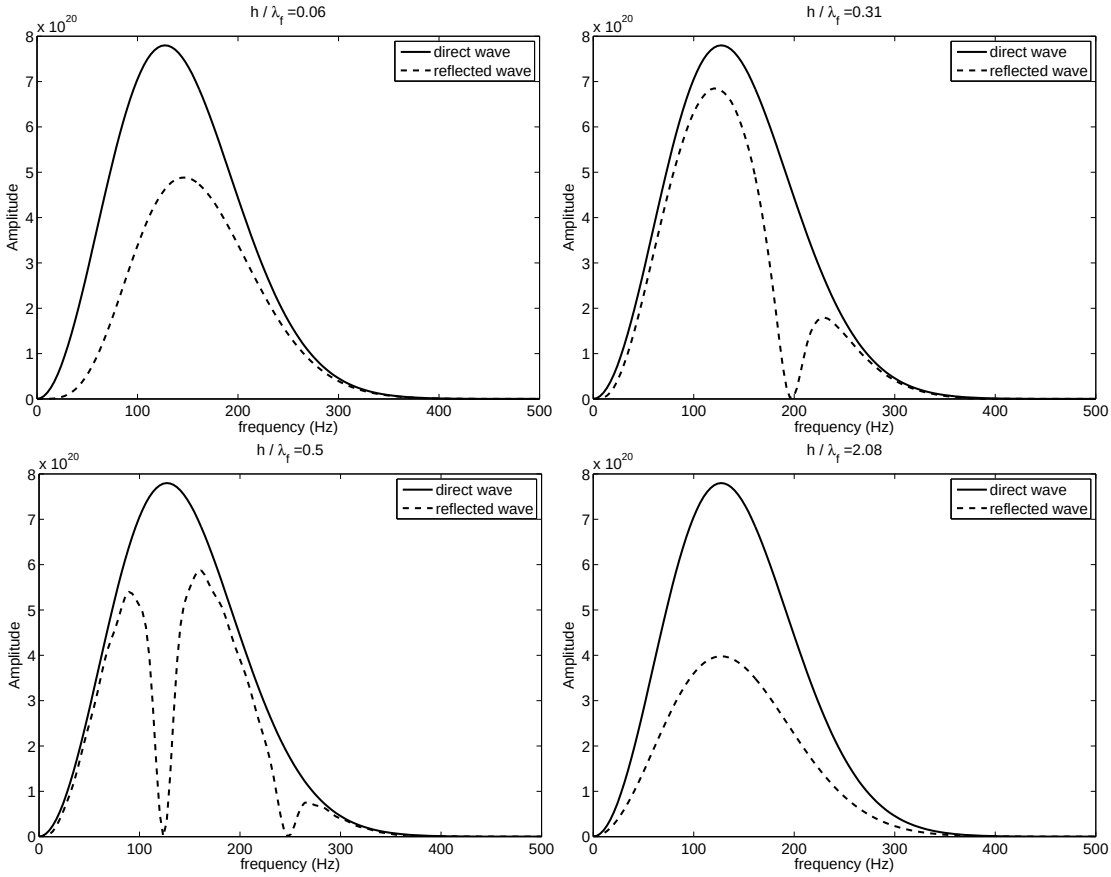

Figure 3.4: *Frequency spectra for different h/λ_{f} combinations are plotted. For $h/\lambda_{\mathrm{f}} \ll 1$ the maximum of the reflected signal is shifted to higher frequencies while for $h/\lambda_{\mathrm{f}} > 1$ it remains at the same frequency. For $h/\lambda_{\mathrm{f}} \sim 1$ some frequencies within the reflected signal cancel out.*

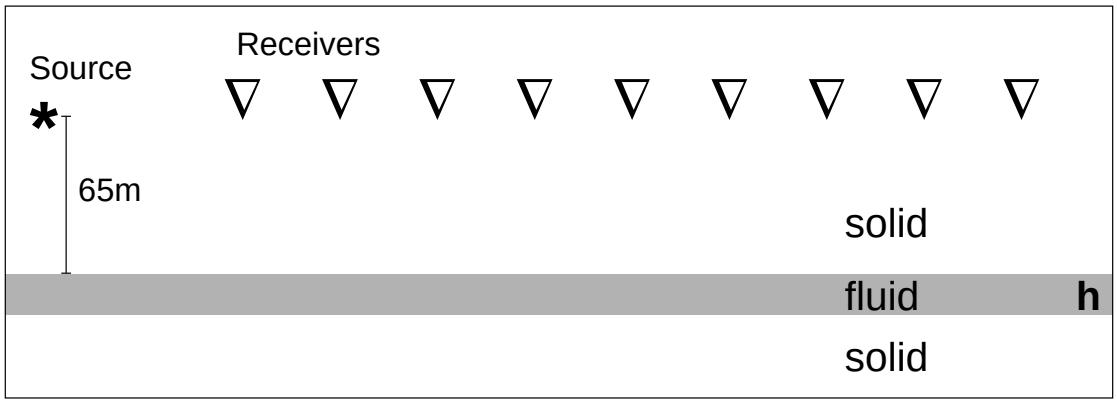

Figure 3.5: *Model to obtain angle dependent reflection coefficients using an explosion source.*

Source type	Point source
Rock P wave velocity	4500 m/s
Rock S wave velocity	2000 m/s
Fluid P wave velocity	1500 m/s
Dominant frequency	171 Hz
Distance source - reflector	65 m
Fracture width	0.5 m
Grid spacing	0.05 m

Table 3.1: *Properties of the solid and fluid media used to calculate angle dependent reflection coefficients.*

3.2.1 Results

Figure 3.6 shows the seismogram recorded at the horizontally evenly distributed receivers. Velocities are chosen in a way, that the direct wave, the P wave, and the S wave, are clearly distinguishable. Reflection coefficients are evaluated in Fourier space and compared to the analytical solution. A layer consisting of 10 grid points proves to be sufficient to model a thin fluid layer with its properties. The reflection coefficient for a 0.5 m thin layer is shown in Figure 3.7. It shows a reasonable agreement compared to the analytical solution.

Figure 3.8 compares the calculated to the analytical solution for a fixed angle of incidence. While the angle of incidence is constant ($\theta = 31.6°$), the fracture width h is varied. As for normal incidence and a plane wave, the comparison of synthetic data and analytical solution yields to the following observation. I see a good agreement for $h/\lambda_f < 0.5$.

This confirms the occurrence of high reflection coefficients at thin fluid layers and thus supports the idea to use microseismic waveform data to estimate reflection coefficients and interpret them in terms of reservoir properties.

3.3 Plane Wave Approximation

The analytical solutions for the reflection coefficients at a thin fluid layer are derived based on the assumption of an incident plane wave. In the modeling, however, an explosion point source is deployed in order to model a more realistic source. We assume that the reflecting layer and the receivers are far away from the source point so that they are effectively hit by a plane wave. We consider this fact by including the spherical divergence correction into the calculations. A good agreement of the results confirms this approach.

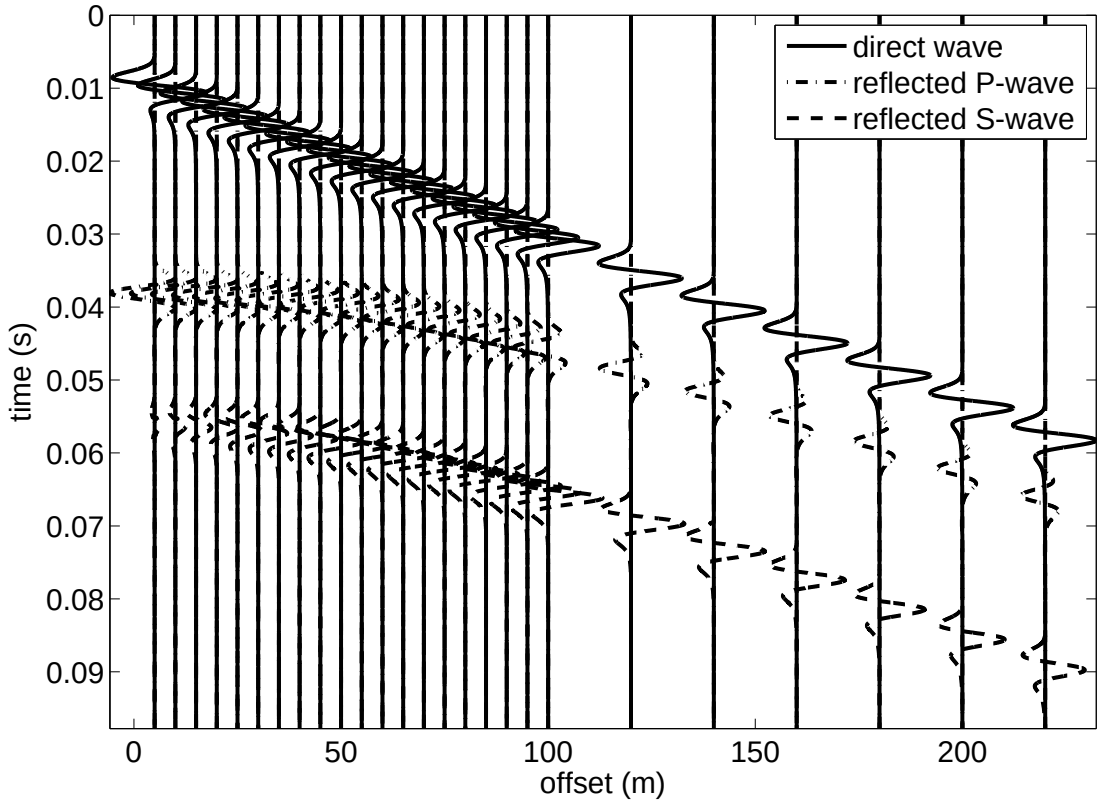

Figure 3.6: *Modeled direct and at fluid layer reflected wave, recorded at receivers on a horizontal line with the source.*

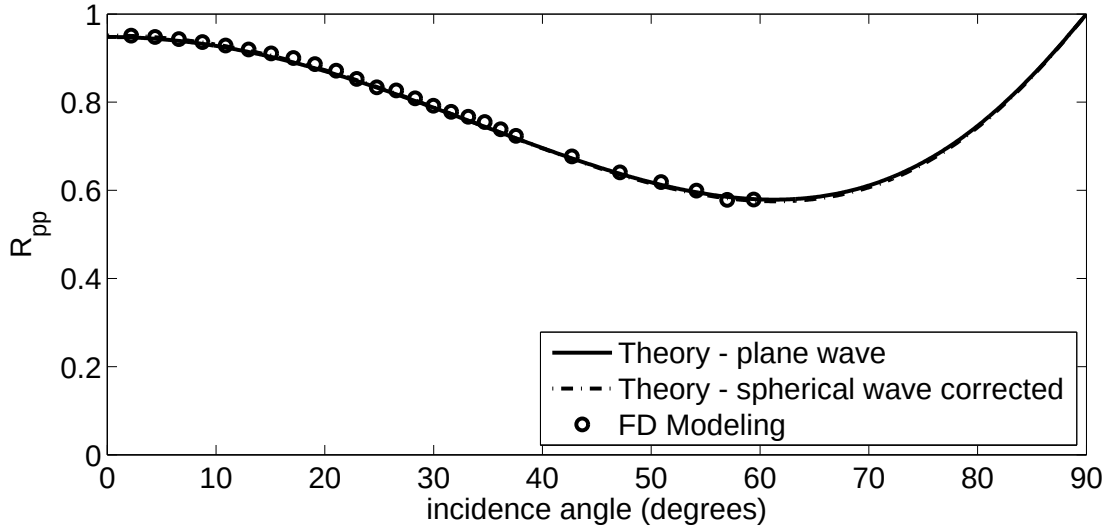

Figure 3.7: *Comparison of exact solution for the P-P reflection coefficient and modeled reflection coefficient using FD method.*

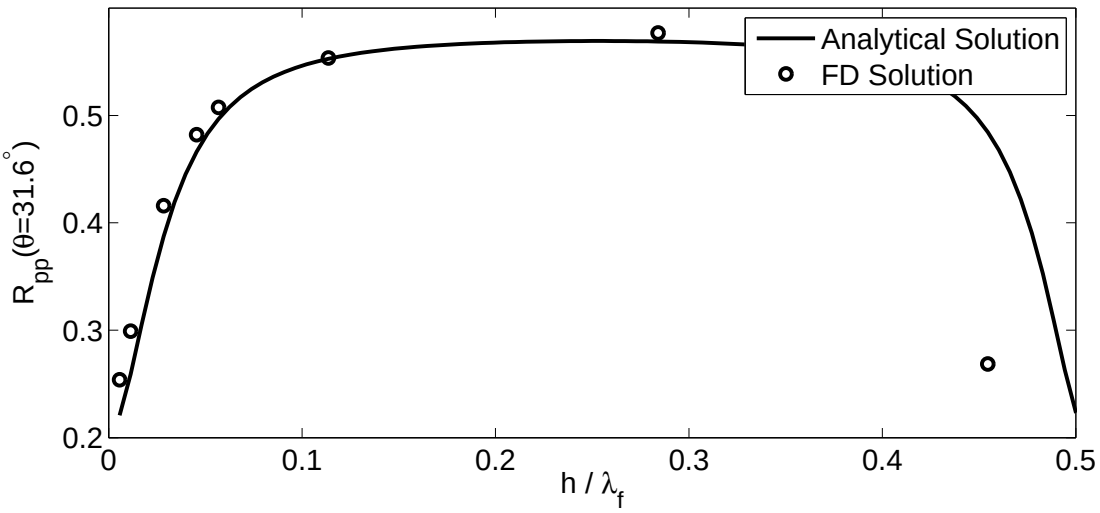

Figure 3.8: *Reflection coefficient $R_{\mathrm{pp}}(\theta = 31.6°)$ as a function of layer thickness.*

3.4 Summary: Reflection Coefficients from Thin Fluid Layers

In this chapter I show that reflections which are present in microseismic data may be caused by reflections at hydraulic fractures.

I investigate reflection coefficients at an idealized hydraulic fracture. The fracture is modeled by a thin fluid layer which is embedded between identical solids. Exact analytical solutions for all four possible reflections (P-P, P-S, S-P, S-S) are presented and analyzed. The solutions are angle dependent and parameters are the densities and velocities of the fluid and the solid. I find out that for values used in microseismicity the reflection coefficients change insignificantly with the product $h \cdot f$ but the coefficients are strongly dependent on the Poisson's ratio.

An important conclusion that I draw from the analysis of the formulas is that even for infinite small fractures, high reflection coefficients occur and thus it is justified to use reflection seismic waveform data from microseismic events in order to image small scale subsurface structures.

Furthermore I approximate the derived formulas for a vanishing layer thickness, which corresponds to the solution at slip contact. These approximations are compared to the Linear Slip model and a comparison of both models shows that they give the same results even though they are derived based on different assumptions and constraints.

An applicability test proposed further FD modeling in order to calculate

synthetic wave data and estimate reflection coefficients. The modeling of angular dependency of P-P reflections confirms the analytical solution, considering minor deviations caused by the sphericity of the incident wave.

The successful modeling of P-P reflections proposes to continue the evaluation of P-S reflections and the modeling of reflections by an incident S wave. In future investigations the solutions can be modified considering a viscous fluid or even a fracture with several contacts. In the following chapters, analytical and modeling results will be compared to real microseismic waveform data. These results will help to interpret reflection coefficients in terms of reservoir and fracture properties.

4. Isotropic Case: Application to Induced Seismicity at the Basel EGS

The data used in the following chapter were acquired in an elastically isotropic environment before, during, and after a stimulation experiment as part of the Deep Heat Mining (DHM) Project in Basel, Switzerland.

In times of the energy transition the exploitation of geothermal energy becomes more and more important. Germany is one of the big shots in the sustainable energy transition. The German government declared that the sustainable energy shift is a way into a secure, environment-friendly, and an economically successful future of energy supply (BMWi, 2015). After the huge public discussion in 2011 following the 2011 Tohoku earthquake, the German government re-assessed their Energy Concept to shorter lifespans of nuclear power plants. As a consequence, a quicker implementation of reorientation in energy supply (known as "Energiewende") is demanded. This is based on halving the energy consumption and, at the same time, the expansion of renewable energies (BMWi, 2014).

In contrast to fluctuating solar- and wind-energy, deep geothermal reservoirs continuously provide their energy. The potential in geothermal energy lies in the combination of direct heat production and electrical energy production. In Germany the Upper Rhine Graben, the North German Basin, and the Molasse Basin are particularly suited for geothermal exploitation. In 2013, in Germany, 25 geothermal plants provided 222.95 MW heat energy and four geothermal plants provided 12.31 MW electrical power (BMWi, 2014). The basic principle is to circulate water through the hot rock, the target area, and to extract heat from depth. To reach economic flow rates in so called Enhanced Geothermal Systems (EGS), the naturally pre-existing fractures are stimulated and thus re-opened or new fractures are opened. This stimulation can generate microseismic events and thus the process needs to be monitored. However, microseismic waveform data contain plenty of information on the reservoir and can help to characterize the reservoir.

The recordings of the microseismic events provide the possibility to image the

subsurface structures in the vicinity of the borehole. Mapping of pre-existing fractures may be of interest for the development of the reservoir and can give indications on the fracture growth. Dyer et al. (2008) used a diffraction stack-type migration to image potential fractures at the Basel 1 EGS site. They image three reflectors from 600 – 1600 m east of the event cloud, but because of the limited distribution of events, the authors state that it is possible to have imaged noise. Reshetnikov et al. (2015) used the directional approach in combination with a strict selection of events to be imaged. A strong signal to noise ratio and rectilinearity are restrictions that the authors applied prior to imaging. The mapped reflectors are interpreted as fluid filled cracks or at least highly permeable rock zones.

The Basel DHM project in the Swiss part of the Upper Rhine Graben aimed to build a co-generation pilot plant producing both thermal and electrical energy. In the following, I will introduce the data set, and then apply the estimation of reflection coefficient procedure to the data. Finally, I will interpret the reflection coefficient in order to characterize the fractured zones and then compare the results to other models.

4.1 Introduction to the Data Set

In the frame of the DHM project, the Basel 1 well was drilled in 2006. Twenty one days of stimulation were planned. However, the induced events reached magnitudes of M_{L} 2.6 and thus the injection of fluid was stopped after only 6 days. Within 5 h after the shutting, a M_{L} 3.4 seismic event occurred, followed by three aftershocks of $M_{\mathrm{L}} > 3$ during the next 56 days (Häring et al., 2008).

The Basel 1 well was drilled through 2.4 km of sedimentary rocks and 2.6 km of granitic basement. The stimulation to enhance the permeability of the reservoir was performed in the open hole section below 4629 m.

The seismic monitoring system consisted of six permanent stations: Otterbach 1 (OT1), Haltingen (HAL), St. Johann (STJ), Schützenmatte (MAT), and Riehen 2 (RI2) in the sedimentary layer, and Otterbach 2 (OT2) in the granite, see Figure 4.1.

The events were re-located by Kummerow et al. (2011). The authors used P and S arrival time picks for 2834 microseismic events. For events, which were identified as multiplet events due to their waveform similarity, the arrival times could be automatically improved. The location procedure was performed in the above mentioned two-layer velocity model, see Table 4.1. 2138 events could be re-located reliably with an average *rms* misfit of only 3 ms. A map view of the events and the station distribution is plotted in Figure 4.2(a) and in a zoom in Figure 4.2(b).

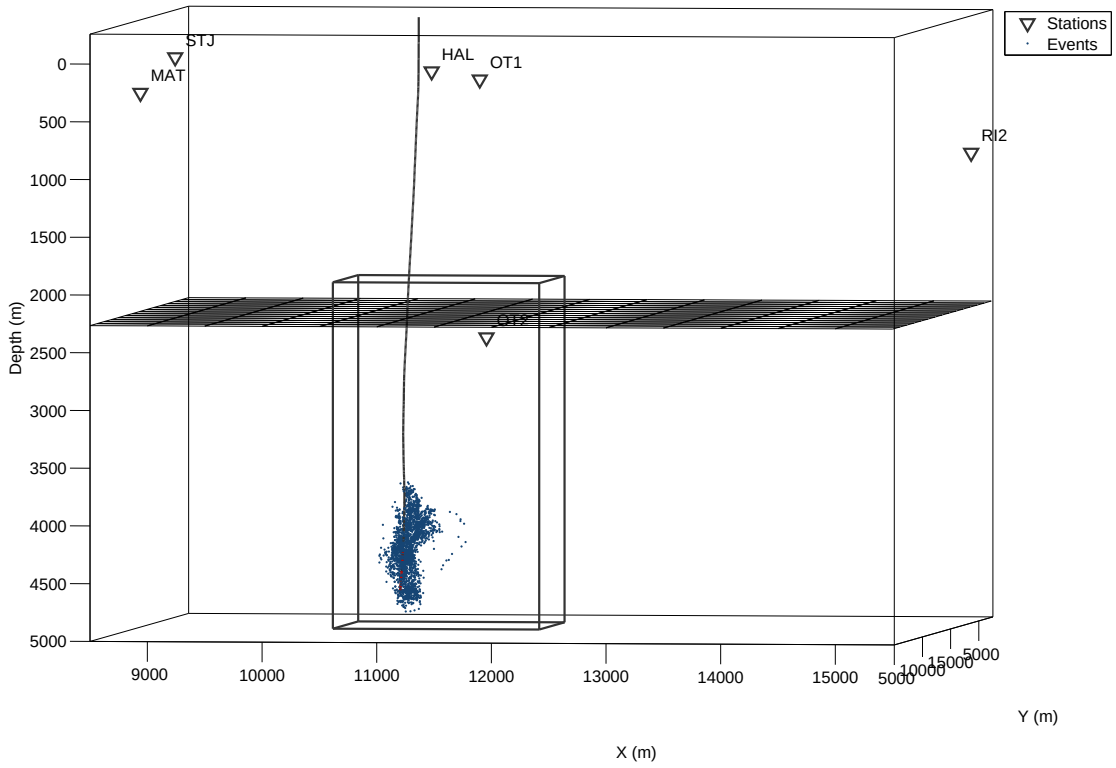

Figure 4.1: *The Basel acquisition geometry. 5 stations in the sedimentary layer, and one station in the granitic basement. The meshed plane depicts the velocity interface between both layers. The borehole Basel 1 is drawn as a black line, with its open hole section in red. The microseismic events are plotted as blue dots. The box displays the later imaging volume.*

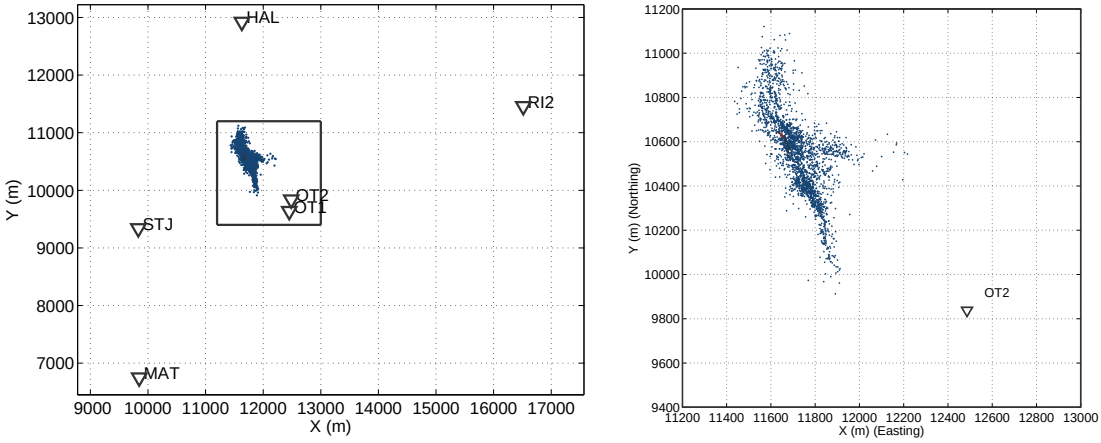

(a) The Basel Station configuration.

(b) The Basel microseismic event distribution.

Figure 4.2: *A map view of the microseismic event cloud and the station distribution. The borehole Basel 1 is drawn as a black line, with its open hole section in red. The microseismic events are plotted as blue dots.*

Interface depth	Sedimentary layer	Granitic layer
2265 m	v_p = 3980 m/s v_s = 2080 m/s	v_p = 5940 m/s v_s = 3450 m/s

Table 4.1: *The elastic properties of the two-layer velocity model at Basel.*

Due to the different distances and thus ray paths to the stations, the data quality of the recorded events varies from station to station. In Figure 4.3 the waveforms of one specific event recorded at the different stations are plotted. No pre-processing has been applied to this data. On most of the stations a clear P and S arrival is visible. The highest signal-to-noise-ratio and thus clearest signal is recorded on station OT2, which is to be expected, since the station is the closest one and the wave travels only through granite, which has a lower attenuation than sediments. In contrast, station OT1, which is deployed more or less above OT2, shows a quite high noise level.

In Figure 4.4 a common receiver gather of the z-component of the first 301 recorded events is plotted. The data are P wave aligned, the arrival is marked by light blue arrows. In the common receiver gather clear signatures of reflections are visible (green and dark blue arrows). The reflections arrive at similar times. That means, that they originate from similar structures. Different (trace) sorting algorithms can be applied and highlight different characteristics of the events.

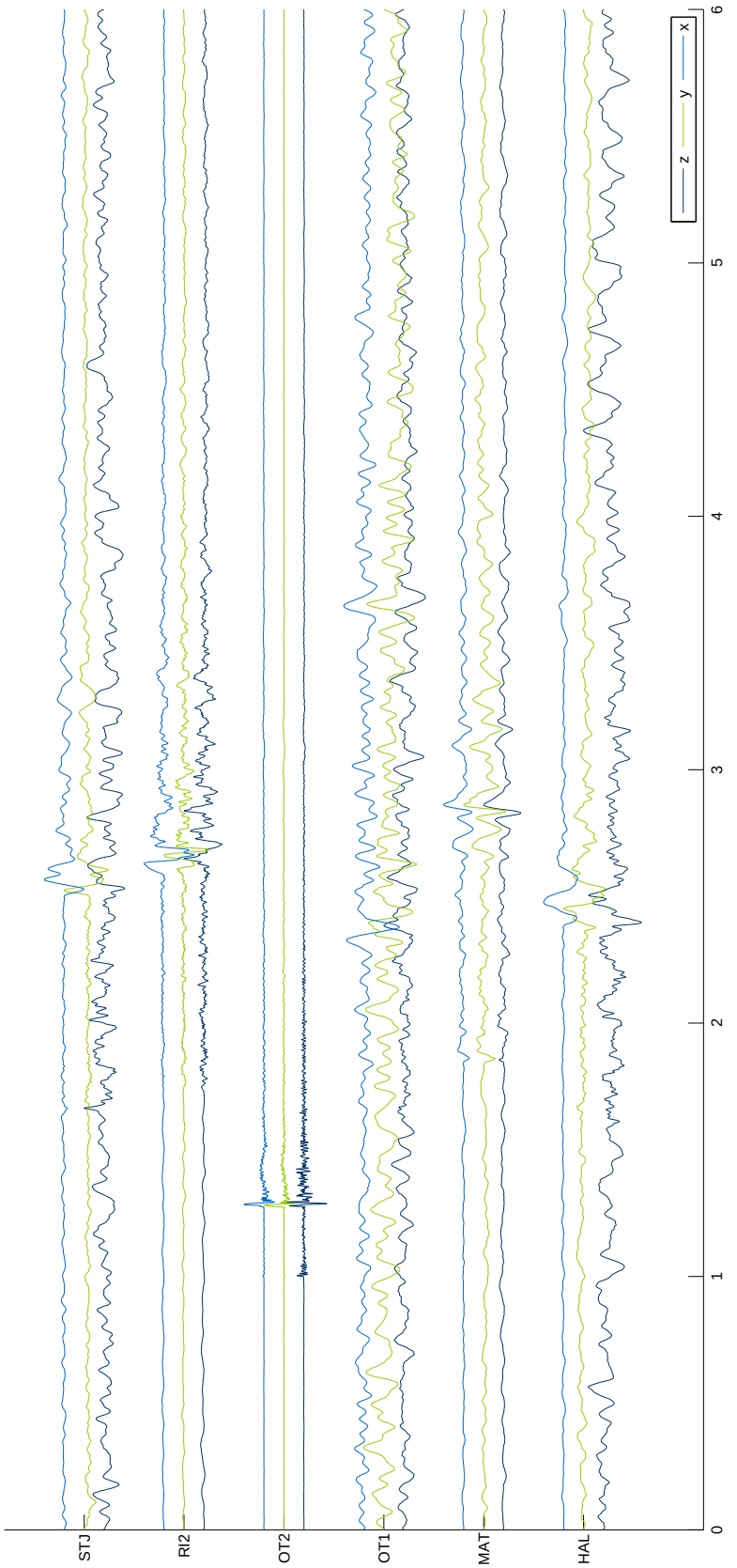

Figure 4.3: *Seismograms of one example event recorded on the different stations. The Data quality varies from station to station.*

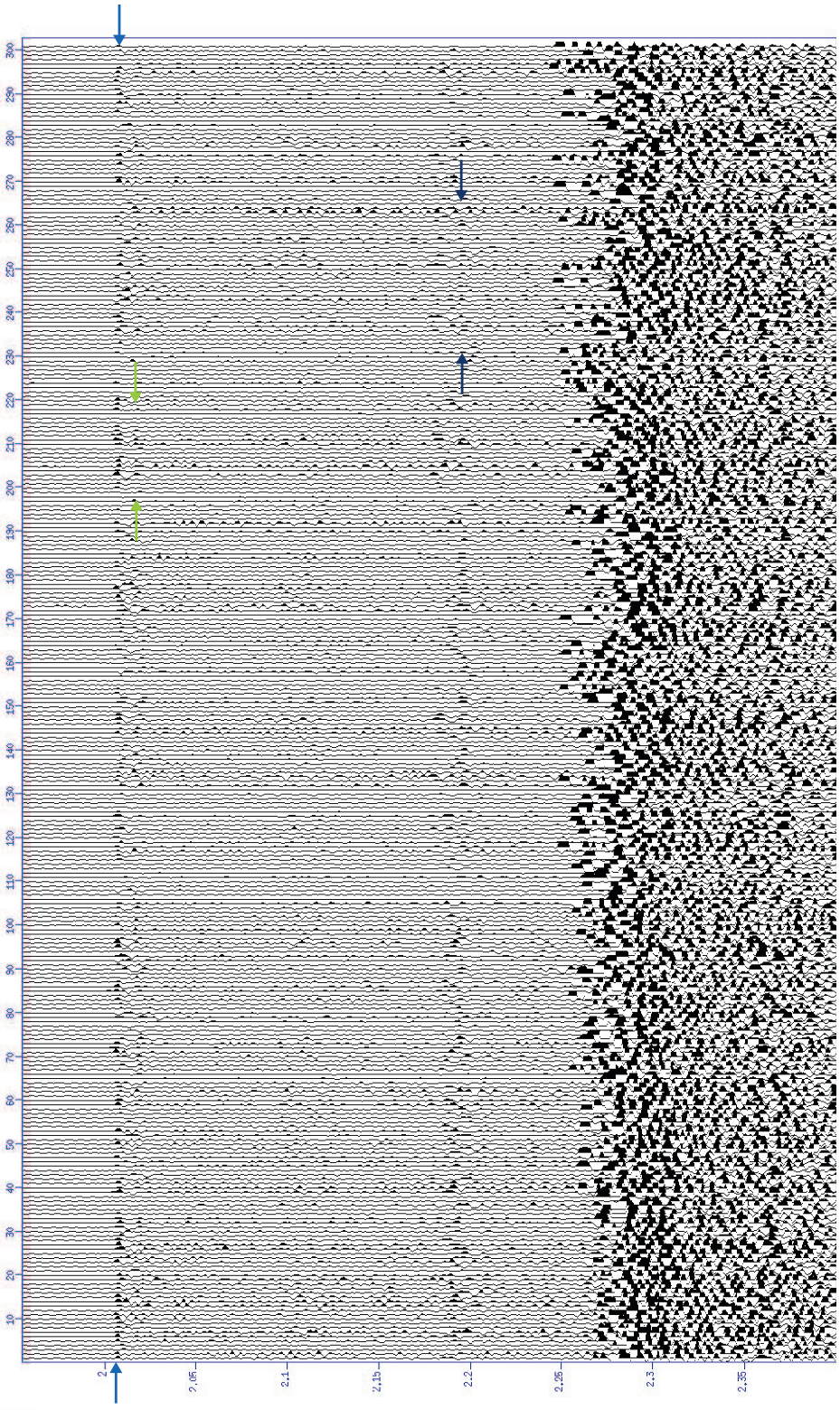

Figure 4.4: *A common receiver gather of the z-component of the first 301 recorded events. The wave trains are P wave aligned. The P wave arrival is marked by a light blue arrow. A reflection possibly from a structure in the vicinity of the borehole is marked by the green arrows. Another reflection is marked by dark blue arrows.*

4.2 Previous Imaging Results

In their study, Reshetnikov et al. (2015) used the recorded events as passive seismic sources. They applied a strict selection of events using the signal-to-noise-ratio and rectilinearity as a measure. After this pre-selection, they applied the Fresnel Zone Migration to image subsurface structures. They could image several small scale structures in the vicinity of the open hole section.

Their imaging result is shown in Figure 4.5. The blue shaded areas are zones of high reflectivity imaged using PP reflection data recorded at station OT2, whereas the zones of high reflectivity imaged using data recorded at station OT1, are shaded red. Plotted are the isosurfaces of the mostly planar reflectors, bending at the edges is due to the limited data aperture. The reflectors partly overlap or complement each other.

An interpretation suggested by the authors is that in order to provide a sufficient contrast, that the zones of high reflectivity are cracks or weak rock zones, which are highly permeable. These zones serve as fluid pathways and exhibit aseismic behavior. However, no information on the quantity of reflectivity is given.

4.3 Identification of Reflected Phases

During their location procedure Kummerow et al. (2011) identified sets of multiplets, so called clusters. Events that exhibit similar waveforms and originate approximately at the same locations, have possibly the same geophysical origin and additionally their focal mechanisms are likely to be similar. The largest clusters, the clusters containing a large number of events, are plotted in Figure 4.6. The cube is the same volume which is also indicated in Figure 4.1. The zones of high reflectivity imaged by Reshetnikov et al. (2015) using the data recorded at station OT2 are plotted as gray planes. The clusters are in the vicinity of the open hole section of the well Basel 1 and do not correlate with zones of high reflectivity. In the following, I will consider only data from clustered events recorded at station OT2.

I now make use of the following: Events with similar waveforms travel similar ray paths and therefore illuminate similar structures. That means, in order to identify reflected phases within the waveforms, it is appropriate to consider specific clusters and batch-process their events.

In Figure 4.7 cluster A is exemplary plotted to show the good data quality and the similarity of the waveforms. The components are trace-normalized and P

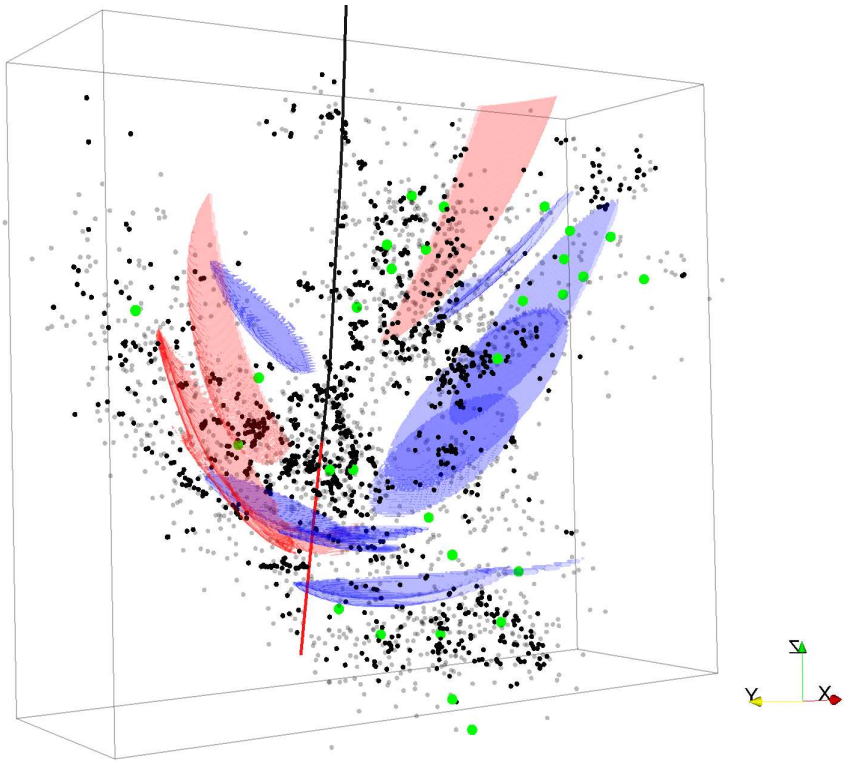

Figure 4.5: *Imaging result of Reshetnikov et al. (2015). Grey dots represent any events, black dots are clustered events, and green dots are events with a relatively high magnitude. The borehole is plotted as a black line with its open hole section in red. Blue isosurfaces are zones of high reflectivity imaged using data recorded at station OT2, red isosurfaces are imaged by data from station OT1.*

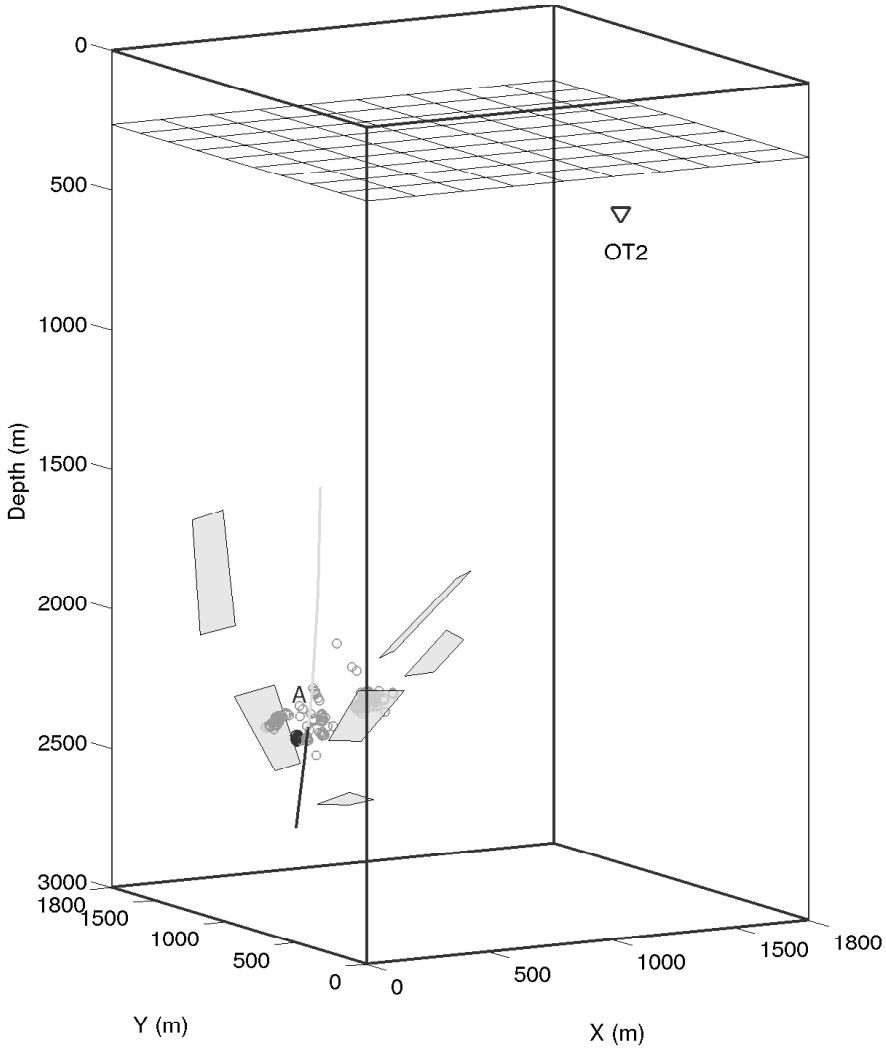

Figure 4.6: *Imaging volume in local coordinates, containing the velocity interface (meshed plane), the largest clusters (gray circles), the borehole Basel 1 (gray line, black: open hole section), previously imaged planar reflectors (gray planes), and the station OT2 (triangle). Cluster A is plotted with black circles.*

wave aligned.

In Figure 4.10 the z-component of the same cluster is plotted. Several coherent signals in the P wave coda are highlighted. They are likely reflected and converted phases from heterogeneities in the vicinity of the borehole. The velocity interface right above the receiver as an origin of reflection has been excluded by polarity analysis, because the registered signals hit the receiver from below.

4.4 Passive Seismic Imaging

As said above, in the following I will focus on the data that were recorded at station OT2. There are two main reasons for that. First, the signal-to-noise-ratio is good and second, this station is closest to the cloud of microseismic events. That means, that the wave travel mainly in a single isotropic velocity layer and that I can select an imaging volume with a sufficiently small grid spacing for a high resolution image.

4.4.1 Focusing Depth Migration

In this work I apply the Fresnel Volume Migration (FVM) (Buske et al., 2009) as an imaging technique. In the following I will image the P wave coda of a single event or event cluster in the Basel geothermal reservoir. In the chapter thereafter my considerations are based on the single event FVM results of Reshetnikov et al. (2010a).

For a single event, or sparse event distribution, standard Kirchhoff Prestack Depth Migration would smear the energy along the two-way-travel time isochrones and an accurate location of a reflector is not possible. Even if several events from a cluster are stacked, the image can not be improved because the events are clustered in space. This means, that the events are close to each other and the sum of the two-way-travel time isochrones would not interfere in such a way, that they could resolve the reflector. In this case, a directional migration approach can restrict the image to the actual reflector.

In the case of a low coverage of receivers, Fresnel Volume Migration can improve the resulting image. In the FVM approach, the migration operator is limited. The emergent angle at the receiver is estimated and the ray is traced back into the subsurface. The back propagated wavefield is restricted to the first Fresnel Volume and the scattered energy is smeared around the actual reflection point.

Figure 4.8 illustrates the principle for significantly different travel time distances from the reflector to the source and the receiver. Because of the travel time

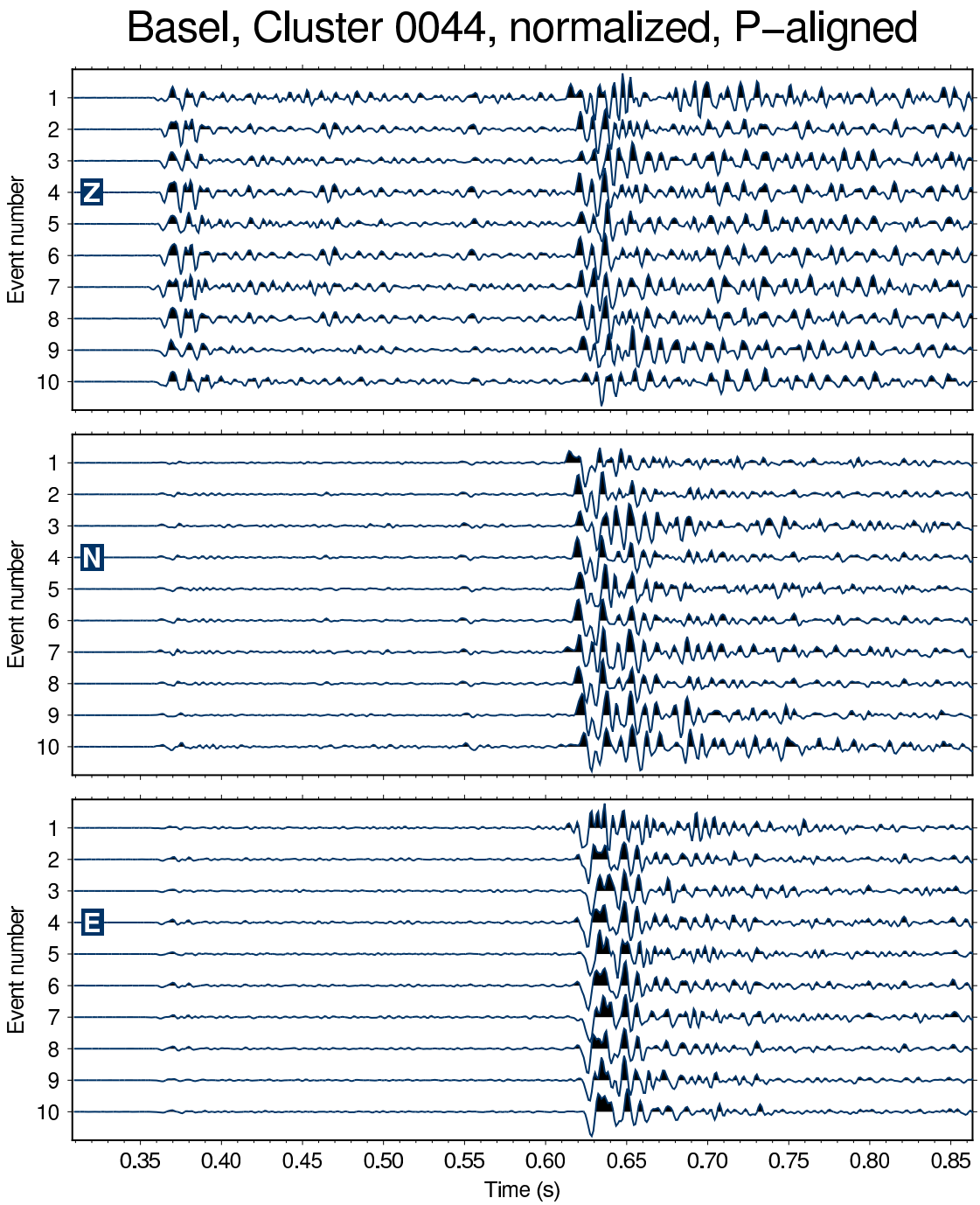

Figure 4.7: *Example seismogram of the events of cluster A. Data are P wave aligned and trace-normalized. Displayed are all three components. The coda of each wave train contains complex information on the subsurface.*

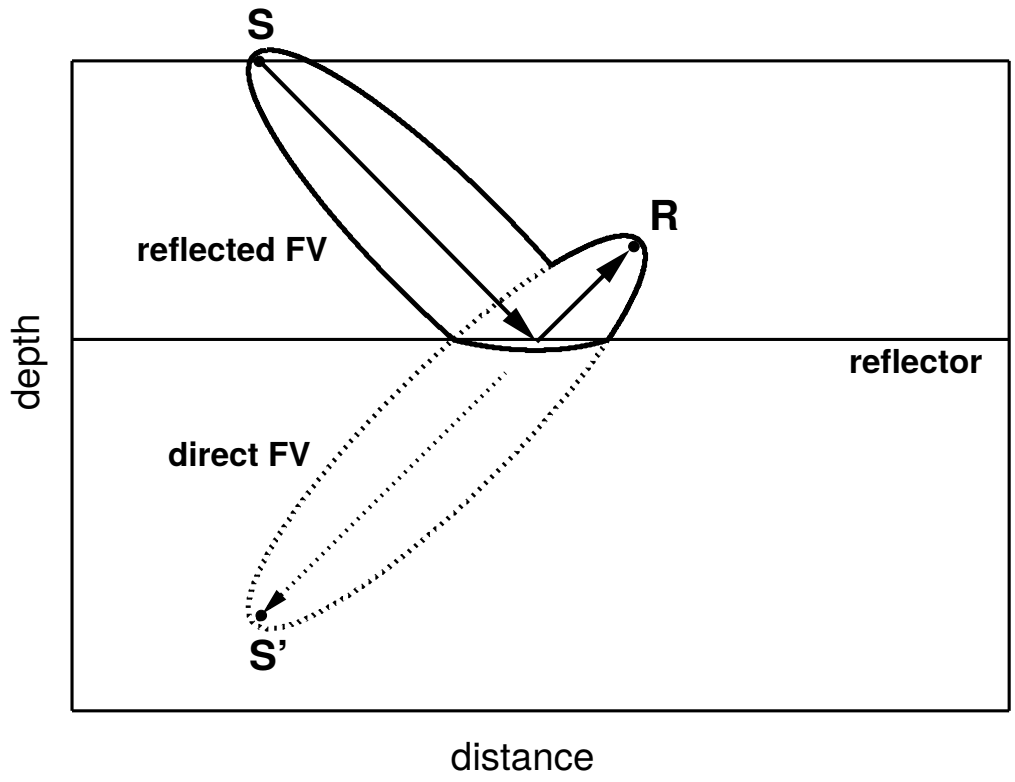

Figure 4.8: *Principle of Fresnel Volume Migration for a short distance to the receiver from Buske et al. (2009).*

reciprocity this is valid also for a short distance from the event (source) to the reflector and a larger distance from the reflector to receiver. The image illustrates the case with a low velocity contrast, however, for a larger velocity contrast the center of the estimated Fresnel zone remains correct.

4.4.2 Imaging Reflections Recorded at OT2

From polarization analysis of cluster A I identify the signal between 0.41 and 0.43 s as a PP reflection (see Figure 4.10). In order to estimate the polarization for each 3-component seismogram, pre-processing is required. As suggested by Reshetnikov et al. (2015), a band-pass filter (from $16 - 87$ Hz) and a notch-filter (center frequency at 55 Hz) are applied. From the polarization the slowness can be computed.
I image the corresponding reflector by migrating only the PP reflection time window using the Fresnel Volume Migration. The illuminated reflector coincides with a previously imaged reflector, as shown in in Figure 4.9 by a stack of migrated events of cluster A.

In addition to the location of the reflector, also the events, which illuminate the reflector, are known.

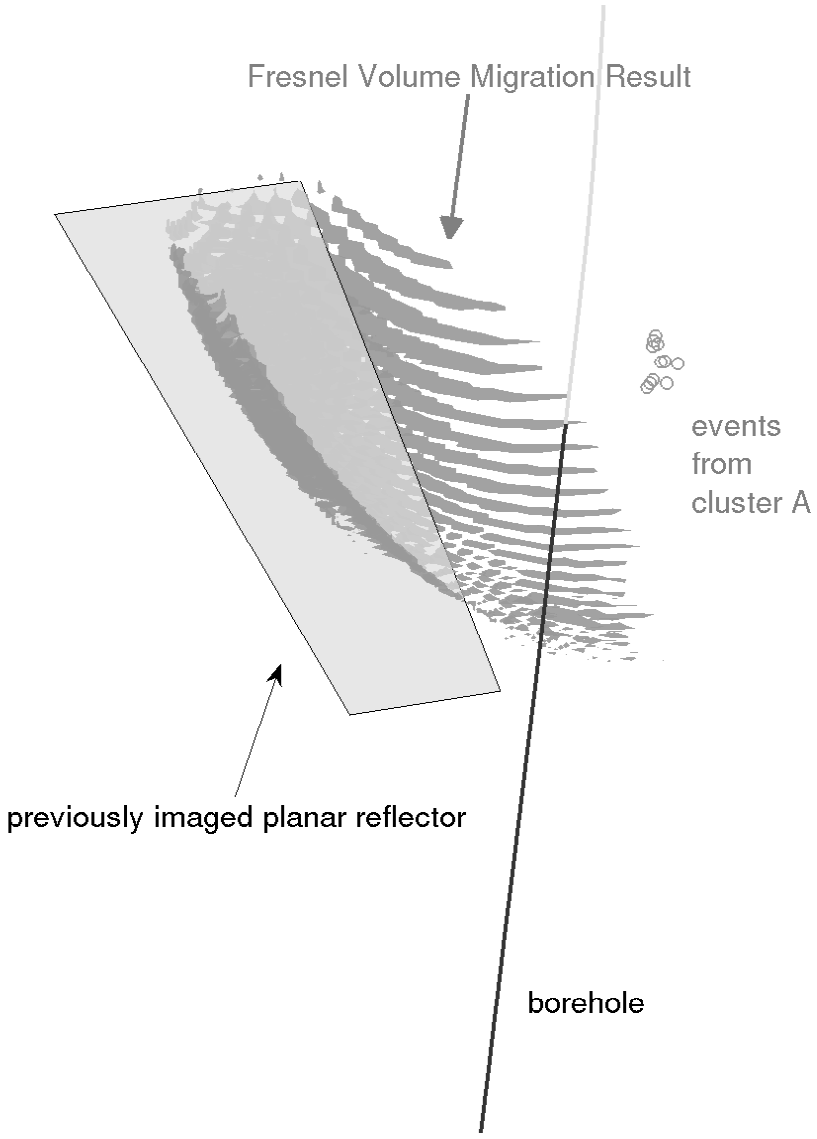

Figure 4.9: *Isosurface of the zone of high reflectivity, imaged using FVM of the PP reflected phases from cluster A (gray shade), coincides with a previously imaged planar reflector (gray plane).*

4.5 Estimation of Reflection Coefficient

The *apparent* reflection coefficient R_{apparent} can be extracted directly from the waveforms. It is the ratio of the amplitudes of reflected and incident wave:

$$R_{\text{apparent}} = \frac{A_{\text{reflected}}}{A_{\text{direct}}},$$

where A denote the maximum of the absolute amplitudes. However, the amplitudes which are recorded by the receiver have already traveled through the medium and therefore experienced some effects which have influence on their amplitudes. I speak here of geometrical spreading and intrinsic attenuation which is different for the direct and reflected wave since they travel different ray paths, and the influence of the source mechanism, since the direct wave is probably emitted with another amplitude than the reflected wave since their direction is (slightly) different. To obtain the *true* reflection coefficient R_0, the apparent reflection coefficient has to be corrected:

$$R_0 = R_{\text{apparent}} \cdot G^{-1}_{\text{Geometry}} \cdot I^{-1}_{\text{Intrinsic}} \cdot S^{-1}_{\text{Source}}$$

In the following I will describe in detail, how each correction can be obtained and the true reflection coefficient for the example cluster is estimated.

4.5.1 Apparent Reflection Coefficient

The *apparent* reflection coefficient can be extracted directly from the waveforms. Compared to the waveforms shown in Figure 4.10, we expect the ratio between reflected and direct wave to be quite high, since we can observe the reflection easily in on the recorded z-component. The apparent reflection coefficient for cluster A can be found to be:

$$R_{\text{apparent}} = \frac{A_{\text{reflected}}}{A_{\text{direct}}} = 0.31$$

4.5.2 Geometrical Spreading

The amplitude changes between direct and reflected rays due to geometrical spreading are accounted for by introducing the correction term G_{Geometry}. This term can be determined from the positions of the source, the receiver, and the reflector (see Figure 4.11 for an illustration of the different ray paths for the direct and reflected wave).

From imaging the reflected waveforms from cluster A, we know which reflector is illuminated by these events and can thus easily calculate the traveled ray paths. Considering the geometrical spreading, each amplitude decays with $1/r$, so the

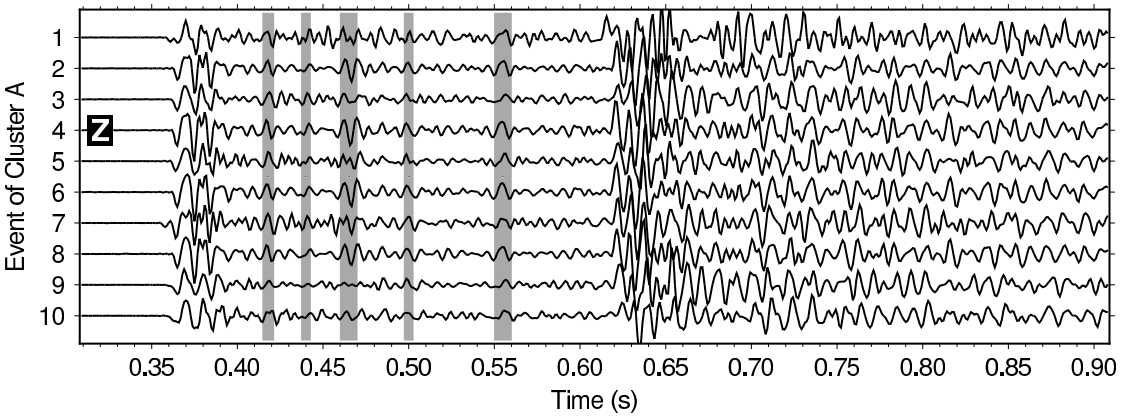

Figure 4.10: *Seismogram of the depth-component of the events of cluster A. Data are P wave aligned and trace-normalized, coherent signals are highlighted.*

correction term becomes:

$$G_{\text{Geometry}} = \frac{r_{\text{direct}}}{r_{\text{reflected}}} = 0.86$$

4.5.3 Intrinsic Attenuation

Following Shearer (2009), the intrinsic attenuation can be calculated by:

$$A(x) = A_0 e^{-\omega x/2cQ}$$

where c denotes the velocity, x the path length, and $Q = 500$, which is the quality factor for granite (Zillmer et al., 2002). The difference in attenuation for the direct and reflected wave results from their difference in traveled ray path, as illustrated in Figure 4.11:

$$I_{\text{Intrinsic}} = \frac{I_{\text{reflected}}}{I_{\text{direct}}} = \frac{I_0 e^{-\omega r_{\text{reflected}}/2cQ}}{I_0 e^{-\omega r_{\text{direct}}/2cQ}} = e^{-\omega \Delta x/2v_{\text{p}}Q},$$

with $\Delta x = r_{\text{reflected}} - r_{\text{direct}}$, the difference in traveled ray path. The attenuation correction $I_{\text{Intrinsic}}$ in our case is:

$$I_{\text{Intrinsic}} = 0.93$$

4.5.4 Source Characteristics

The correction term S_{Source} accounts for the different amplitudes due to the directional characteristics of the source. Rusu (2012) has determined the source mechanisms for the largest clusters at the Basel reservoir. The author has shown by random testing, that events from clusters (which are determined by waveform similarities) have similar focal mechanisms. In Figure 4.12 the

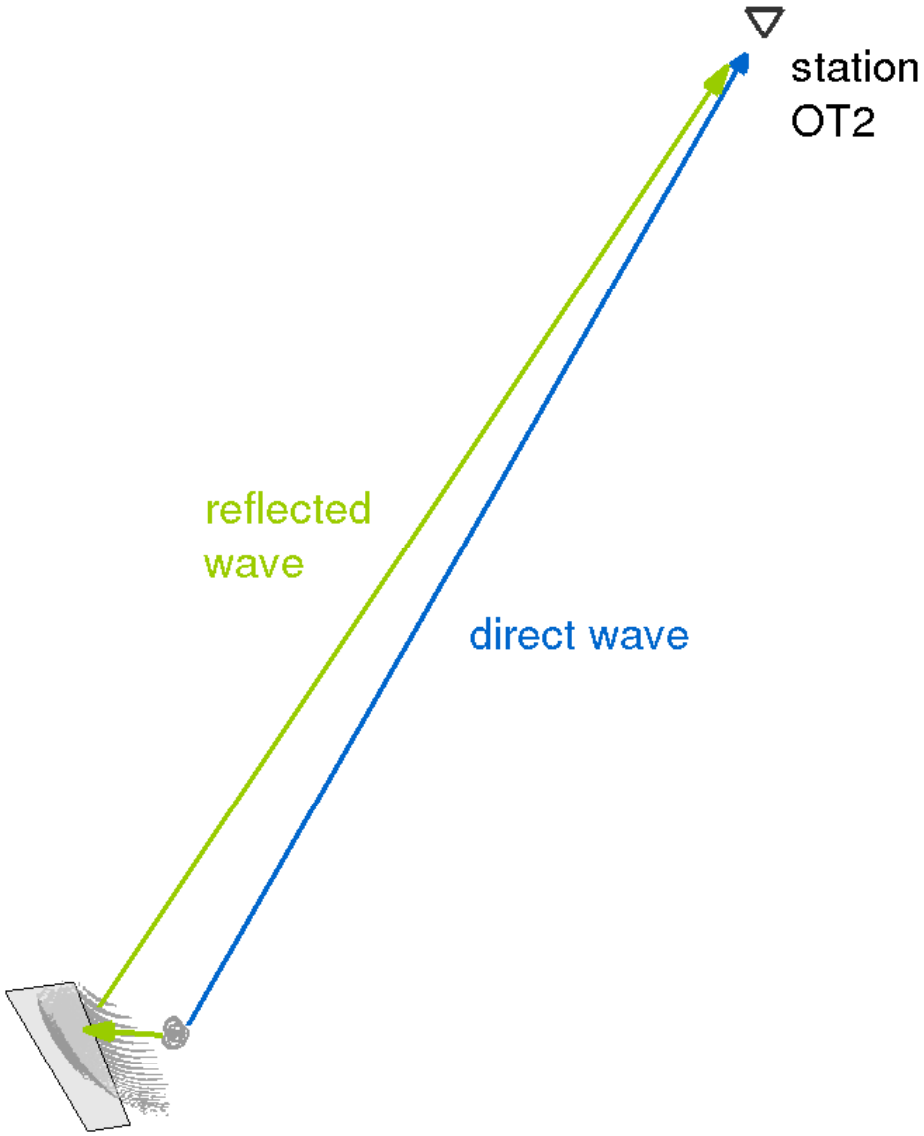

Figure 4.11: *Schematic ray path for the direct and reflected wave, that is emitted by cluster A and recorded at station OT2.*

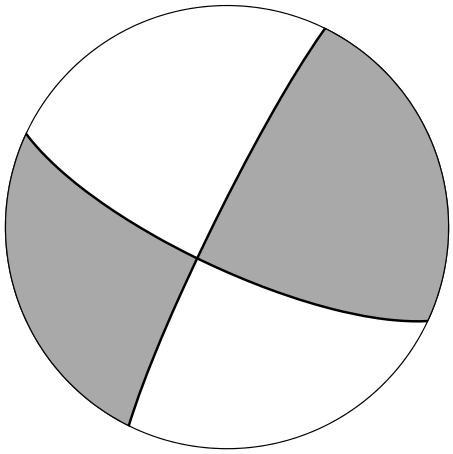

Figure 4.12: *Beach ball representation (lower hemisphere) of the fault plane solution of cluster A.*

beach ball representation of the fault plane solution of cluster A is plotted.

In combination with the far field radiation pattern (Aki and Richards, 2002),

$$\begin{aligned} A(\phi, \delta, \lambda, \theta_{\mathrm{R}}, \phi_{\mathrm{R}}) &= \cos\lambda \sin\delta \sin^2\theta_{\mathrm{R}} \sin 2(\phi - \phi_{\mathrm{R}}) \\ &- \cos\lambda \cos\delta \sin 2\theta_{\mathrm{R}} \cos(\phi - \phi_{\mathrm{R}}) \\ &+ \sin\lambda \sin 2\delta (\cos^2\theta_{\mathrm{R}} - \sin^2\theta_{\mathrm{R}} \sin^2(\phi - \phi_{\mathrm{R}})) \\ &+ \sin\lambda \cos 2\delta \sin 2\theta_{\mathrm{R}} \sin(\phi - \phi_{\mathrm{R}}), \end{aligned}$$

where $\phi = 115°, \delta = 75°, \text{and } \lambda = 175°$ are strike, dip, rake of cluster A, and $\theta_{\mathrm{R}}, \phi_{\mathrm{R}}$ are the take-off and azimuth angles, I can determine the corresponding correction term. The different amplitudes due to different directions of the direct and reflected wave are illustrated in Figure 4.13. Sketched is the amplitude distribution in the event-reflector-receiver plane, in which the direct and reflected wave travel to the station OT2.

For this specific example cluster, the correction term of the source is:

$$S_{\mathrm{Source}} = \frac{A_{\mathrm{to\ Reflector}}}{A_{\mathrm{to\ Receiver}}} = 3.09$$

One can see that this correction term has a notable influence. If the considered ray path is close to the nodal plane, the amplitude is sensitive to the exact locations and of course to the determination of the focal mechanism itself. In the Basel example the station distribution that was used to find the fault plane solution has a good spatial coverage. The deviation of the solution for each event from the mean of the whole cluster is in the order of a degree.

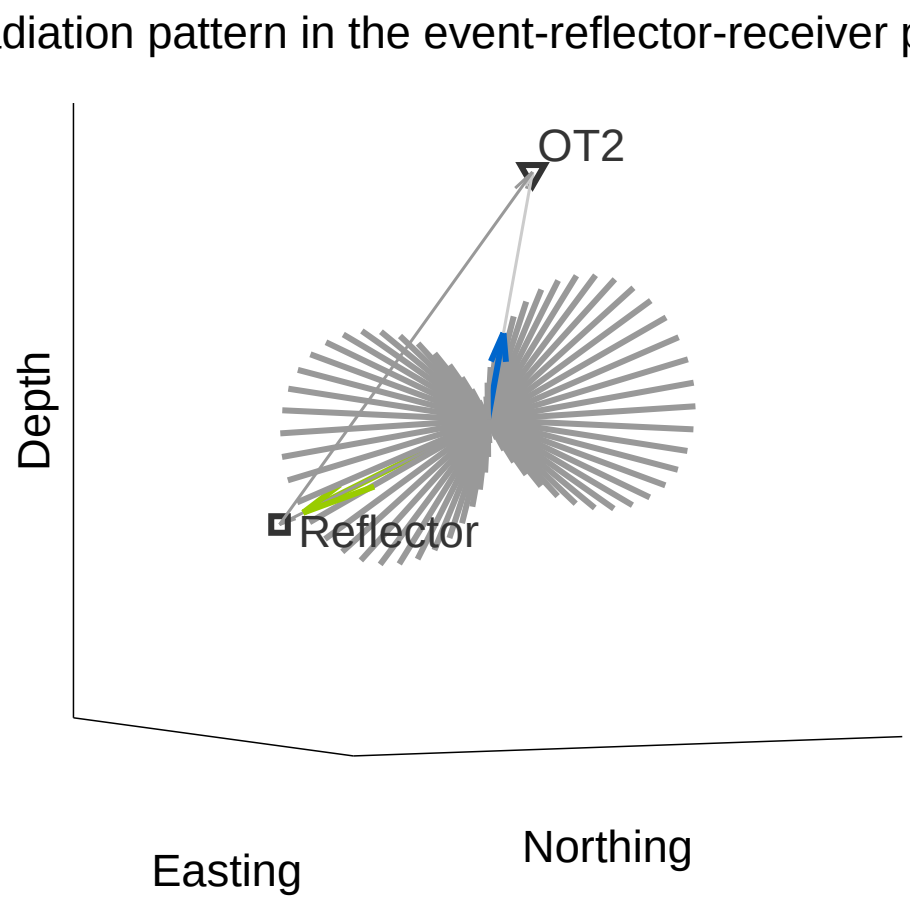

Figure 4.13: *Amplitude distribution in the event-reflector-receiver plane, in which the direct and reflected wave travel to the station OT2.*

4.5.5 True Reflection Coefficient

In the current example cluster A, the averaged and corrected reflection coefficient at the main frequency of $100\,Hz$ and an angle of incidence $\theta = 22°$ is:

$$R_0 = R_{\text{apparent}} \cdot G^{-1}_{\text{Geometry}} \cdot I^{-1}_{\text{Intrinsic}} \cdot S^{-1}_{\text{Source}} = 0.13 \pm 0.02$$

This number is calculated by averaging over the reflection coefficient R_0 from each event-receiver-pair, the error is calculated using the standard deviation. The result of $R_0 = 0.13$ seems to be a reasonable number. However, this value of reflectivity is dependent on the frequency and angle of incidence, thus the reflectivity as it is seen on station OT2.

4.6 Interpretation of the Reflection Coefficient

As it was stated above, in order to produce reflective signals at a sufficient level, the wave must experience a strong impedance contrast. In agreement with the study of Reshetnikov et al. (2015), in the case of a fluid filled fracture, this condition would be fulfilled. A planar thin fluid filled fracture would have a strong enough velocity contrast to produce a measurable reflection signal within the coda. The fact that the illuminated reflector is in the target area, which means the seismically active area, and in the vicinity of the open hole, supports the idea that the velocity contrast is produced by a fluid.

I now compare the number of estimated reflection coefficient to the theoretical reflection coefficient $R_{\text{pp0}}(h)$ at the given background properties and geometrical settings. The result is shown in Figure 4.14.

From the estimated reflection coefficient at the given constraints, we can infer for a reflector width of:

$$h = 0.05\ m$$

For a single fluid-filled fracture at several kilometers depths, it seems quite a high value. It is hard to imagine that under whatever the injection pressure is, a fracture of several centimeters width exists in this granite environment.

However, if this is a weak or fractured zone, which consists out of several fluid filled fractures, than the wave with a wavelength of about 60 m experiences this complex fracture as one effective fracture. That is to say from the estimated reflectivity $R_0 = 0.13$ at the reflector A, we can infer an effective, fluid filled fracture width of $h = 0.05\ m$.

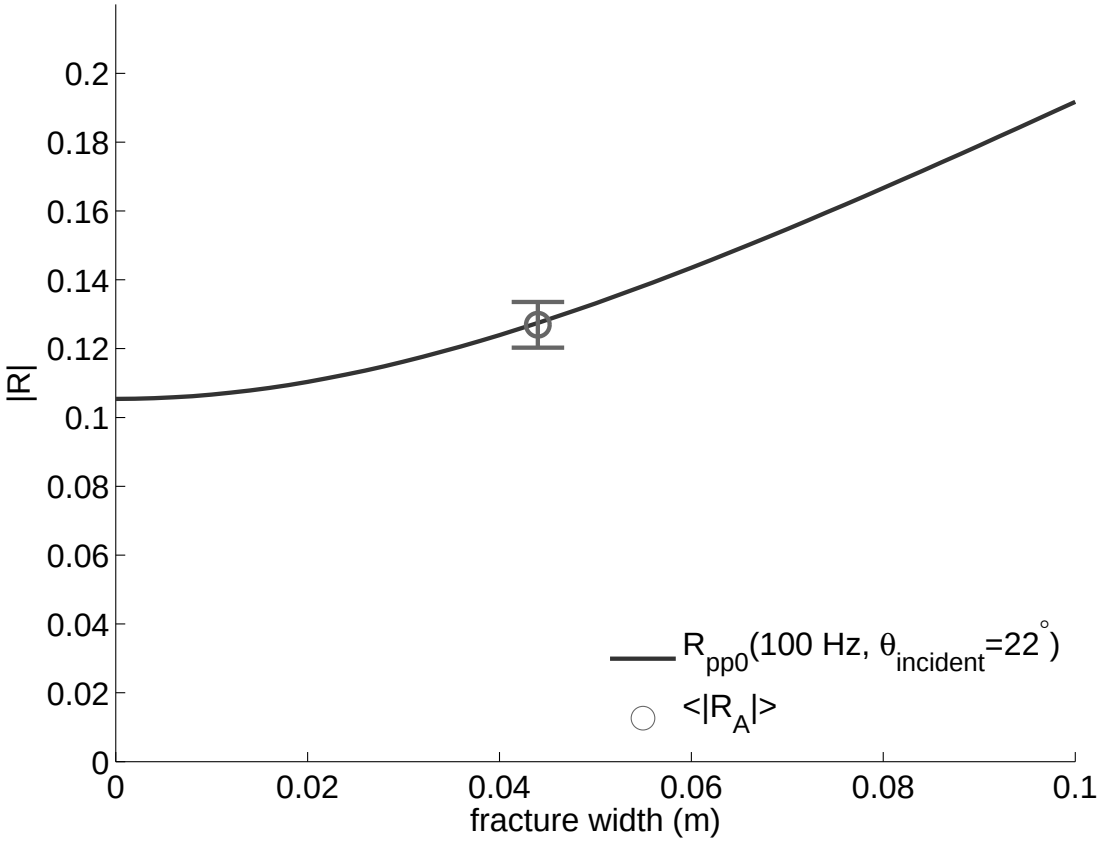

Figure 4.14: *Estimated reflection coefficient of reflector A in comparison to the theoretical reflection coefficient $R_{\mathrm{pp0}}(h)$ at the given background properties and geometrical settings.*

4.6.1 Map of Reflectors

In the above section, I described in detail the following work flow for the exemplary cluster A:

- Identification of reflected phases within waveforms
- Imaging of reflected phases
- Calculation of *apparent* reflection coefficient
- Correction for geometrical spreading, radiation pattern, and attenuation
  $\rightarrow$ *true* reflection coefficient
- Comparison to theoretical reflection coefficient
  $\rightarrow$ reflector width

I also applied this work flow to other clusters B and C of the Basel data set. The corresponding imaged reflectors coincide with other previously imaged zones of high reflectivity. The resulting map of reflectors and their reflectivity is plotted in Figure 4.15 in a depth and a 3D view. Again, it is crucial to keep in mind, that the plotted values of reflectivity are as they are observed by the station OT2, this means that the angle of incidence can become quite high and thus high reflection coefficients are expected.

After the translation from reflectivity to fracture width (see Figure 4.16), it becomes obvious, that I have to interpret the width as an effective fracture width. It is very unlikely that even in the direct vicinity of the borehole a single fracture of a meter width exists. However, for the 60 m long wave, a complex fractured one meter thick zone is seen as one effective fracture.
The results of the three processed clusters can be found in Table 4.2:

Cluster	R_0	θ / °	ϕ / °	δ / °	λ / °	h_{eff} / m
A	0.13$\pm$0.02	16	116	75	175	0.05
B	0.23$\pm$0.07	47	256	49.5	-174.5	1.3
C	0.24$\pm$0.05	48	199.6	25.9	24.9	1.0

Table 4.2: *Properties of the imaged reflectors and their corresponding clusters.*

4.7 Comparison to the Linear Slip Model

If one assumes slip condition at the fracture, and, for simplicity, normal incidence of the reflected wave, one can determine the normal compliance and width

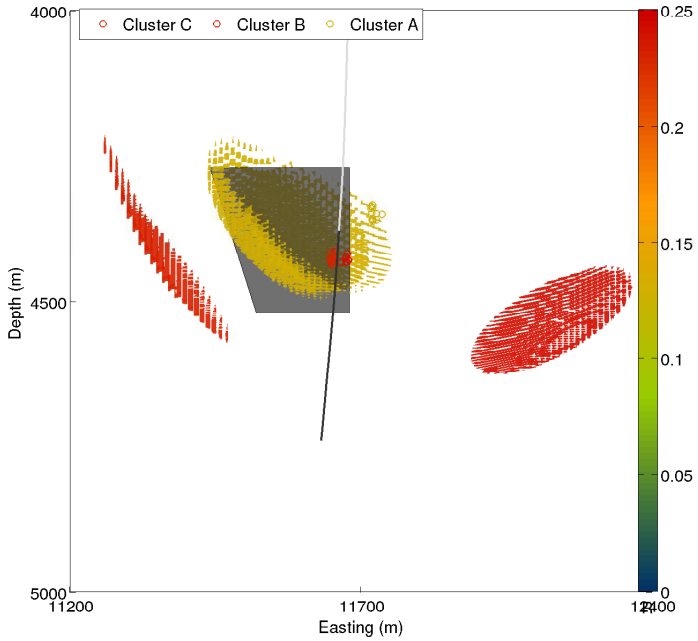

(a) Depth view.

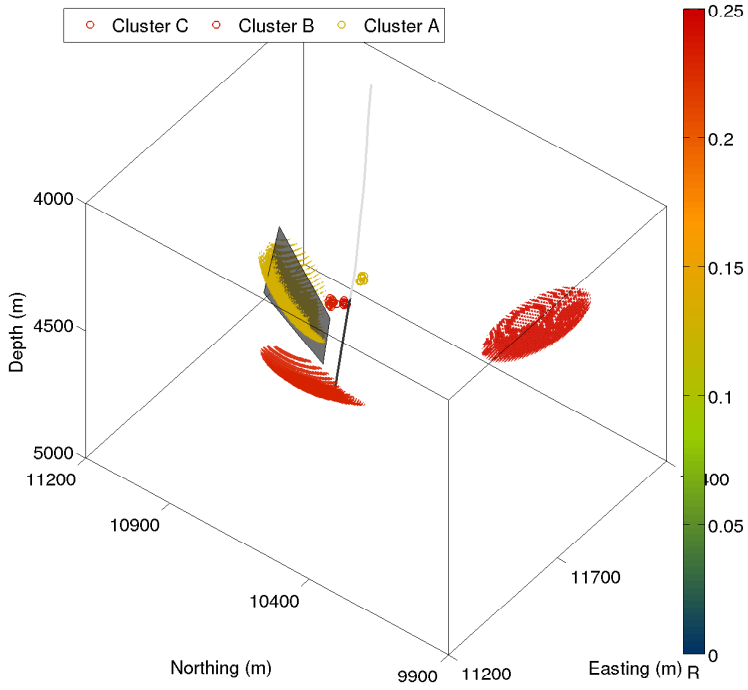

(b) 3D view.

Figure 4.15: *A map of reflectors in the vicinity of the borehole Basel 1 (gray line, open hole section in black). The microseismic events illuminating each reflector are plotted as circles in the corresponding color. The color represents the level of reflectivity.*

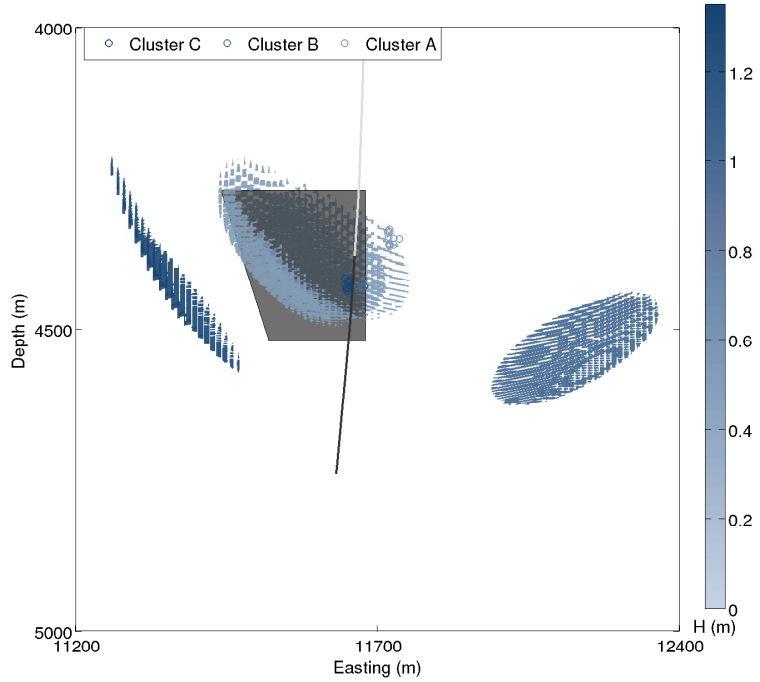

(a) Depth view.

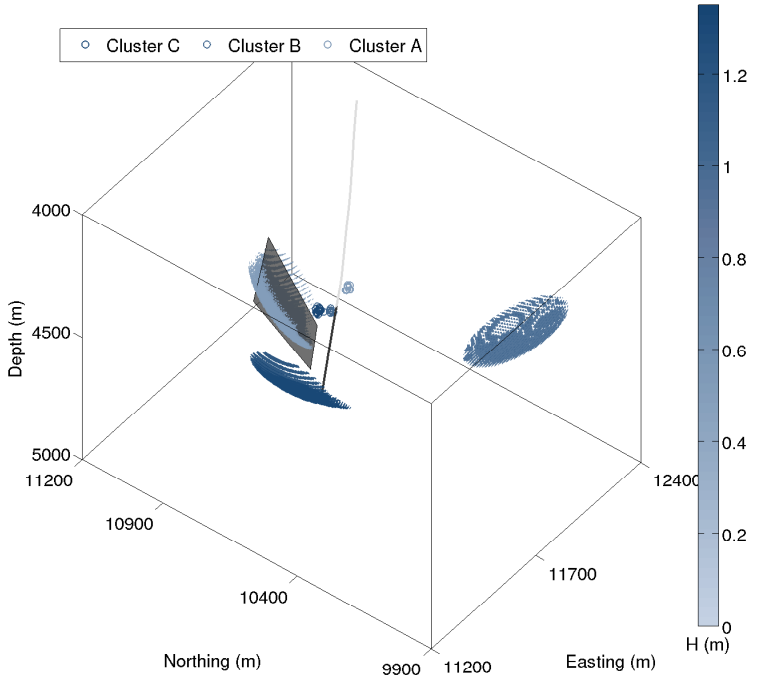

(b) 3D view.

Figure 4.16: *A map of reflectors in the vicinity of the borehole Basel 1 (gray line, open hole section in black). The microseismic events illuminating each reflector are plotted as circles in the corresponding color. The color represents the effective fracture width.*

of the fractured zone. Following Schoenberg (1980), I obtain for a reflection coefficient of $R_0 = 0.13$:

$$\eta_{\mathrm{N}} = \frac{2R(0°)}{i\omega\rho_{\mathrm{f}}v_{\mathrm{f}} + R(0°)i\omega\rho_{\mathrm{f}}v_{\mathrm{f}}}$$

$$|\eta_{\mathrm{N}}| = 2.06 \cdot 10^{-11}\frac{m}{Pa}$$

This compliance characterizes the fracture induced anisotropy of the reservoir and should be homogeneous within the fractured zone. In their study Yu and Shapiro (2015) determine the fracture induced anisotropy of shale in addition to the fabric anisotropy in the Horn River Shale. They compare their absolute value of fracture compliance to different other studies. If I classify the above obtained compliance value in comparison to these other studies (Figure 4.17, after Yu and Shapiro (2015)), it fits quite well to their results. With an increasing (effective) fracture size, the value of compliance should increase, too. I assume the fracture length to be in the order of $10^1\,m$ and find the compliance between low values obtained from microseismic and lab scale data from shale and high values from major fracture zones, which is a reasonable result.

Implementing the exact formula for a finite fracture width within the Linear Slip Model (LSM), I also obtain:

$$h_{\mathrm{LSM}} = \eta_{\mathrm{N}}\rho_{\mathrm{f}}v_{\mathrm{f}}^2 = 0.05\,m\ .$$

This value is in the same order as the value determined using a single fluid filled fracture model. Usually, compliances are determined to estimate the upper limit of anisotropy of the reservoir. In this case, the reflectivity of a reflector yields the compliance value for a fractured zone and thus the fracture zone width.

4.8 Summary: Application to the Basel ESG

I have re-processed the passive seismic reflection data from the Basel EGS. Selected event clusters were re-analyzed in terms of reflections within their P wave coda. In order to do that, the data were depth migrated using the Fresnel Volume Depth Migration and the locations of reflectors were obtained. Once the locations of the reflectors were known, I could compute the correction terms accounting for the changes in amplitude due to different damping and geometrical spreading of the direct and reflected wave and the difference in amplitudes of direct and reflected wave caused by the focal mechanism of the events.

For an example cluster I have extracted the apparent reflection coefficient directly from the waveform, corrected this coefficient for the above mentioned

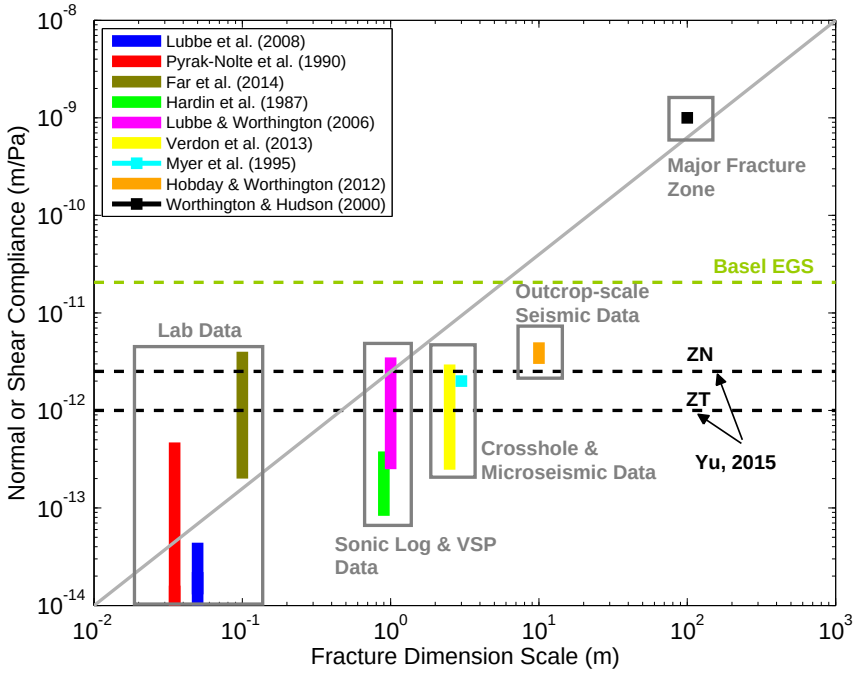

Figure 4.17: *Classification of normal compliance derived by reflection coefficient estimate (green line) in comparison to other studies, modified after Yu and Shapiro (2015).*

effects and obtained a true PP reflection coefficient of $R_0 = 0.13$. For an effective, fluid filled fracture this yields a width of $h = 0.05\ m$. Analogously I have re-processed two other clusters and discussed the results.

By comparison to the Linear Slip Model, where the compliance is determined from the reflectivity and the effective fracture width from the compliance, I obtained the same result. The resulting effective width of $0.05\ m$ of a fracture in the direct vicinity of the borehole is a reasonable result.

5. Isotropic Case: Application to the Natural Occurring Seismicity at the SAFOD

In this chapter I analyze the P wave coda of naturally induced seismic events occurring at a major fault zone in terms of reflection coefficients.

Major fault zones, especially at active tectonic boundaries, gain special interest from researchers and public. Active faults are considered to be a geologic hazard since the stress release can potentially cause earthquakes, landslides, or rockfalls for example. The occurring earthquakes can be energetic and destructive, causing death an damage: In the $M_W = 7.0$ 2010 Haiti earthquake, occurring at the Caribbean and the North American plate boundary, 316,000 people were killed, 300,000 were injured, and 97,000 houses were destroyed (USGS, 2015a). Generated at the fault that conveys the Nazca plate eastward and downward beneath the South American plate, the $M_W = 8.8$ 2010 Maule earthquake caused more than 500 peoples death, about 120,000 injuries, and the damage or destruction of at least 370,000 houses (USGS, 2015b). The 6.3 magnitude aftershock 2011 in Christchurch, New Zealand, at the plate boundary between the Pacific and Australian plate resulted in destruction, injuries and deaths (GNS Science, 2011).

Despite of the danger that affects the lives of communities around the world, for scientists active faults provide excellent areas to study the processes controlling the plate motion for a better understanding of what is going on in the subsurface. This knowledge can than be used for example in estimating geohazards, which are not only a scientific but also a public issue.

Deep fault drilling projects aim to better understand active faults and earthquakes. Analysis of mineralogy and deformation mechanics can be performed through drilling. Additionally, stress states and pore pressures can be measured, and occurring seismicity, its physics of nucleation and rupture, can be monitored closely (Zoback et al., 2010). A list and report of planned and conducted drilling projects addressing the above questions can be retrieved from `www.icdp-online.org`.

One example of an active fault zone and its associated drilling project is the Alpine Fault, South Island, New Zealand, which is one of the largest active fault zones on earth. It is the transform boundary between the Australian plate to the north and the Pacific plate to the South. The Alpine Fault is situated along West Coast of the South Island of New Zealand and runs more than 460 km parallel to the coast. Major ruptures in AD 1430, 1620 and 1717 have been related to the Alpine Fault (R. Sutherland et al., 2007). Thus, major earthquakes, such as a magnitude 7.1 earthquake 40 km west of Christchurch on September 4th 2010, mentioned above, occur with a periodicity of about 300 years, which implies a significant geohazard potential. Scientific drilling programs at the Alpine Fault aim to better understand fundamental processes of rock deformation, seismogenesis, and earthquake deformation. The main goals are not exclusively for scientific but in a long term also for significant public safety reasons.

The probably most studied fault in the world, the San Andreas Fault, California, has also been target of a drilling program and provides microseismic reflection data which I can interpret in terms of reflection coefficients.

5.1 Introduction to the Data Set

In order to study plate-bounding processes at seismogenic depth, the Earth-Scope's San Andreas Fault Observatory at Depth (SAFOD) drilled into the San Andreas Fault (SAF) immediately north of Parkfield, California, see Figure 5.1. The ability to drill through a zone close to frequent repeating M$\sim$2 microearthquakes at relatively shallow depths has been an important criterion in the drill site selection (Zoback et al., 2010). The SAFOD project intended to directly study the physical and chemical processes of the active San Andreas Fault at depth. The main goals are listed by Zoback et al. (2011) and include, besides the study of structure and composition of the San Andreas Fault at depth, also the determination of the origin of fault-zone pore fluids. Drilling into an active plate-bounding fault zone had never been attempted before. The SAFOD drilling should provide a comprehensive case study on future scientific drilling into active fault zones.

A near-vertical and 2.2 km deep pilot hole was drilled in 2002 approximately 2 km away from the surface trace of the San Andreas Fault. After answering a number of technical, operational and scientific questions, the location for the SAFOD drilling was confirmed appropriate. The drilling of the main hole has been conducted in three distinct phases, carried out in the summers of 2004, 2005, and 2007. Each phase was clearly separated from another and consequent phases were planned considering the experiences from the previous drilling phase. Figure 5.2 shows the locations of the different holes and their location within the geologic setup.

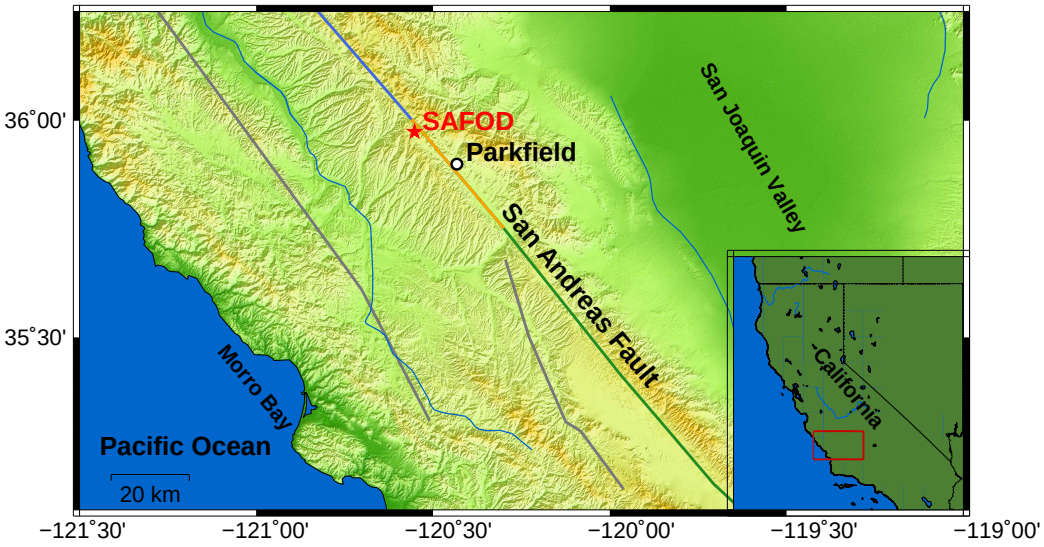

Figure 5.1: *Location of the San Andreas Fault, California. The borehole is located in the Southwest of the surface trace of the SAF. The transition zone is denoted by the orange line and separating the part of the San Andreas fault which is characterized by aseismic creep (blue) and the locked part (green).*

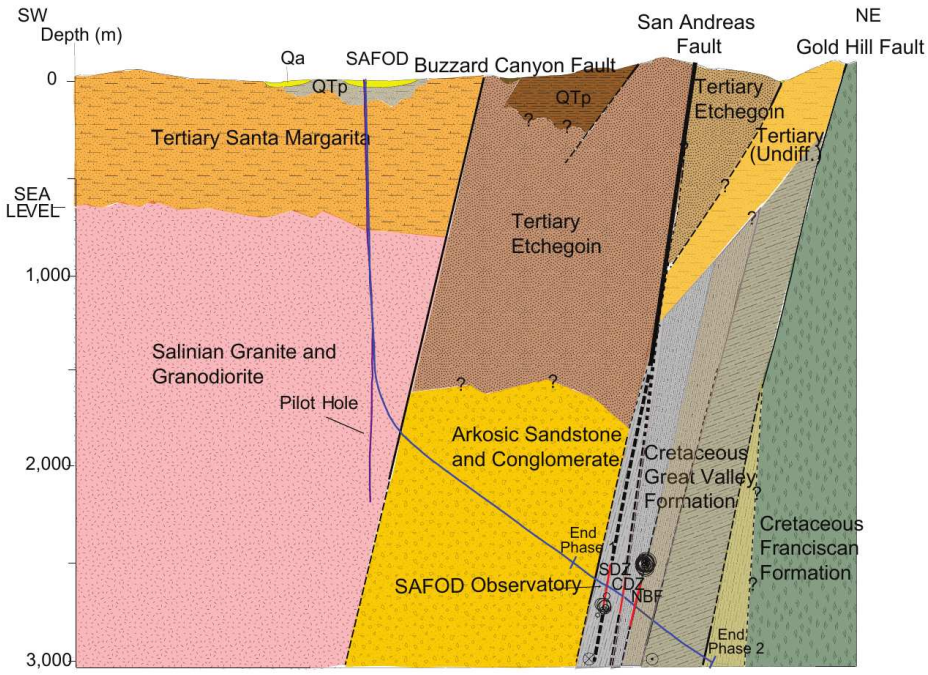

Figure 5.2: *Geologic sketch taken from Zoback et al. (2011). Plotted is a depth section perpendicular to the trajectory of the San Andreas Fault. Geologic units are constrained by surface mapping and core samples from drilling. Black circles denote the zones of repeating microearthquakes. Red fault branches are traces associated with the San Andreas Fault.*

Phase 1 drilled vertically into a depth of $\sim$1.5 km and then steered the well at an angle of $\sim$60° from vertical toward the repeating microearthquakes. The second Phase drilled across the San Andreas Fault Zone during the summer of 2005. The observatory equipment, containing seismometers and accelerometers, was deployed in the borehole within the fault zone. The third phase, carried out during summer 2007, involved multilateral drilling. That means the creation of secondary holes at optimal locations.

Between the end of Phase 1 and the beginning of Phase 2, Paulsson Geophysical Services Inc. (PGSI) deployed an eighty-level, 240-component seismic array in the tilted part of the borehole, see Figure 5.4. Over a five-week period PGSI tested the suitability of this array for recording microearthquakes. Several microearthquakes were recorded during this period. An example event recorded on the array is plotted in Figure 5.3. The P wave hits the receiver array from the bottom and can be identified clearly. The S wave is hardly to recognize on this component. What is striking here, is the strong reflection arrival directly after the P wave. The crossing with the direct wave is a hint, that the reflector is intersecting with the array at exactly the crossing point.

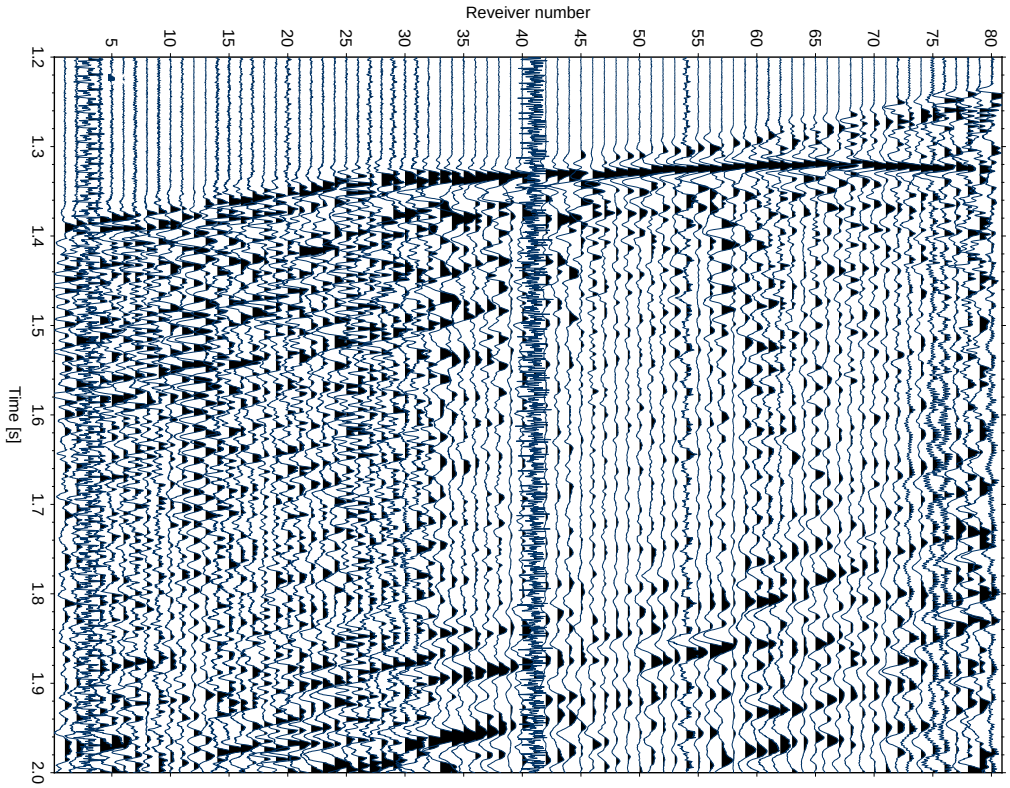

Figure 5.3: *X-component of a microseismic event at the target area, recorded by the PGSI array.*

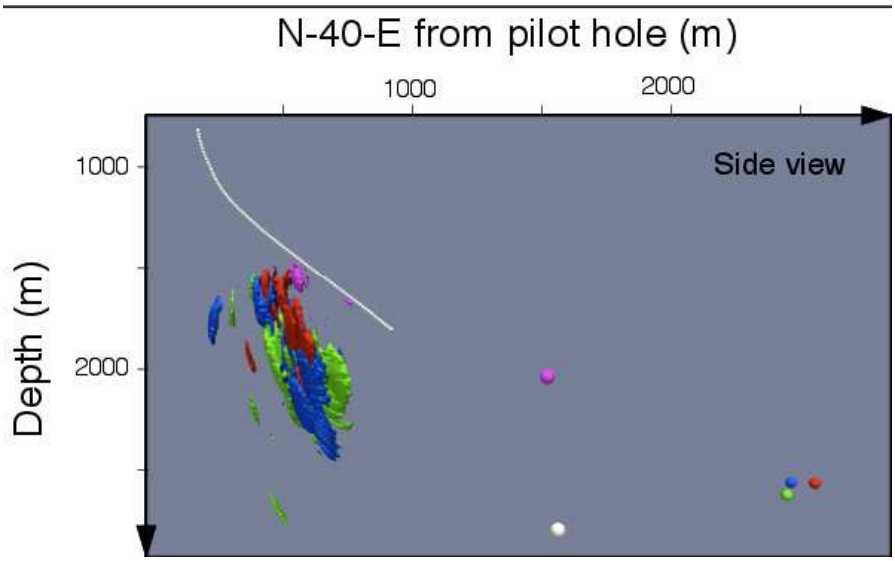

Figure 5.4: *Reflectors imaged in the vicinity of the borehole using microseismic events as a passive source, figure taken from Reshetnikov et al. (2010a). Each event illuminates parts of the reflector, plotted in the corresponding color.*

5.2 Previous Imaging Results

Reshetnikov et al. (2010a) used the microearthquakes recorded on the PGSI array as sources for passive seismic imaging. The authors revealed a quite strong reflector in the vicinity of the borehole.

Their two step passive imaging approach precisely located the events using a modified back propagation Gaussian-beam-type procedure which uses the ray density as a location criterion. Than, in a second step, the Fresnel Volume Migration was applied to each of the six located events. In their paper, only PP reflections are presented. The obtained images are complementing reflectors in the vicinity of the SAFOD main borehole, as shown in figure 5.4, where the isosurfaces of the imaged structures are plotted. Note, that in the sketch the reflector imaged by the sixth event is covered completely by the other reflectors.

Reshetnikov et al. (2010a) compare their results with previous studies and find that their approach provides much higher resolution images and shows fine-scaled structures inside the fault zone. They correlate their stacked images to geological features. Especially the strongest reflector is interpreted to correlate with the possibly complex structure of the Buzzard Canyon Fault, which is crossing the SAFOD main borehole (c.f. Figure 5.2).

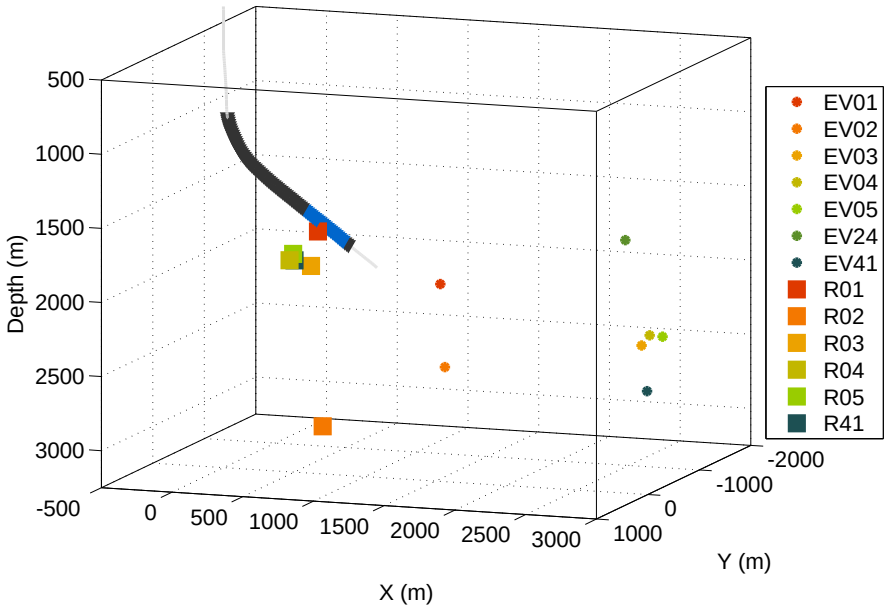

Figure 5.5: *3-D sketch of the SAFOD experimental setup and the previous imaging results. Events are plotted as colored dots, the imaged reflector is plotted as a square in the corresponding color. The receivers (black) are threaded along the main borehole (gray line). Receivers at which direct and reflected wave can be distinguished are plotted in blue.*

5.3 Identification of Reflected Phases

The experimental setup is sketched in a 3-D view in Figure 5.5. The events are plotted as colored dots, the illuminated and imaged reflector is plotted as a square in the corresponding color. For simplicity the reflector is plotted as a point scatterer, which makes it easier to approximate expected wavefields. The receivers (black) at which I can clearly distinguish between direct and reflected wave are plotted in blue, threaded along the main borehole (gray line).

There is one main difference to the previous case study. In the Basel EGS reservoir, a cluster of events was illuminating the same structure. The ray paths for the different events were similar and thus the correction terms were similar. Each event-receiver-pair had the same reflection coefficient and the discussed reflection coefficient is the average coefficient over the whole cluster. In the SAFOD case there is a line of receivers. Each event-receiver-pair in principle illuminates another part of the resulting imaged reflector. For each receiver the actual reflection point shifts slightly and so do the correction terms. I assume that in this slight shift of reflection point the properties of the reflector do not change. In order to test the applicability of my method, I will make some simplifications and obtain a preliminary result during the following sections. The preliminary result shows the tendency in which a detailed evaluation will yield.

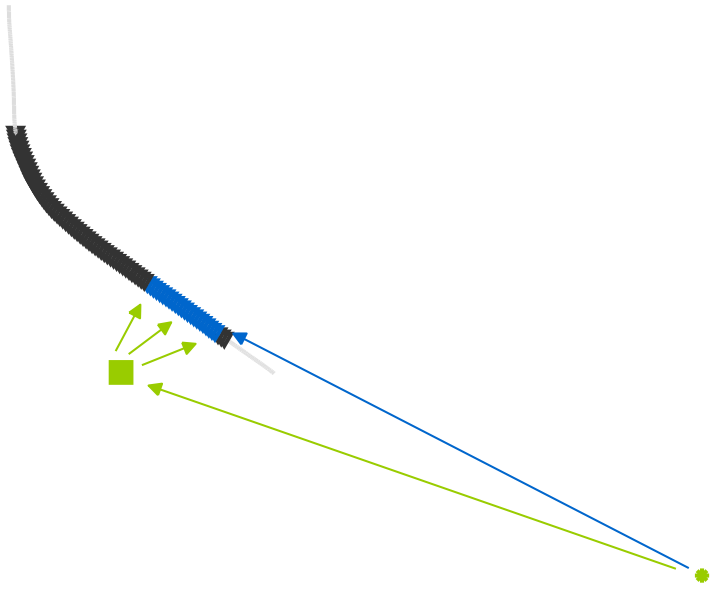

Figure 5.6: *Simplified ray path of one event. Direct ray path (blue) in comparison to the reflected ray path (green), simplified for a point scatterer. Receivers at which I can clearly distinguish between direct and reflected wave are plotted in blue.*

In the following I will make two simplifications, which have to be in mind when interpreting the results. First, I will consider the reflectors as point scatterer in order to simplify some of the calculations. This will not give the perfect results as the imaged reflector rather is an inclined plane (superposition of the signal recorded at different geophones), but one can get a principle idea of what is going on in the subsurface. Second, I assume a homogeneous and isotropic velocity in the vicinity of the borehole. Although we are in a complex fault area, this approximation is valid since the events are all located in the same target area and I assume that the waves travel similar ray paths and experience similar features. Affected is mainly the dip angle at the receiver which will play a role in the determination of the fault plane solution. In a true heterogeneous velocity model, deviations from the simplified ray paths will occur but will then affect each receiver and thus the trend of the correction terms is not affected by the assumption of a homogeneous and isotropic velocity in the vicinity of the borehole in order to obtain a preliminary result of reflection coefficient.

In Figure 5.6 the simplified ray path of one event is sketched. The direct P wave reaches the lower part of the receivers first. The reflected waves will have the smallest P-PP travel time difference at receivers closest to the reflector in the case of a point scatter. In reality we have a reflector intersecting the borehole, which means, that the PP reflection will converge to the direct P wave.

For the case of a point scatterer and a constant velocity around the borehole, the velocity-normalized travel time curves are plotted in Figure 5.7. As expected, the P wave arrives first at the lowermost receiver and latest at the uppermost receiver. The S wave arrival follows after the $v_\mathrm{p}/v_\mathrm{s} = 1.83$ (taken from Rentsch et al. (2010)) expected time difference. The two-way travel time for the reflected PP wave looks very similar to the real arrival times in the recorded seismograms (c.f. Figure 5.3). Furthermore, the smallest P-PP travel time difference is at the receiver closest to the reflector, which is due to the point scatterer approximation. For a planar reflector I can thus expect a PP reflection converging to the direct wave at the receiver where the reflector intersects the receiver array. In reality the reflection point shifts slightly for each receiver and the superposition of all reflections gives the planar reflector. However, these approximated travel times match the waveforms which we can see in the recorded seismograms and I will evaluate the PP reflection of this exemplary event in more detail during the following sections.

5.4 Estimation of Reflection Coefficient

As in the section before, in order to estimate a reflection coefficient for the revealed reflector, I need to perform the following steps:

a Identification of reflected phases within waveforms

b Imaging of reflected phases

c Calculation of *apparent* reflection coefficient

d Correction for geometrical spreading, radiation pattern, and attenuation
$\rightarrow$ *true* reflection coefficient

e Comparison to theoretical reflection coefficient
$\rightarrow$ reflector width

The step *a* is resolved. However, for the steps *b* – *e* the starting position changes slightly as mentioned above: In this case, I have one event and several spatial distributed receivers, whereas in the Basel configuration I had one receiver and a cluster of events.

As the receivers are spatially distributed, I cannot calculate a mean apparent reflection coefficient and then apply mean correction terms. Instead, I have to calculate an apparent reflection coefficient for each receiver as each receiver records a reflection at a slightly shifted reflection point. For each receiver I have to calculate a slightly different correction term for the geometrical spreading and attenuation as the traveled ray paths differ from receiver to receiver (c.f. Figure 5.6) and of course, the amplitude correction changes from receiver to receiver.

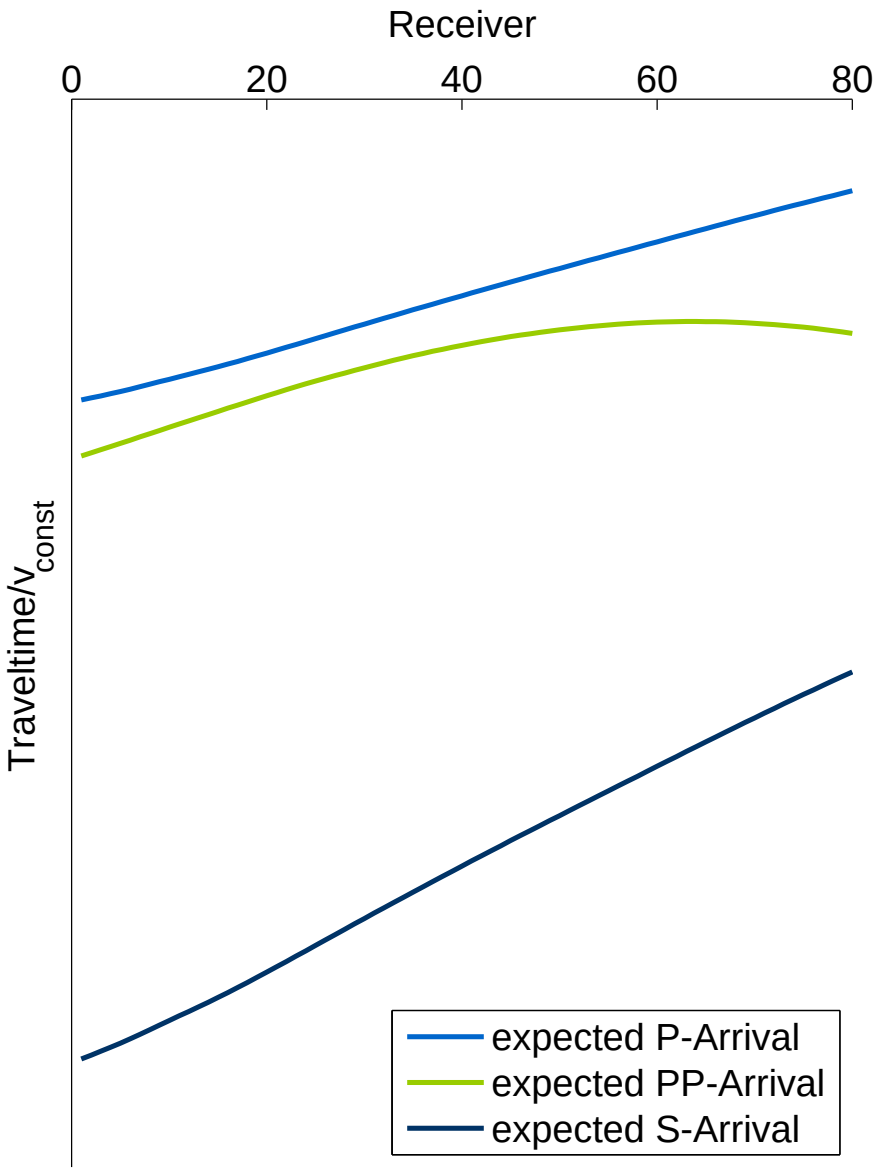

Figure 5.7: *Approximated, velocity-normalized travel time curves. Direct P wave (light blue), direct S wave (dark blue) and reflected wave arrival (green) are plotted for the case of a point scatterer.*

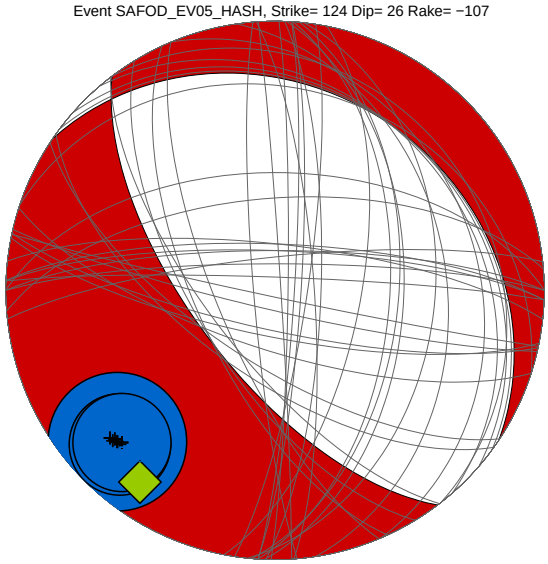

Figure 5.8: *The beach ball representation (upper hemisphere) of the fault plane solution of the exemplary event as determined using HASH. Receivers are denoted by crosses surrounded by blue rings representing the size of the S/P - amplitude ratio. The green diamond denotes the location of the reflector. Grey lines show solutions for small perturbations of the take-off angle.*

5.4.1 Source Characteristics

The source mechanisms of the selected events were not known to me, except that the events in the target area are supposed to have similar mechanisms. For the exemplary event I transferred the seismogram components into the LQT system in order to determine the S/P - amplitude ratio. Additionally I picked the polarity of the P wave first arrival. After personal communication with W. Bloch the fault plane solution of the exemplary event could be determined to $\phi = 124°, \delta = 26°, \text{and } \lambda = -107°$, assigning the strike, dip, and rake, using the HASH algorithm (Hardebeck and Shearer, 2003), introducing a relatively large error which I discuss below. The beach ball representation (upper hemisphere) of the solution given by HASH is plotted in Figure 5.8.

The error of the determined fault plane solution is quite high: As one can see on the location of receivers (crosses surrounded by blue circles; the radius of the circle is proportional to to square root of the P/S amplitude ratio), the coverage of the focal sphere is very limited as the event occurs in the prolongation of the borehole and the emergence angle at the receivers is very similar. Small perturbations in the take-off angle result in relatively high changes of the fault plane solution (gray lines). The green diamond in Figure 5.8 denotes the direction to the reflector on the focal sphere and this location is very similar to the location of the receivers. This means that perturbations in the take-off angle influence both the amplitudes toward the receiver and the amplitudes toward the reflector in the same way. The roughly estimated fault plane solution is thus

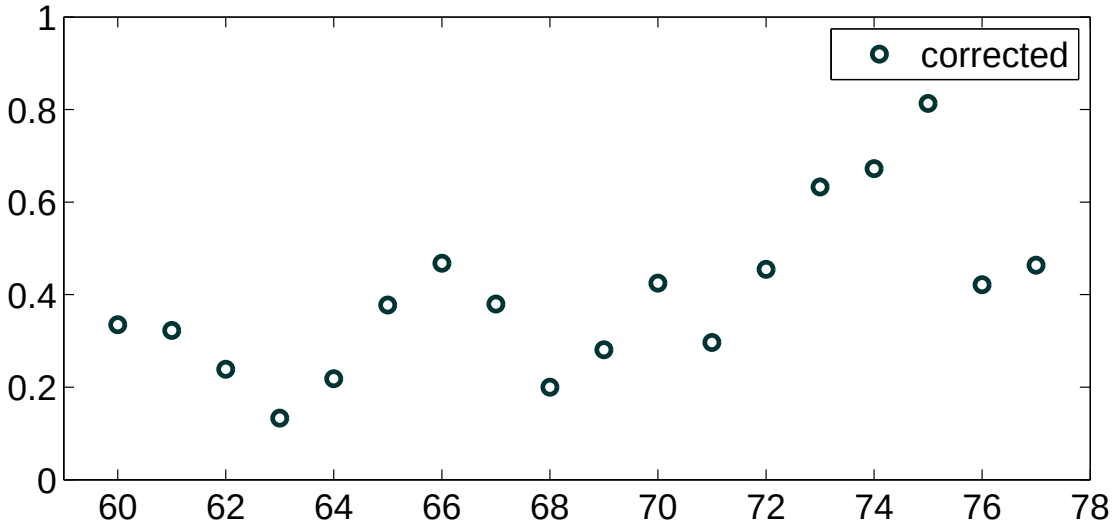

Figure 5.9: *The true reflection coefficients as a function of the receiver.*

sufficient for a preliminary guess of reflection coefficient and giving the right trend for the correction term, which is calculated for each receiver following the amplitude distribution given in section 4.5.4.

5.4.2 True Reflection Coefficient

The correction term for the geometrical spreading and the intrinsic attenuation is as well affected by the assumption of a isotropic homogeneous velocity model and thus a linear ray path. The consequential error here however should be less influential. The calculation of the correction terms follows the equations given in section 4.5.4.

For each event-receiver-pair, an apparent reflection coefficient is calculated from the waveform (only the L-component considered). Then, for each pair, the amplitude correction terms are determined and a true reflection coefficient is computed. The resulting reflection coefficients are plotted in Figure 5.9 as a function of the receiver.

The averaged true reflection coefficient at the imaged structure is:

$$< |R_{\mathrm{pp0}}| >= (0.31 \pm 0.04).$$

This value is surprisingly high compared to the result from the exemplary cluster of the Basel EGS. However, the reflector is very close to the receivers (and even intersecting the line of receivers) and illuminated under a quite high reflection angle so the value seems reasonable.

5.5 Discussion of the Reflection Coefficient

For the receivers at which we can compute the reflection coefficient, the reflection angle varies from 41 – 52 °. This means that the theoretical curve $R_{\mathrm{pp0}}(h_{eff})$ changes for each event-receiver-pair. The higher the receiver number, the smaller is the reflection angle. The trend in Figure 5.9 is slightly increasing, which means with increasing receiver number and decreasing reflection angle the PP reflection coefficient increases. This again means, that the effective width within the interval of 1 – 7 m or at an multiple of that. However, I can exclude higher multiples where the fault width is larger than the wavelength of the incident wave, because in this case the reflection coefficient should equal the reflection at a single solid-fluid interface.

Most of the estimated reflection coefficients intercept the graph of the theoretically predicted reflection coefficient as a function of fracture width and thus predict an effective fracture width, see Figure 5.10. However, this result is not unique as constructive interference of reflected waves is periodic and gives two solutions for a wavelength larger than the fault width. Additionally, a number of approximations bias the result. In principle all the reflection angles should be more similar as the reflection point changes with the receiver number but this is not considered here, as I use for a first estimate only a single reflection point. If I take the averaged number of the reflection coefficient, under the assumption, that the reflection angle stays constant with a moving reflection point, the effective fracture width could be restricted a little bit more.

In order to give a more safe prediction of effective fracture width, I would have to evaluate more events which contribute to the image of the reflector. In addition, I would have to use a more detailed velocity model which would also provide more accurate ray paths and more accurate emergent angles for the determination of the fault plane solutions. On the one hand, the fault plane solutions are still a critical point, since the target events are in the prolongation of the receiver array and thus give a bad coverage on the focal sphere. A good approach would be, to look if there are surface data of these events available. On the other hand, I have shown, that perturbations in the fault plane solution effect both the amplitudes toward the receiver and the amplitudes toward the reflector in the same way.

Another outcome of this chapter is that in the vicinity of the Buzzard Canyon Fault at depth fluids or similar high contrasts in elastic parameters must be present. A planar structure with a high impedance contrast must be present to cause such significant reflective signatures within the recorded microseismic data.

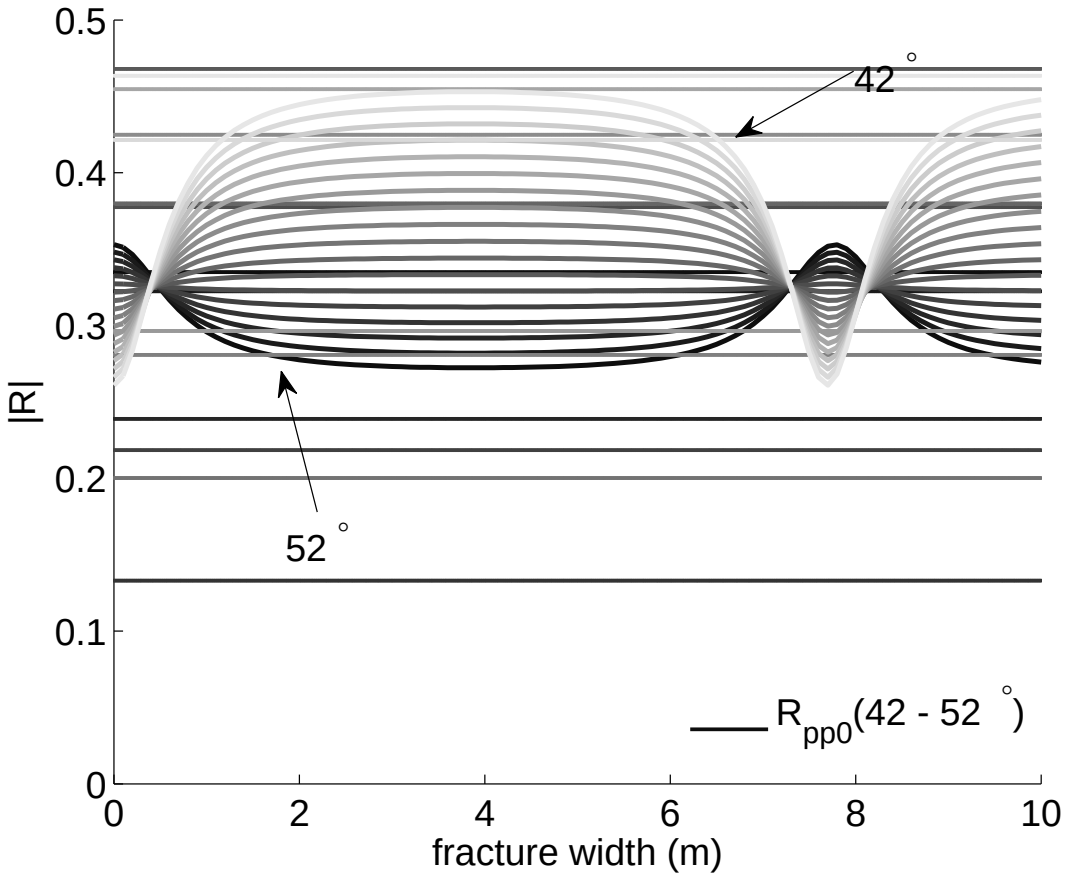

Figure 5.10: *The true reflection coefficients as a function of fracture width for different receivers. The higher the receiver number, the smaller is the reflection angle. Horizontal lines in corresponding color denote the estimated value of reflection coefficient.*

5.6 Summary: Application to the SAFOD

I have re-processed the waveform data of a single event recorded in the target area of the SAFOD. A PP reflection has been identified. In contrast to the Basel case study, the PP reflection of a single event is recorded on a receiver array. This means, that I evaluated each event-receiver-pair for its reflection coefficient. In the frame of that I determined the focal mechanism of the event, however, the result is poorly restrained and probably inaccurate. The restriction to an effective (natural) fracture width from a single event evaluation is not possible. However, the evaluation of further events, additional information of a surface array, or a more detailed velocity model and reflection point location could provide a reliable effective fracture width.

6. Anisotropic Case: Application to the Induced Seismicity at the Horn River Basin

In this chapter I aim to understand microseismic wavefields which are recorded in the Horn River Basin, British Columbia, Canada. This is an essential pre-requisite for extracting information on the subsurface using reflection coefficients. On this site hydraulic fracturing was deployed in order to increase the permeability for shale gas production and induced a number of microseismic events whose waveforms contain plenty of information on the reservoir.

In Germany, the "Energiewende" demands halving the energy consumption and, at the same time, the expansion of renewable energies (BMWi, 2014), as I mentioned before in the introduction to Chapter 4. However, as sketched in Figure 6.1, in 2014 only 11 % of the primary energy (amount of energy that is required to support the national economy) were produced using renewable energy sources. The transition to low carbon energy production will take decades. Until then, natural gas is regarded as a "bridge" energy source because of its low CO_2 emission. In Germany, conventional gas resources were estimated to be $\sim\ 88 \cdot 10^9\ m^3$, whereas the technically recoverable resources of shale gas, the unconventional resources, were estimated from $0.7 \cdot 10^{12}\ m^3$ up to $2.3 \cdot 10^{12}\ m^3$ to a multiple of the conventional resources (BGR, 2015).

Even though only parts of the available unconventional gas resources can be recovered economically, their potential exploitation will play a role in the discussion of the future energy supply.

In Northern America, unconventional gas resources are already commercially successful exploited. The Horn River Formation is a significant shale gas reservoir. The data to which I refer in this chapter were recorded there. For the characterization of the reservoir a description of subsurface structures and imaging of hydraulic fractures is a goal. The recorded data exhibit quite complex wavefields. In order to extract the corresponding reflection coefficients from the Horn River Basin data set for further evaluation in terms of reservoir properties it is crucial to understand the recorded wavefield entirely.

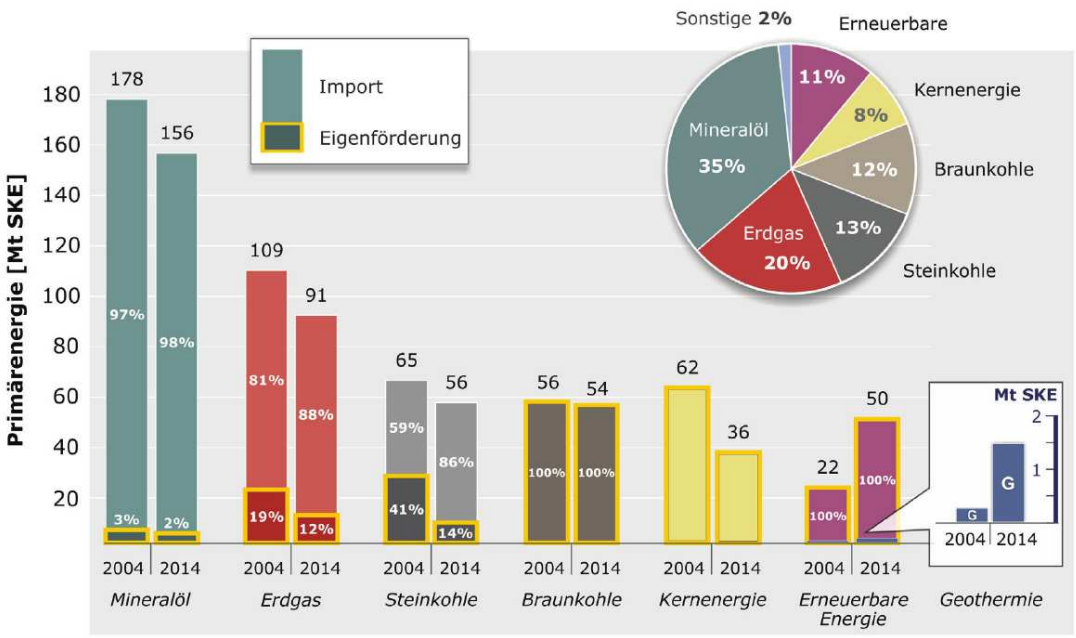

Figure 6.1: *Illustrated is the German import of resources for primary energy production in 2004 and 2014. On the top left of the figure the mixture of resources is sketched. Figure taken from BGR (2015).*

In the following I will numerically investigate the multiple wavefront arrivals from microseismic events in anisotropic heterogeneous media using numerical modeling based on the Finite Difference algorithm described in Chapter 3. The influence of anisotropy on the wave propagation can be significant. Shear wave splitting causes additional strong signals in the recorded wavefield and interfaces within a heterogeneous velocity distribution can cause the occurrence of multiple wavefront arrivals. Consequently it is very difficult to identify reflections from hydraulic fractures within such a wavefield record.

In the end of the chapter I will not be able to identify and image reflections from within the recorded wavefield because the provided velocity model is not sufficient for understanding the waveforms. However, as a pre-study for the interpretation of the wavefield, exemplary different settings are given and discussed:

- A homogeneous anisotropic velocity layer is modeled
- The influence of interfaces from a two-layer anisotropic velocity model is examined as the provided velocity model is a block model with sharp velocity contrasts at the interfaces
- A smoothed anisotropic velocity model derived from borehole logs is implemented

- An updated anisotropic velocity model derived from borehole logs is implemented

First, I model the wavefield in a homogeneous anisotropic volume. I will see, that already in this simple case with the anisotropic parameters given by the microseismic data, the wavefield shows significant signatures caused by the shear wave splitting. Then I investigate the influence of interfaces: Conversions and reflections are present in the recorded wavefield and are not to be mixed with reflections at hydraulic fractures. Finally I model the wave propagation of a microseismic event with the complex velocity model extracted from the borehole log and compare the travel times to numerical solutions derived using a ray tracing program. The numerical results will be compared to the real data recordings of induced microseismic events within this anisotropic and heterogeneous environment.

6.1 Introduction to the Data Set

The considered data set consists of microseismic events that were induced during a hydraulic fracturing treatment in the Horn River Basin, British Columbia, Canada. Three fracturing stages were recorded at two receiver arrays consisting of 10 and 21 geophones, respectively. At each stage a set of microseismic events was induced (Figure 6.2) (e.g. Hummel and Shapiro (2013)). The idea is that in each stage hydraulic fractures are either generated or pre-existing fractures are re-opened. So waves from an event of a later stage are potentially reflected at these fractures and the respective signature is recorded in the microseismic data (Figure 6.3).

6.2 Modeling Wave Propagation in Anisotropic Media

A crucial point in order to extract amplitudes from potential reflections is to understand the recorded wavefield. Often when it comes to real data, the subsurface is not homogeneous or isotropic anymore. Depending on the medium and on the scale which we are looking at, inhomogeneities and anisotropy can start to play an essential role.

The Horn River Basin data set I chose to examine includes the above mentioned complexities. In a first approximation the subsurface is horizontally layered, each layer exhibiting different elastic properties. In the area of interest, where most of the microseismic events are triggered, anisotropy has a large impact on the wave propagation. An example of anisotropic parameters within the study area is given in Table 6.1. Large Thomsen parameters ϵ, γ, and δ, predict a huge shear wave splitting. The low velocity zone (labeled layer 8) may cause

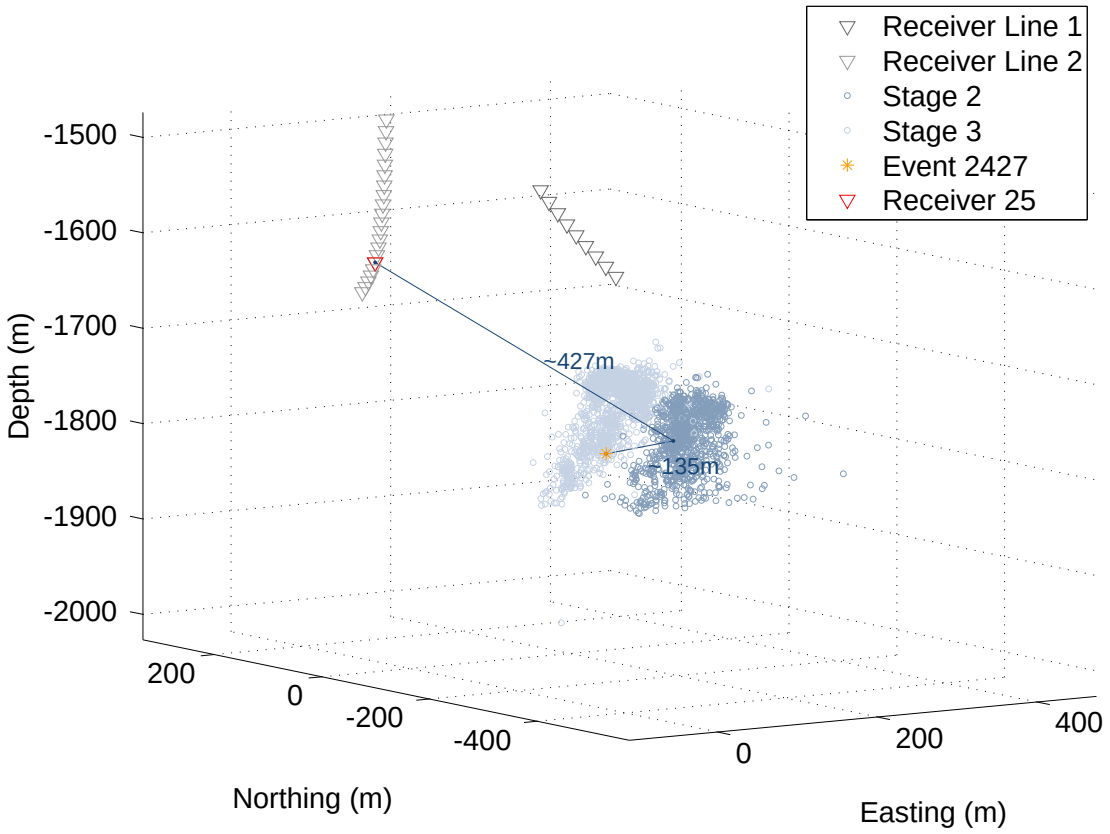

Figure 6.2: *Schematic setup of the hydraulic fracturing experiment in the Horn River Basin and the induced seismicity. Events from the second and third stage are plotted (blue points). The events were recorded at two arrays consisting of 10 and 21 geophones (gray triangles), respectively. Wavefields from events off the third stage are potentially reflected at fractures that were opened during the second stage. A possible ray path is sketched for one specific event (orange star).*

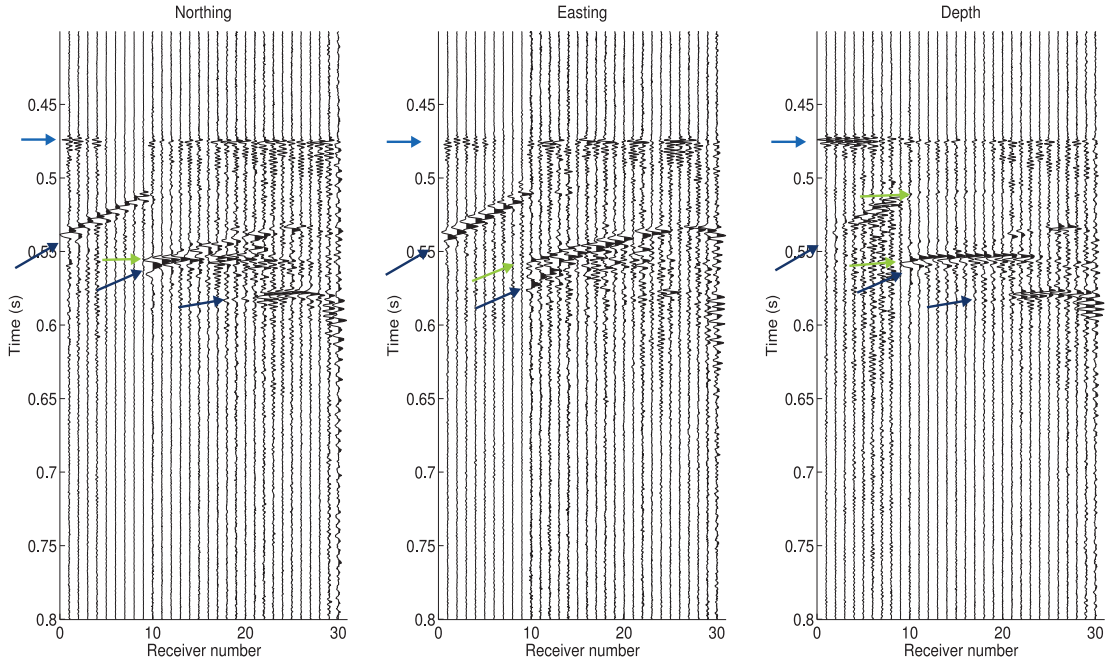

Figure 6.3: *A representative seismogram from an event recorded during the third fracturing stage. All three components are plotted. The data are P wave aligned as indicated by light blue arrows. The different receiver arrays can be distinguished. A huge shear wave splitting is present. Additional strong signals are recorded. They are potential reflections from hydraulic fractures or as shown in this thesis are reflections or conversions due to a heterogeneous velocity distribution and reflections and conversions at interfaces. It is hard to distinguish between reflections at hydraulic fractures and reflections / conversions or splitted shear waves due to the velocity model (all indicated by green and dark blue arrows).*

# Layer	Vp (m/s)	Vs (m/s)	ε	δ	γ
3	3525	1725	0.2	0.3	0.4
4	3650	1800	0.2	0.3	0.4
5	3800	1925	0.2	0.3	0.75
6	4000	2350	0.2	0.3	0.55
7	4150	2550	0.12	0.15	0.15
8	3800	2325	0.15	0.15	0.2
9	4700	2850	0.1	0.1	0.1

Table 6.1: *Elastic parameters from the study area.*

deviations from the expected wavefield. Between the different layers, relatively large contrasts may also cause reflections of the wavefield and therefore can make the interpretation of the recorded wavefield more complicated.
In order to identify each signature within the recorded data to later extract reflections from potential hydraulic fractures, I need to understand the influence of layering and anisotropy. In the following I will try to cover both these effects on the wave propagation.

To recall, the rotated staggered grid (RSG) finite difference (FD) algorithm suggested by Saenger et al. (2000) serves our purposes. The accuracy of this algorithm for thin fractures has been shown before by Krüger et al. (2005) and is a pre-requisite for further studies when besides the above mentioned effects, hydraulic fractures will be included to the model. Saenger and Bohlen (2004) have shown the applicability of this FD scheme to model wave propagation in anisotropic media and VTI media in particular.

6.2.1 Stiffness Tensor for a VTI Medium

Seismic anisotropy describes the angle-dependency of the seismic wave velocity. This angle dependency can be due to the fabrics, which means grain scale heterogeneities (Thomsen et al., 2002) such as aligned crystals or layers of a medium, or the anisotropy can be induced by dry or fluid-filled fractures, the so called crack induced anisotropy.
The anisotropy can be described using the stiffness tensor. This stiffness tensor is the elasticity tensor which is simplified due to the symmetry of stress and strain according to the Voigt scheme. In a general, triclinic, case there are 21 independent entries in the stiffness matrix. If there is polar symmetry, which means a vertical or horizontal symmetry axis, the unknown parameters reduce to 5 elements:

$$c_{33} = \rho v_{\mathrm{p0}}^2$$

$$c_{44} = \rho v_{\mathrm{s0}}^2$$

$$c_{11} = 2\varepsilon c_{33} + c_{33}$$

$$c_{66} = 2\gamma c_{44} + c_{44}$$
$$c_{13} = \sqrt{2\delta c_{33}(c_{33} - c_{44}) + (c_{33} - c_{44})^2} - c_{44}$$

where $\varepsilon, \gamma, \text{and } \delta$ are the Thomsen parameters, and ρ is the density of the rock. v_{p0} and v_{s0} are the P and S wave velocities along the symmetry axis. The Thomsen parameters are a dimensionless measure of the degree of anisotropy and reduce to zero in the case of an isotropic medium. A rock with a vertical symmetry axis is commonly referred to as VTI (vertical transverse isotropy) medium, whereas in a HTI (horizontal transverse isotropy) the symmetry axis is in the horizontal. The density normalized stiffness matrix components can be included to the deployed numerical modeling algorithm.

6.2.2 The Modeling Setup

I apply damping boundary conditions since they minimize the boundary reflections and allow a study of the wavefield with hardly any boundary reflections. The dispersion criterion is chosen in such a way, that for wave propagation within the most dominant layer (in terms of thickness) the simulations run without any dispersion and fulfills the stability criterion. On the contrary, in the displayed examples we can observe slight dispersion. However, to ensure the comparability of models with different medium parameters, the grid spacing and time update interval are kept constant throughout the experiments. Moreover, a slight dispersion does not influence the main focus of this case study and hence we will neglect this fact.

The modeling volume is chosen in a way, that for later modeling of the real data it potentially contains microseismic events from all three stages and partly one receiver array. The general model volume setup is shown in Figure 6.4. The depth is realized by 600 grid points (300 m) and the x-axis by 1500 grid points (750 m). Investigating a VTI medium, 300 grid points in y-direction (150 m) are sufficient. A vertical 8 receiver array (blue triangles) with a slight inclination is realized. In the opposite corner of the model, a source (red star) is deployed.

6.2.3 Homogeneous Anisotropic Layer

In order to study the influence of anisotropy and compare results to the real data, medium properties of the study area are adapted. For the example which I show here, properties of one of the upper layers are taken and presented in Table 6.2.
In Figure 6.5 and 6.6 depth slices of the complete wavefield after different time steps are displayed. The depth slice is located at the same y-coordinate as the source. A for microseismic events typical double couple mechanism (see Table 6.2) serves as a source. The anisotropic wave propagation is visualized using hot colors for high amplitudes and cold colors for negative amplitudes.

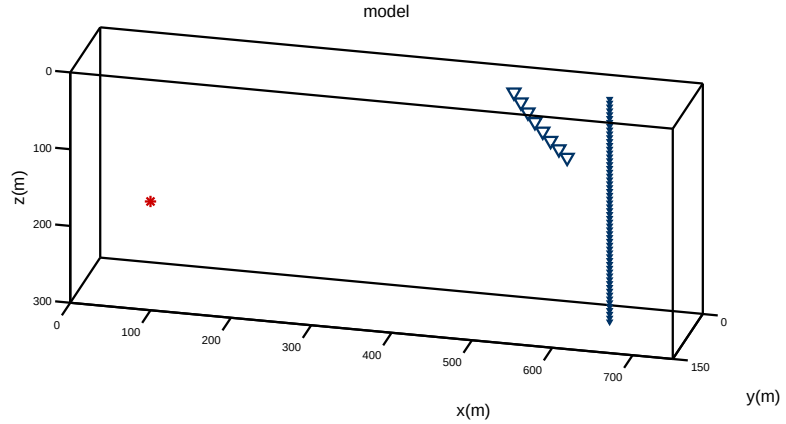

Figure 6.4: *The modeling volume. The inclined 8 receiver array (blue triangles) is realized and a vertical line of receivers is implemented. In the opposite corner of the model, a source (red star) is deployed.*

Medium properties		Source properties
P wave velocity v_p	3650 m/s	strike ϕ 73°
S wave velocity v_s	1800 m/s	dip δ 90°
Thomsen parameters		rake λ 0°
ε	0.2	
γ	0.4	
δ	0.3	
Model parameters		
Grid spacing dh	0.5 m	
Time update interval dt	0.067 ms	

Table 6.2: *Modeling parameters for the FD numerical modeling.*

Within the wavefield a relatively weak P wave and stronger S_1 and S_2 wave can be identified. The effect caused by the anisotropy of the medium can clearly be seen, not only in the (strong) shear wave splitting but also in the elliptical propagation of the wavefront (for more background on seismic anisotropy, c.f. Grechka (2009)).

The different components of the wavefield recorded at the array are plotted in Figure 6.7. Here, the clear P wave arrival and the fast and slow S wave can be distinguished. In the coda of both S waves the above mentioned dispersion is visible. In addition, boundary reflections cause a slight noise level but no obvious sign of a triplication is visible.

6.2.4 Influence of Interfaces

The realistic velocity model which was provided by the operator of the experiment, is a block model consisting of several homogeneous anisotropic layers (Table 6.1). The borehole log contains several sharp contrasts in elastic parameters, so that in this chapter we study the influence of interface reflections and conversions.

Again, the cuboid modeling volume as in Figure 6.4 is deployed. In Figure 6.8 the depth view with the block velocity model and a map view illustrate the modeling setup. I now investigate different interfaces within separate simulations. For each simulation one interface at the corresponding depth is realized. The complete upper half space has the properties of the upper adjacent layer whilst the complete lower modeling volume has the properties of the lower adjacent layer. The elastic properties of the two simulations discussed in this section are listed in Table 6.3.

Interface depth	Elastic properties above the interface		Elastic properties below the interface	
116 m	v_p = 3800 m/s	ε = 0.2	v_p = 4000 m/s	ε = 0.2
	v_s = 1925 m/s	γ = 0.75	v_s = 2350 m/s	γ = 0.55
		δ = 0.3		δ = 0.3
291 m	v_p = 3800 m/s	ε = 0.15	v_p = 4700 m/s	ε = 0.1
	v_s = 2325 m/s	γ = 0.2	v_s = 2850 m/s	γ = 0.1
		δ = 0.15		δ = 0.1

Table 6.3: *The elastic properties of the presented two simulations investigating interface effects are listed.*

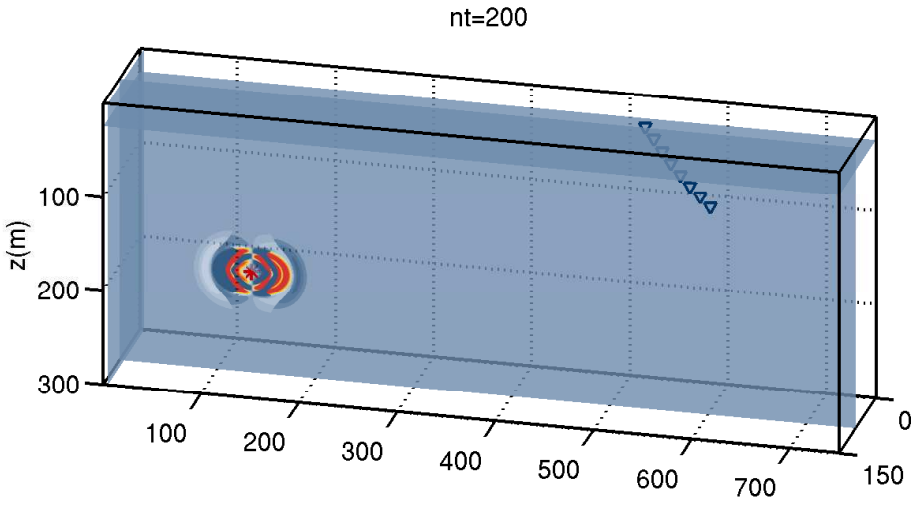

(a) t = 13.3 ms

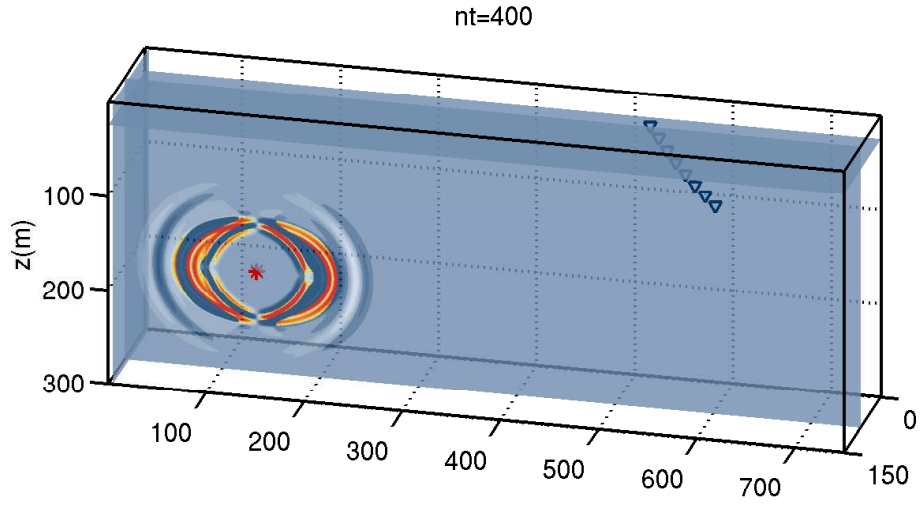

(b) t = 26.6 ms

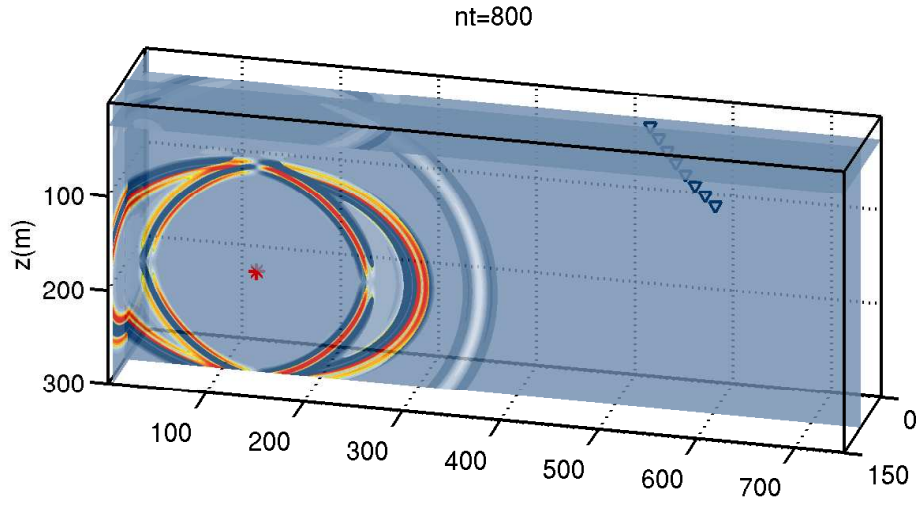

(c) t = 53.3 ms

Figure 6.5: *Snapshots of the modeled wave propagation in an homogeneous and anisotropic medium.*

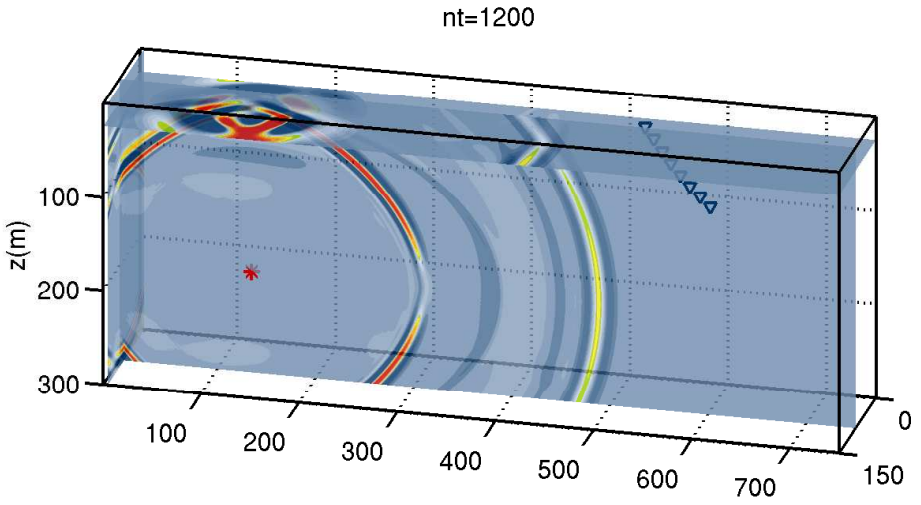

(a) t = 79.8 ms

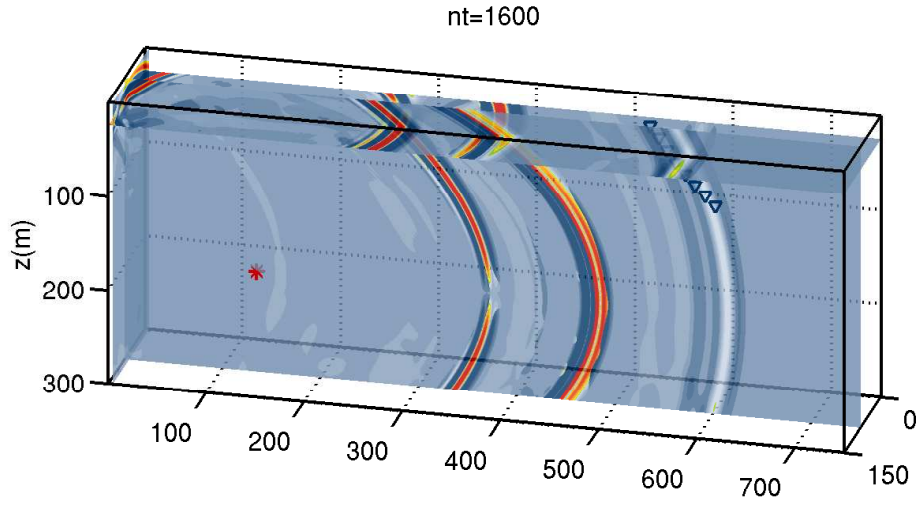

(b) t = 106.6 ms

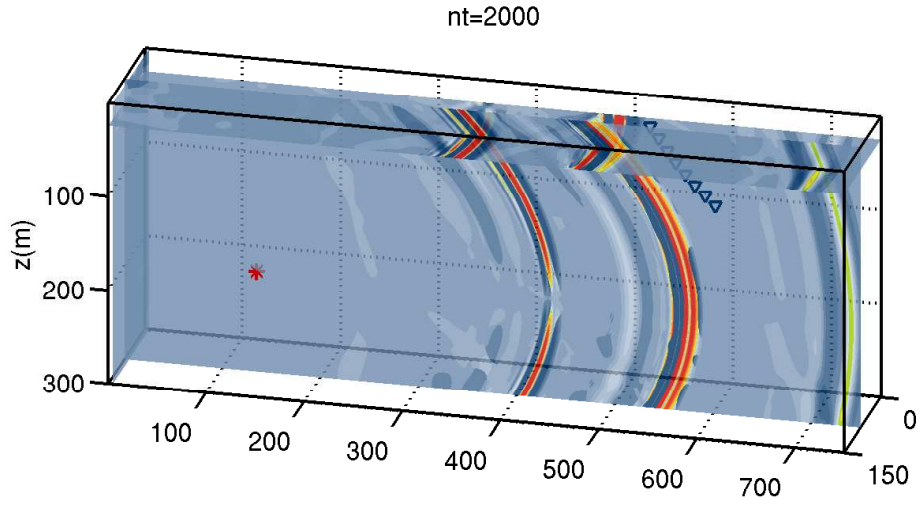

(c) t = 133.3 ms

Figure 6.6: *Snapshots of the modeled wave propagation in an homogeneous and anisotropic medium.*

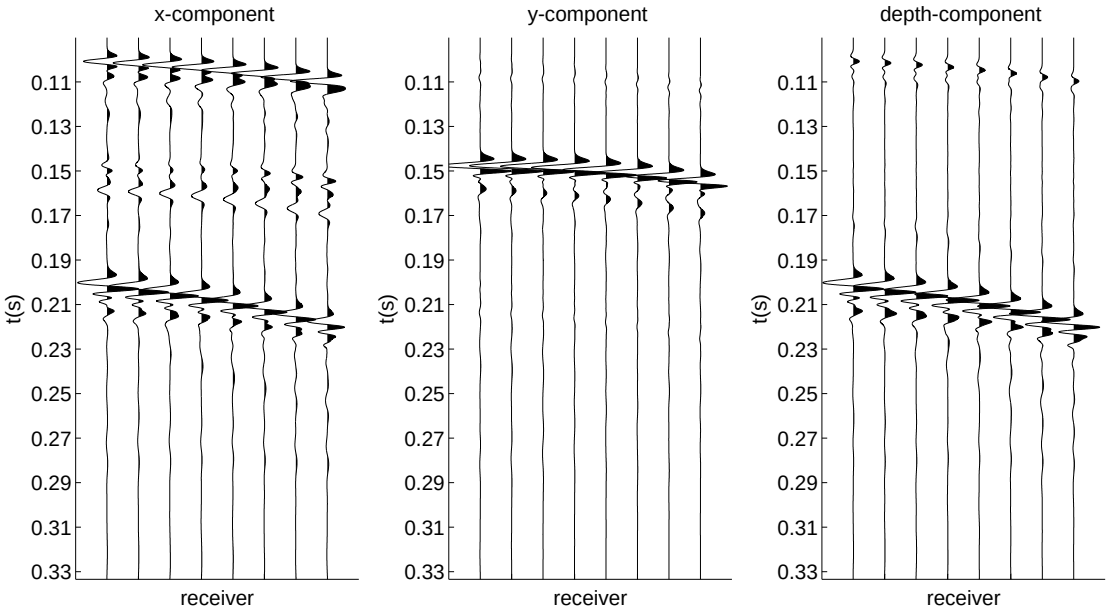

Figure 6.7: *All three components recorded at the receiver array.*

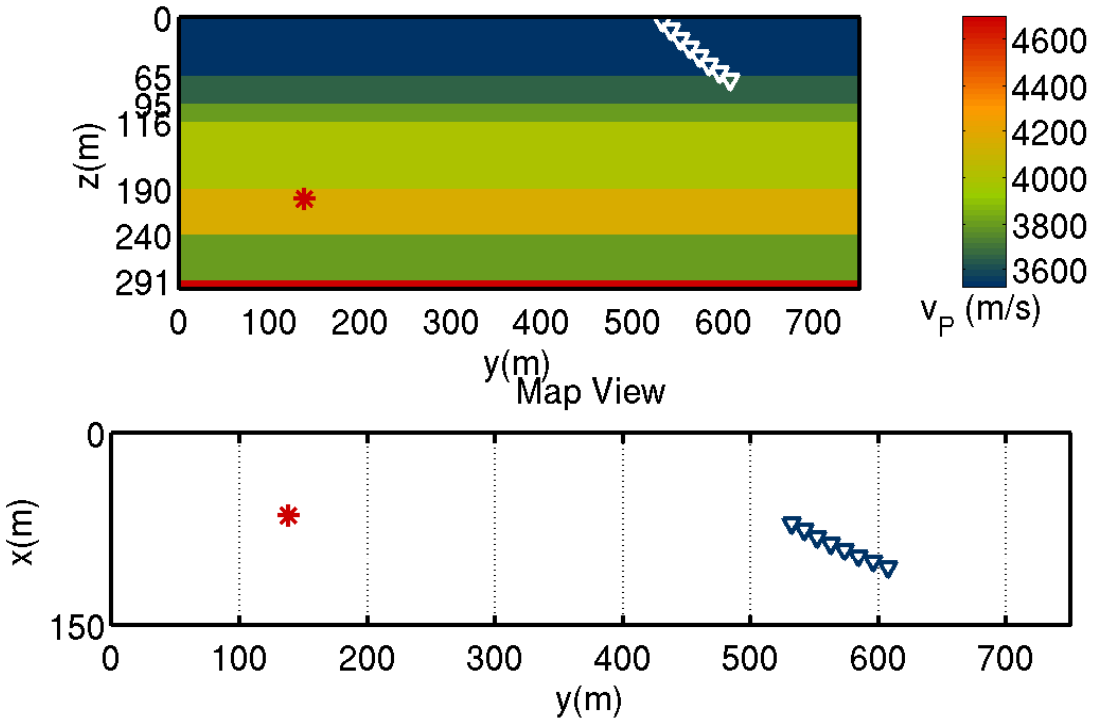

Figure 6.8: *In a depth view the block velocity model is illustrated. The map view visualizes the spatial distribution of source and receivers.*

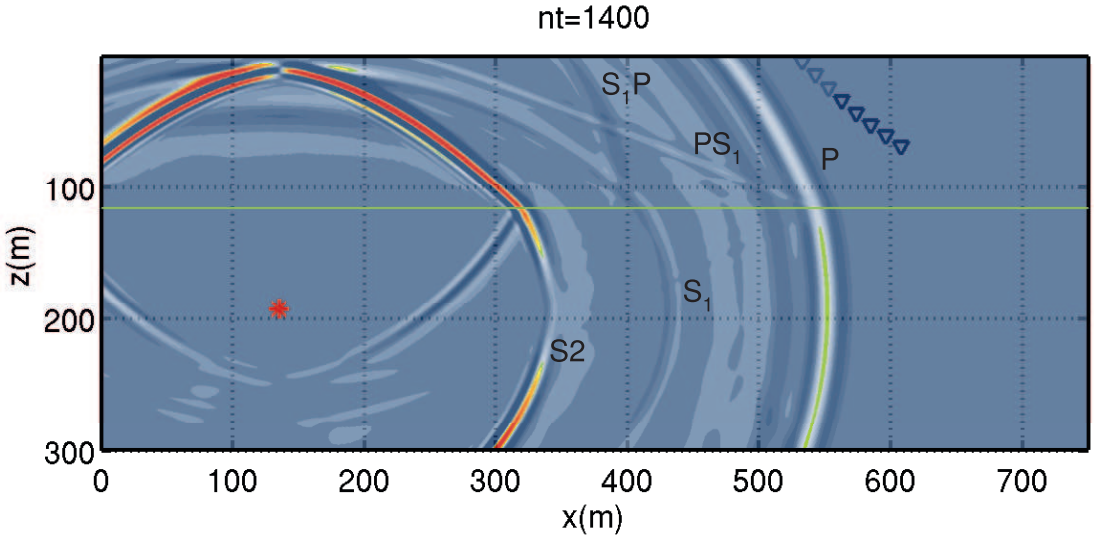

(a) A snapshot of the complete wavefield after 93 ms. The interface is indicated by a horizontal green line. The different wave types are indicated.

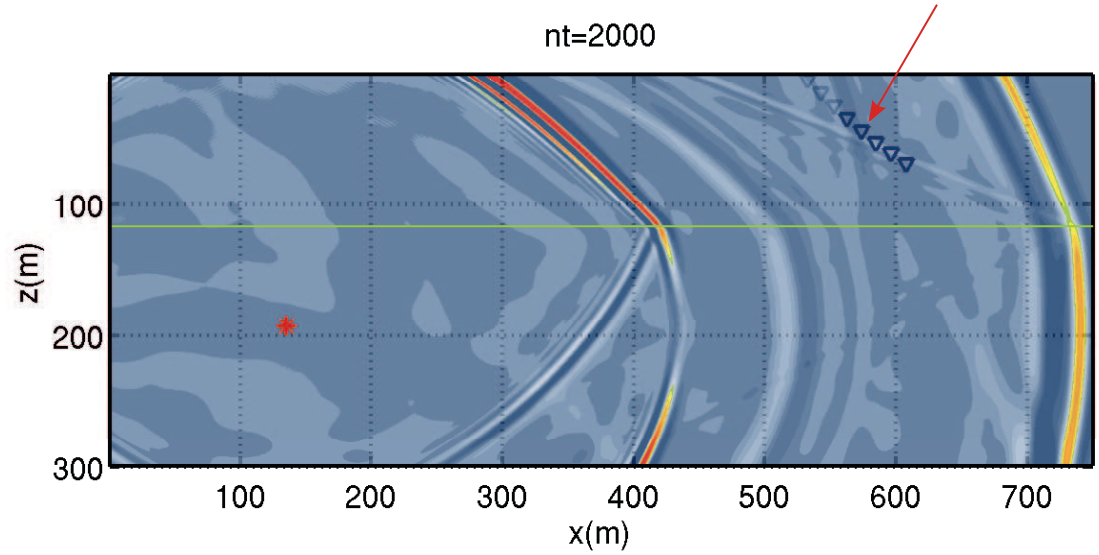

(b) A snapshot of the complete wavefield after 130 ms. The interface is indicated by a horizontal green line. The red arrow indicates the intersection point between the converted PS_1 and S_1P wavefront which we can identify in the recorded seismogram in Figure 6.10, indicated with red arrows.

Figure 6.9: *Wave propagation in a two-layer anisotropic medium with a significant influence of the interface.*

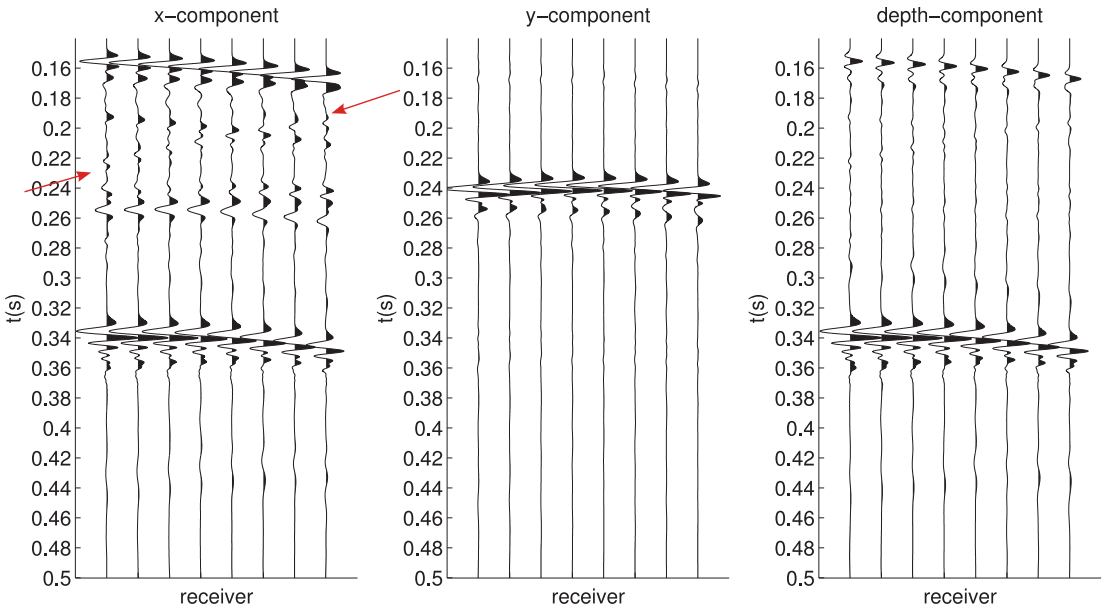

Figure 6.10: *The recorded wavefield. The source is in the lower layer whilst the receivers are all within the upper layer. All three components are plotted. The first signal is the direct P wave, followed by the S_1-P wave, that is intersected by the P-S_1 wave and has an opposite slope, indicated by red arrows. The next signal is the S_1 wave, followed by the S_2 wave.*

The snapshots and the recorded seismograms (Figure 6.10) for this simulation show that the influence of the interface between source and receivers is significant. Converted waves show non-negligible signatures in the wavefield.

In the second example, I investigate the influence of the bottom interface. Below source and receivers, at 291 m depth, a high velocity layer marks the bottom of the stimulated volume. However, this large velocity contrast most likely causes signatures within the recorded wavefield. In Figure 6.11(b) the layers are visualized once more. The source and receiver positions in this figure are not their true locations, only their depth is their true depth in order to illustrate their location with respect to different interfaces. In Figure 6.11(a), next to the signal of the direct P , S_1 , and S_2 wave, diverse reflections from the interface more or less interfere with the S_1 signal. A similar slope makes them hard to distinguish. If the source is closer to the interface, the signals will be indistinguishable.

To conclude this section, I can say that velocity contrasts can cause significant reflections within the recorded wavefield. In order to not confuse them with reflections from hydraulic fractures, it is crucial to identify reflections at interfaces as such.

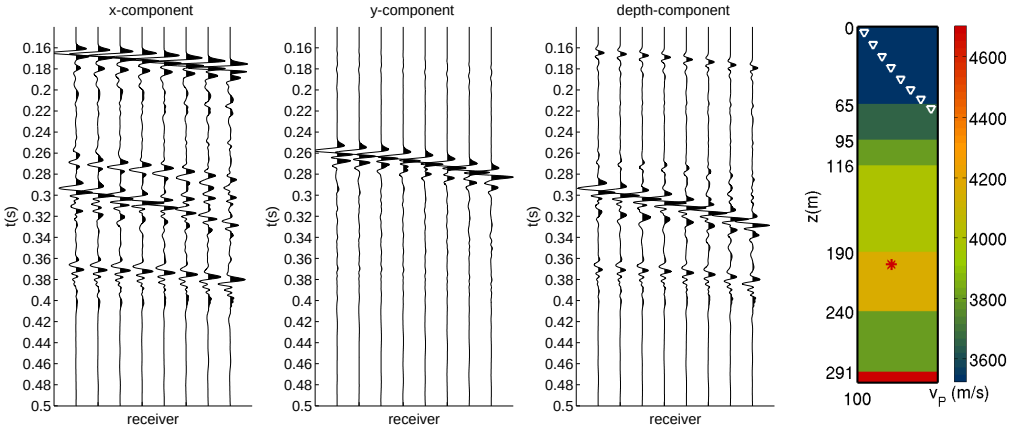

(a) The seismograms for a wavefield containing reflections from the bottom layer.

(b) The layered velocity model.

Figure 6.11: *The influence of the interface to the basement below the stimulated volume is shown here. In this simulation, we consider the interface at 291 m depth, below events and receivers.*

6.3 Complex Modeling Setup

A next step in the modeling path is now to include the real velocity model and compare the synthetic results with real data. For this, an event from the third stage and within the modeling volume was selected (Figure 6.12).

The selected event (Figure 6.12) has a magnitude of $M = -0.73$ and was induced during the third hydraulic fracturing stage. The recorded seismograms including picked P and S arrival times are plotted in Figure 6.13.

The velocity model (Figure 6.12(d)) was derived from borehole logs. The anisotropic elastic parameters were smoothed using Backus averaging over a 35 m base. For detailed information see Reshetnikov (2013). In a first modeling step, an explosion source is deployed. The snapshots of the complete wavefield at different times in Figure 6.14 and Figure 6.15 show that the most prominent reflection is due to the low velocity zone right below the event. In the case of an explosion source, a quite strong P wave arrival and a significant shear wave splitting are expected and both can be observed in the snapshots of the complete wavefield. The amplitude of the fast S wave is, in the case of an explosion source, relatively weak compared to the P wave. However, in the case of a double couple mechanism this might change though. The dispersion that we see in time step 3100 (Figure 6.15(b)) is due to the low velocity and has been discussed in a previous subsection (6.2.3).

The recorded seismograms at the receiver array are plotted component-wise in Figure 6.16. They are compared to the picked P and S wave arrival times from

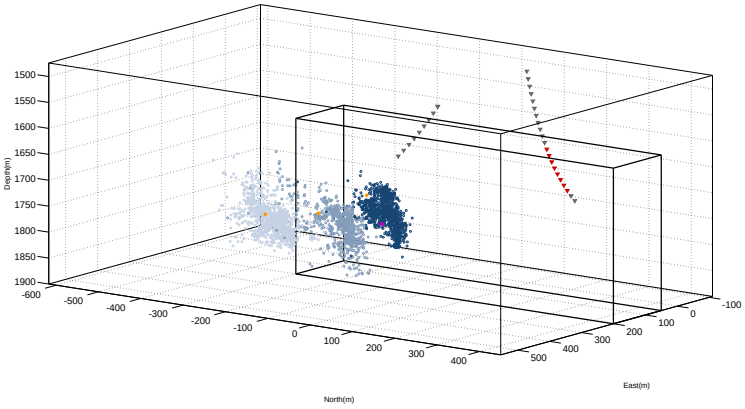

(a) A 3-D view of the induced seismicity including the modeling volume.

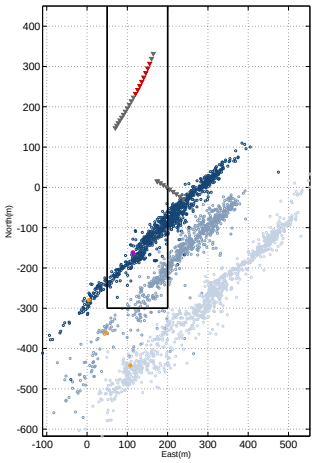

(b) A map view.

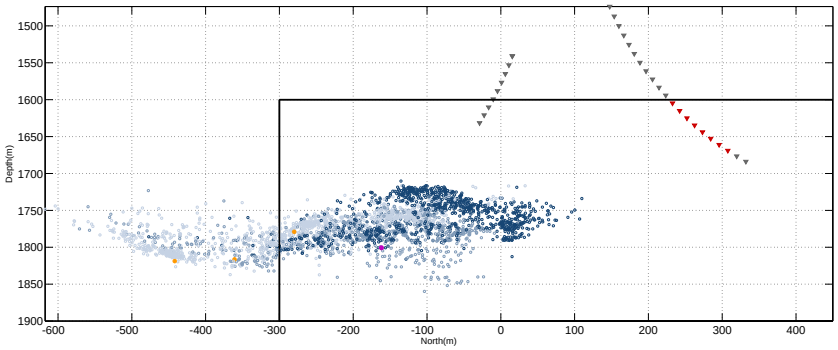

(c) A depth view of the induced seismicity including the modeling volume.

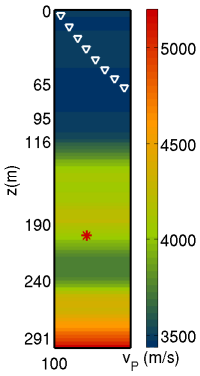

(d) The P wave velocity.

Figure 6.12: *Two receiver arrays record the events from 3 different stages. Stage 1 events are colored by light blue, stage 3 events are in dark blue and closest to both arrays. Perforation shots for each stage are marked by orange dots. The modeling volume is illustrated by the cuboid and chosen such, that both events from third and second stage and one receiver array (red receivers) can be included in the modeling. The chosen event is marked by a magenta point. The elastic parameters are extracted from the borehole log and smoothed using Backus averaging.*

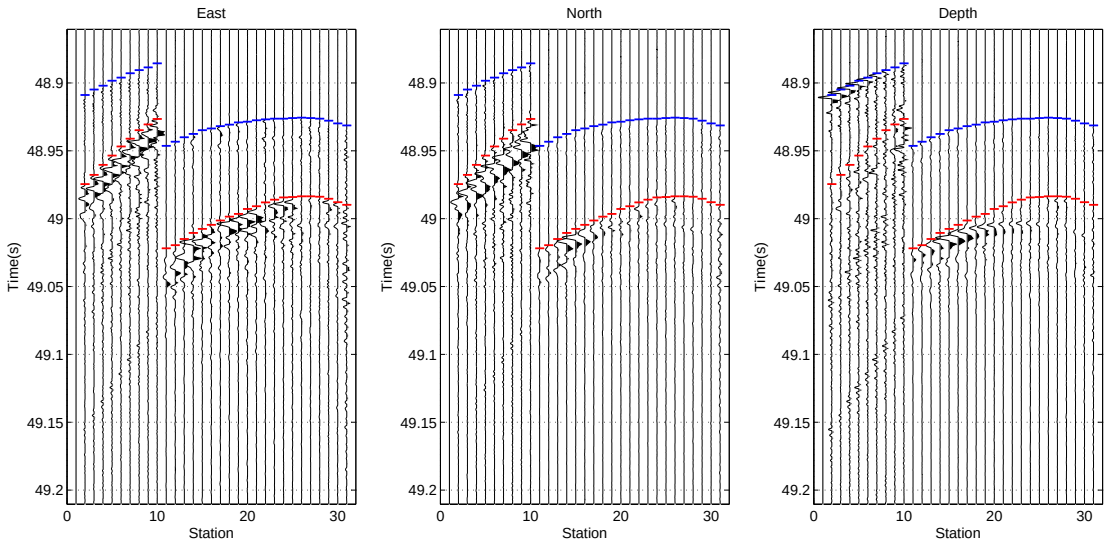

(a) East component. (b) North component. (c) Vertical component.

Figure 6.13: *The recorded seismogram of a $M = -0.73$ event are displayed. Blue line denotes the (provided) picked P wave arrival, the red line denotes the S wave arrival.*

the real data and to the theoretical arrival times derived using a Ray Tracer (Reshetnikov, 2013). Figure 6.17 shows a superposition of the wavefronts calculated using this Ray Tracer and the modeled wavefield. The Ray Tracer's input are the same elastic parameters as used in the FD modeling and both results are in a good agreement. Compared to the real data picks, a quite high deviation is obvious. I conclude, that the deviation results from an incorrect velocity model, since both independent modeling methods are in agreement. The vertical line of receivers as shown in Figure 6.14 and 6.4 is used for a further evaluation of the Ray Tracer in the report of Reshetnikov (2013).

6.4 Discussion of the Result

The identification of reflections from hydraulic fractures in data from a layered, anisotropic subsurface is, as expected, quite challenging. Inhomogeneities, such as interfaces as they are caused by large velocity gradients, in the velocities alone may cause significant signatures in the recorded wavefield. In addition, anisotropy and especially anisotropy in combination with interfaces and therefore various reflected and converted waves increase the number of significant wave types within the recorded wavefield.

We are able to take changes in anisotropic and other elastic parameters into account and model the wave propagation of an arbitrary source which can be represented by a moment tensor. The synthetic wavefields serve as support for

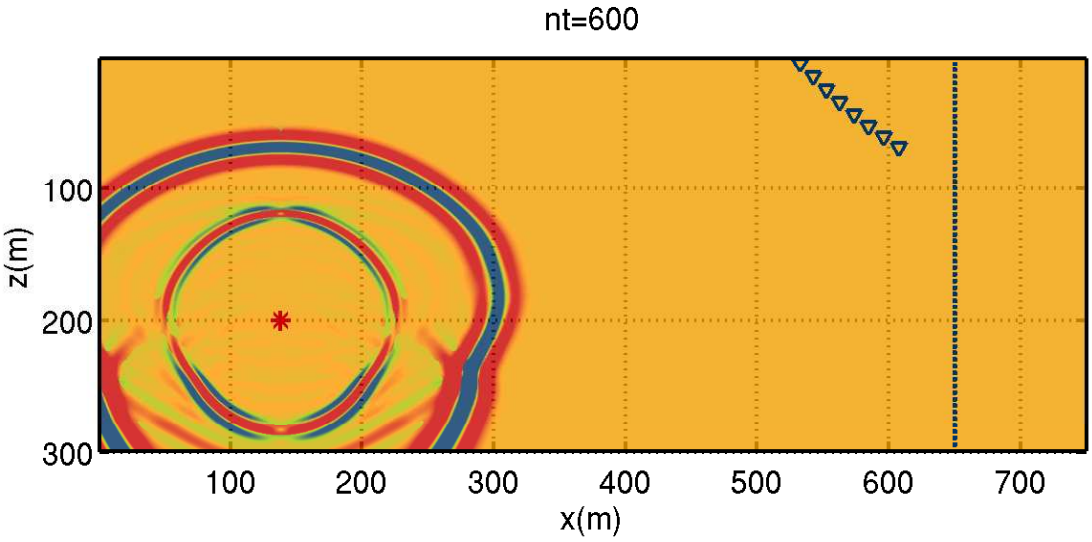

(a) The complete wavefield after 40 ms.

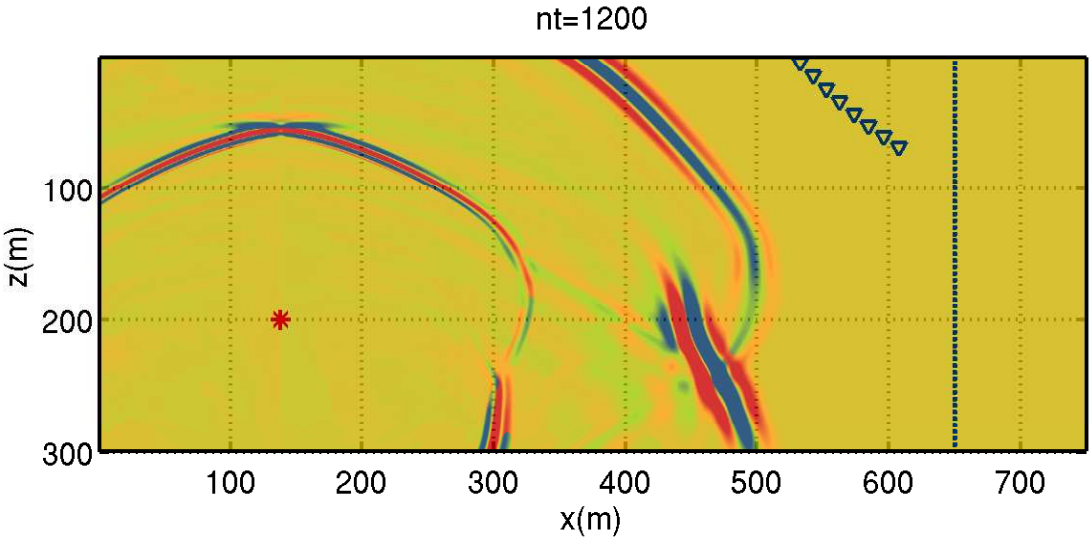

(b) The complete wavefield after 80 ms.

Figure 6.14: *The complete wavefield of a real data event (modeled by an explosion source) in a depth view at different times. The second receiver array as deployed in the induced seismicity experiment is partly realized. Additionally a vertical line of receivers is included to the modeling in order to compare travel times from FD modeling with a ray tracing algorithm.*

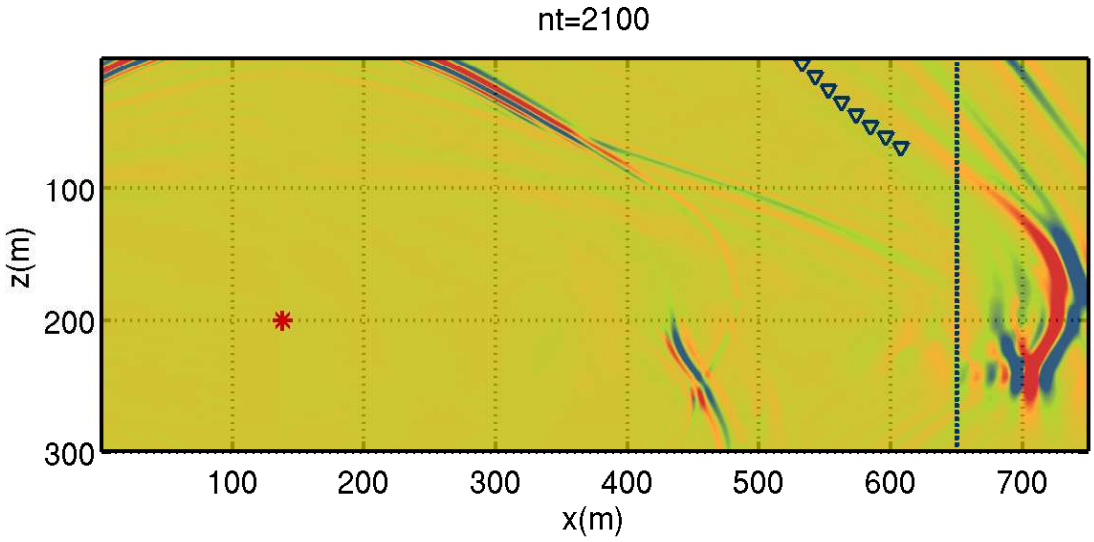

(a) The complete wavefield after 140 ms.

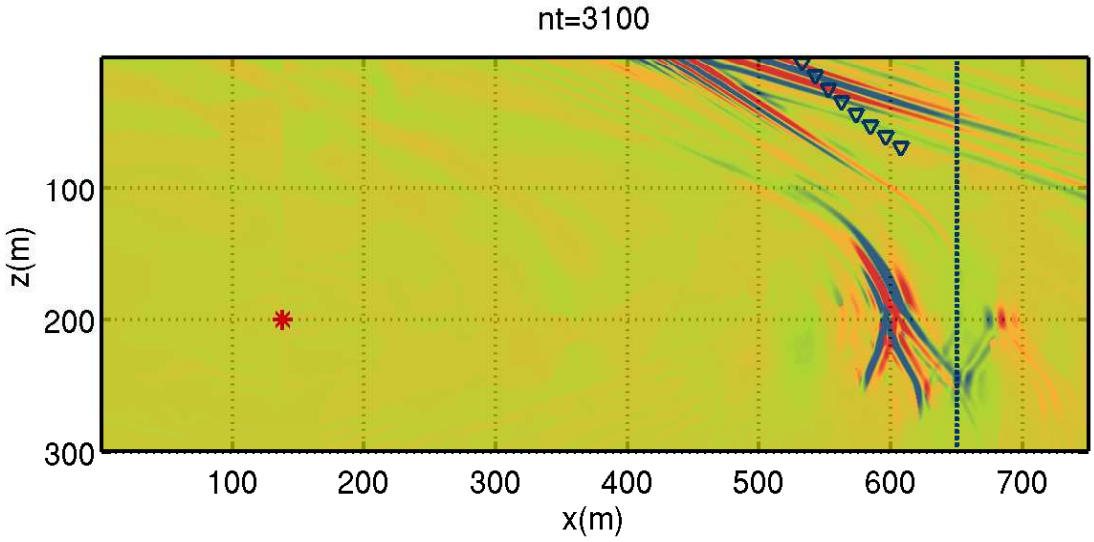

(b) The complete wavefield after 207 ms.

Figure 6.15: *The complete wavefield of a real data event (modeled by an explosion source) in a depth view at different times. The second receiver array as deployed in the induced seismicity experiment is partly realized. Additionally a vertical line of receivers is included to the modeling in order to compare travel times from FD modeling with a ray tracing algorithm.*

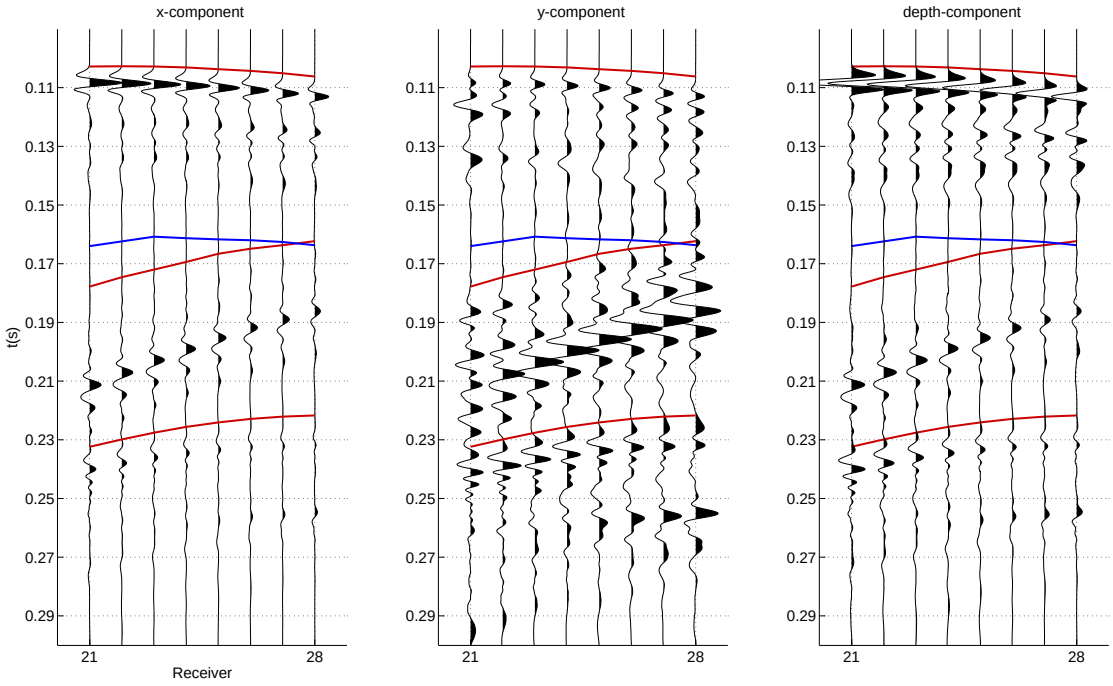

Figure 6.16: *The three components of the seismograms as they are recorded in the FD modeling experiment at the receiver array. The red lines are P , S_1 and S_2 wave arrival times derived from ray tracing, the blue line denotes the picked S wave arrival.*

the interpretation of the real wavefields. Once, an appropriate velocity model is derived, reflections within the data can be identified. This reflections can be imaged and give a map of reflectors. The effective properties of the mapped reflectors could be extracted from the recorded microseismic waveforms.

6.5 Summary and Outlook: Application to the HRB

In this chapter I have analyzed microseismic waveform data from a shale reservoir in the Horn River Basin, Canada. This shaly rock is intrinsically highly anisotropic due to its fabrics, which means the alignment and lamination of minerals (c.f. Yu and Shapiro (2015)). Using a FD algorithm I have investigated the influence of anisotropy on the wave propagation within this HRB reservoir.

First, I have analyzed the influence of anisotropy in a homogeneous anisotropic rock using the Thomsen parameters as given by the data provider. The acquisition geometry was adapted from the reservoir, the source position is given by the location of one exemplary event and a representative focal mechanism is implemented. Besides the applicability of the deployed FD

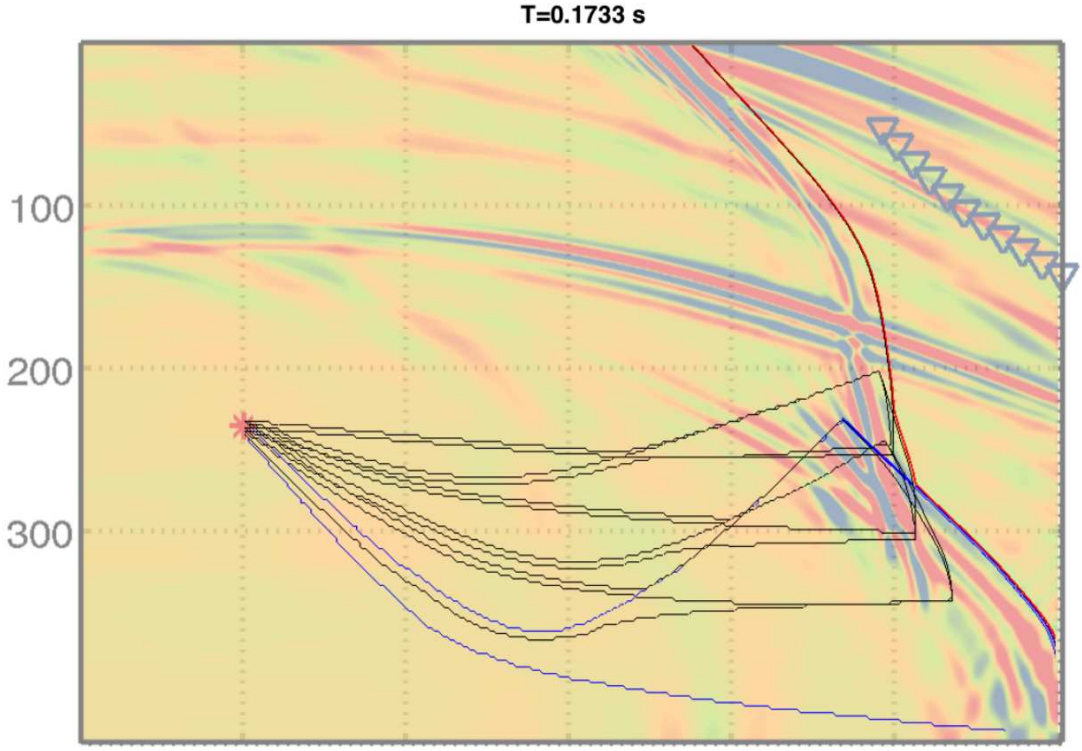

Figure 6.17: *Comparison to ray tracing results, superposition of S wavefronts from ray tracing by A. Reshetnikov.*

algorithm, the modeling results show, that a significant shear wave splitting is to expect within the real data and the signal that was identified as a reflection from a first visual inspection might be the slow shear wave.

In a next step I have investigated the influence of the interfaces of the different layers. High velocity contrasts lead to conversion and reflection of waves at the boundaries. I have modeled several two-layer realizations implementing the properties from the given model. Already for the two layer case the modeled wavefield becomes quite complex: we have converted, converted and reflected, and reflected waves. This is a challenge in the interpretation of the wavefield. Additionally there are amplitude effects of the source, which can influence the recorded signal strength.

Taken from the borehole log an improved and smoothed velocity model was derived by Reshetnikov and Shapiro (2015). For this velocity model the simulations were repeated using a different source location and a double couple fault mechanism. The resulting wavefront were compared to ray tracing results and multipath shear wave arrivals, as predicted by the ray tracer, were confirmed. Even though from the numerical modeling no reflection could be interpreted yet, the modeled wavefield has proven helpful to support the results provided by the anisotropic ray tracer.

In order to process the data as in the previous chapters (identification of reflections, imaging of reflective areas, interpretation of the reflection coefficient from the recorded waveforms) other studies have to be undertaken first:

- An improved velocity model is needed. Until now, a VTI medium was considered. However, Yu and Shapiro (2015) suggest orthorhombic anisotropy. The velocity model would strongly influence the modeled wavefield and thus its interpretation.
- A re-location of the events with an updated velocity model is required. The location of the events influences the travel times and thus interpretable signatures within the wavefield. Additionally, for the calculation of correction terms of the apparent reflection coefficient, a precise location is required.
- The effects of an anisotropic source or isotropic source in an anisotropic medium have to be studied in order to understand the amplitude effects of the emitted waves. These amplitudes play a role for the correction terms and, even more crucial, in the determination of the fault plane solutions.

Once the mentioned studies are performed, the recorded wavefields of this microseismic data set can be evaluated in terms of reflection coefficients. However, the recorded waveforms are rich on information. A quantitative evaluation of reflected waves would help to characterize the reservoir and the processes before, during, and after the hydraulic stimulation. The forward modeling has shown as a helpful tool in the pre-examination of the microseismic event situation and can be helpful in further studies.

7. Summary and Conclusion

In this thesis I present a formula to compute reflection coefficients at thin fluid-filled cracks in an elastic medium. The reflection coefficient depends on the reflection angle, the properties of the fluid, and on the elastic properties of the background rock. Even very thin layers (width $\ll$ wavelength) can produce remarkably high reflection coefficients. Thus small scale fractures leave their signatures in microseismic event recordings. These seismic signatures can be identified and evaluated in terms of fracture properties. This helps to characterize the subsurface.

The evaluation of microseismic data sets for reflection coefficients was performed in several steps. First, the theoretical formula was compared to numerical modeling results. Different acquisition geometries from zero incidence to arbitrary receiver source combinations were calculated, and were shown to have a good agreement to theoretical values. In the next step, I analyzed the seismic reflections in the Basel EGS. The acquisition geometry of the EGS is comparably simple. Six receivers recorded microseismic events from around the injection borehole. The velocity model consists of two layers. The upper layer is a sedimentary layer containing the majority of the recording instruments, the lower layer is a granitic layer in which one station is deployed. At this station multiplet events were detected. These events are clustered in space and exhibit similar radiation patterns. This means, that their rays travel similar ray paths and thus illuminate similar structures. I then selected a cluster of events with a significant reflection within the recorded wavefield. The reflection was imaged and revealed a structure in the vicinity of the borehole. With this location knowledge, I could then derive the amplitude correction terms, which incorporate source and travel path effects. And thus correct the apparent reflection coefficient, to a true reflection coefficient. The true reflection coefficient was compared to theoretical values, and I inferred an effective fracture width for the imaged structure. The procedure was successfully repeated for other clusters, and a map of reflectors with their corresponding effective width was obtained.

Next the procedure was applied to natural occurring seismicity. The target area was the San Andreas Fault Observatory at Depth data. Microseismic events were recorded with a downhole receiver array. The waveforms contain seismic signatures of a reflector crossing the array which is in agreement with

the seismic imaging results of Reshetnikov et al. (2010a). To obtain a first estimate of the reflection coefficient, I simplified the velocity model to a single homogeneous and isotropic velocity layer. A source mechanism for a single event and a first approximation for the correction terms were obtained. In contrast to the previous case, a single event was evaluated which gives slightly changed correction terms for each event-receiver-configuration. I determined a first estimate of the reflection coefficient. But since only a single event was evaluated, the accuracy of the estimate for the reflector width is low. The high reflection coefficient is caused by the high velocity contrast of the fracture. This suggests that the fracture, most likely a subsurface strand of the Buzzard Canyon Fault, is fluid-filled or contains a dense network of fluid-filled cracks. However, for the Buzzard Canyon Fault, no indications of the presence of fluids have been reported yet. To produce these observed seismic signatures a high contrast of elastic properties is required, and this motivates a detailed examination of this fault zone. In order to retrieve more information about this fault from the current data set, a refinement of the velocity model, and the evaluation of further events is necessary.

Especially in shale, a high degree of anisotropy makes the interpretation of seismic data more difficult. My last chapter deals with data acquired in shale in the Horn River Basin which exhibits extremely high anisotropy. The recorded data is rich in information, and contain several reflections. Through analysis I partially explain the influence of anisotropy on the propagation of the wavefield. First, I modeled the wavefield for a single homogeneous anisotropic velocity layer using the degree of anisotropy provided by the block velocity model. The shear wave splitting in these waveforms is very large for a single layer. I investigated the influence of the interfaces between several velocity layers. This shows that the contrast between adjacent layers produces significant reflections and conversions which should not be confused with reflections at fractures. In a final modeling experiment I incorporate a refined and smoothed velocity model. Even though the model is smoothed, high reflections and significant conversions from velocity contrasts still occur. Moreover, due to a low velocity zone, multipath shear waves make the identification of reflections within the data even more complex. With this degree of complexity and using only the simple velocity model, it was not possible to extract the reflection coefficients. However, this numerical study serves as a pre-examination and I suggest several steps for how to proceed to estimate reflection coefficients.

In this thesis I introduce a procedure for the estimation of reflection coefficients:

- Identification of reflected phases within waveforms
- Imaging of reflected phases
- Calculation of *apparent* reflection coefficient

- Correction for geometrical spreading, radiation pattern, and attenuation
  $\rightarrow$ *true* reflection coefficient

- Comparison to theoretical reflection coefficient
  $\rightarrow$ reflector width

This procedure was applied to the simplest case of an isotropic and homogeneous background rock, as well as a high quality data set which recorded hydraulically induced microseismic events. For a more complex acquisition geometry and a sparse event distribution, I make a preliminary estimate of the reflection coefficient. For an anisotropic and layered velocity model I performed a numerical study as a pre-requisite for waveform interpretation.

The described procedure is demonstrated in simple cases, but is also applicable to more complex experiments. Monitoring of specific experiments, could be enhanced by automation of this procedure.

The quantitative evaluation of reflections within recorded waveforms is also applicable to laboratory experiments. Place et al. (2016) replicate a hydraulic fracture using two steel plates which have a P wave velocity comparable to the velocity within granite. The void between both plates is filled with air, water, and grouts of different mixtures. Ultrasonic P wave reflections are recorded under the constrained geometrical setup, and are then compared to the analytical solution presented in Chapter 2. The authors find the values in good agreement, and use the resulting reflection coefficient to retrieve the nature of the fluid infill.

In this work, I demonstrate two main points:

(i) From a single hydraulic fracture, significant reflections can occur even if the fracture width is much smaller than the wavelength of the incident wave. This allows the imaging of the fracture.

(ii) Additionally it is feasible to quantitatively evaluate the reflections and estimate reservoir properties using the determined value of reflectivity.

Both of these insights allow us to further characterize the subsurface.

List of Figures

List of Tables

Bibliography

Aki, K. and Richards, P. G. (2002). *Quantitative Seismology*. University Science Books, 2 edition.

BGR (2015). Reserven, Resourcen und Verfügbarkeit von Energierohstoffen. In *Energiestudie 2015*, pages –172. Hannover.

Biot, M. (1956). Theory of propagation of elastic waves in a fluid-saturated porous solid. i low-frequency range. *THE JOURNAL OF THE ACOUSTICAL SOCIETY OF AMERICA*, 28(2):186–178.

BMWi, O. (2014). Bundesbericht Energieforschung 2014. *Forschungsförderung für die Energiewende*.

BMWi, O. (2015). Vierter Monitoring-Bericht zur Energiewende. *Die Energie der Zukunft*.

Buske, S., Gutjahr, S., and Sick, C. (2009). Fresnel volume migration of single-component seismic data. *Geophysics*, 74(6):WCA47–WCA55.

Chavarria, J. A., Malin, P., Catchings, R. D., and Shalev, E. (2003). A look inside the san andreas fault at parkfield through vertical seismic profiling. *Science*, 302:1746–1748.

Dyer, B., Schanz, U., Ladner, F., Häring, M., and Spillman, T. (2008). Microseismic imaging of a geothermal reservoir stimulation. *The Leading Edge*, 27(7):856–869.

Fehler, M. (1982). Interaction of seismic waves with a viscous liquid layer. *Bulletin of the Seismological Society of America*, 72(1):55–72.

GNS Science (2011). M 6.3, Christchurch, 22 February 2011. `http://info.geonet.org.nz/display/quake/M+6.3%2C+Christchurch%2C+22+February+2011` . [Accessed: 14.07.2016].

Grechka, V. (2009). *Applications of Seismic Anisotropy in the Oil and Gas Industry*. EAGE Publications bv. 978-90-73781-68-9.

Grechka, V., Bakulin, A., and Tsvankin, I. (2000). Estimation of fracture parameters from reflection seismic data - Part I: HTI model due to a single fracture set. *Geophysics*, 65:1788–1802.

Groenenboom, J. and Fokkema, J. (1998). Monitoring the width of hydraulic fractures with acoustic waves. *Geophysics*, 63:139–148.

Hajati, T., Langenbruch, C., and Shapiro, S. A. (2015). A statistical model for seismic hazard assessment of hydraulic-fracturing-induced seismicity. *Geophysical Research Letters*, 42(24):10,601–10,606. 2015GL066652.

Hardebeck, J. L. and Shearer, P. M. (2003). Using s/p amplitude ratios to constrain the focal mechanisms of small earthquakes. *Bulletin of the Seismological Society of America*, 93(6):2434–2444.

Häring, M. O., Schanz, U., Ladner, F., and Dyer, B. C. (2008). Characterisation of the Basel 1 enhanced geothermal system. *Geothermics*, 37(5):469–495.

Hummel, N. and Shapiro, S. A. (2013). Analysis and Interpretation of Hydraulic Fracturing Induced Seismicity from the Horn River Basin. In *PHASE Annual Report 2013*.

Korneev, V. (2010). Low-frequency fluid waves in fractures and pipes. *Geophysics*, 75(6):N97–N107.

Korneev, V., Goloshubin, G., Bakulin, A., Troyan, V., Maximov, G., Molotkov, L., Frehner, M., Shapiro, S., and Shigapov, R. (2012). Krauklis wave - half a century after. In *5th Saint-Petersburg International Conference & Exhibition 2012 Saint-Petersburg, Extended Abstract*.

Krauklis, P. (1962). About some low frequency oscillations of a liquid layer in elastic medium. *PMM*, 26(6):1111–1115. In Russian.

Krüger, O., Saenger, E., and Shapiro, S. (2005). Scattering and diffraction by a single crack: an accuracy analysis of the rotated staggered grid. *Geophysical Journal International*, 162:25 – 31.

Kummerow, J. (2010). Using the value of the crosscorrelation coefficient to locate microseismic events. *Geophysics*, 75:MA47–MA52.

Kummerow, J., Reshetnikov, A., Häring, M., and Asanuma, H. (2012). Distribution of the vp/vs ratio within the basel 1 geothermal reservoir from microseismic data. In *74th EAGE Conference and Exhibition incorporating EUROPEC 2012*. EAGE.

Kummerow, J., Shapiro, S. A., Asanuma, H., and Häring, M. (2011). Application of an arrival time and cross correlation value-based location algorithm to the basel microseismic data. In *Extended Abstracts DVD of the 73rd EAGE Conference & Exhibition incorporating SPE EUROPEC*, page Artikel Nr. P193 (5 S.). EAGE Publications bv.

L. M. Brekhovskikh and O. A. Godin (1990). *Acoustics of Layered Media I*. Springer, 2nd edition.

Langenbruch, C. and Shapiro, S. A. (2015). Quantitative analysis of rock stress heterogeneity: Implications for the seismogenesis of fluid-injection-induced seismicity. *Geophysics*, 80(6):WC73–WC88.

Lombard, B. and Piraux, J. (2006). Numerical modeling of elastic waves across imperfect contacts. *SIAM journal on scientific computing*, 28:172–205.

Nagy, P. B. (1992). Ultrasonic classification of imperfect interfaces. *Journal of Nondestructive Evaluation*, 11:127–139.

Place, J., Ghafar, A. N., Malehmir, A., Draganovic, A., and Larsson, S. (2016). On using the thin fluid-layer approach at ultrasonic frequencies for characterising grout propagation in an artificial fracture. *International Journal of Rock Mechanics and Mining Sciences*, 89:68 – 74.

Pod'yapolsky, G. S. (1963). Reflection and refraction at a nonrigid boundary between two elastic media. *Izvestiya AN USSR, Physics of Earth*, 4:525–531. In Russian.

Pyrak-Nolte, L. J., Myer, L. R., and Cook, N. G. W. (1990). Transmission of Seismic Waves across Single Natural Fractures. *Journal of Geophysical Research*, 95, B6:8617–8638.

Quintal, B., Schmalholz, S. M., and Podladchikov, Y. Y. (2009). Low-frequency reflections from a thin layer with high attenuation caused by interlayer flow. *Geophysics*, 74(1):N15–N23.

R. Sutherland et al. (2007). Do great earthquakes occur on the Alpine Fault in central South Island, New Zealand? In Okaya, D., Stern, T., and Davey, F. J., editors, *A Continental Plate Boundary: Tectonics at South Island, New Zealand, Geophys. Monogr. Ser.*, volume 175, pages 235–251. AGU, Washington, D. C.

Rentsch, S. (2007). *A Migration-type Approach for the fast Location of Seismicity: Theory and Applications*. PhD thesis, Berlin, Freie Universität Berlin, Diss., 2007.

Rentsch, S., Buske, S., Gutjahr, S., Kummerow, J., and Shapiro, S. A. (2010). Migration-based location of seismicity recorded with an array installed in the main hole of the san andreas fault observatory at depth (safod). *Geophysical Journal International*, 182:477 – 492.

Reshetnikov, A. (2013). Ray tracing for microseismic monitoring in strongly anisotropic media. In *PHASE Annual Report 2013*.

Reshetnikov, A., Buske, S., and Shapiro, S. A. (2010a). Seismic imaging using microseismic events: Results from the San Andreas Fault System at SAFOD. *Journal of Geophysical Research*, 115.

Reshetnikov, A., Kummerow, J., Asanuma, H., Häring, M., and Shapiro, S. A. (2015). Microseismic reflection imaging and its application to the basel geothermal reservoir. *GEOPHYSICS*, 80(6):WC39–WC49.

Reshetnikov, A., Kummerow, J., Buske, S., and Shapiro, S. A. (2010b). Microseismic imaging from a single geophone: KTB. *SEG Expanded Abstracts 29*, 2070.

Reshetnikov, A. and Shapiro, S. (2015). Using multipath shear wave arrivals for enhanced microseismic location in strongly anisotropic shale. In *77th EAGE Conference and Exhibition 2015*.

Rusu, A. (2012). Processing of microseismic data for imaging the basel geothermal reservoir. Master's thesis, Berlin, Freie Universität Berlin, BSc., 2012.

Saenger, E. H. (2000). *Wave Propagation in Fractured Media: Theory and Applications of the Rotated Staggered Finite-Difference Grid*. PhD thesis.

Saenger, E. H. and Bohlen, T. (2004). Anisotropic and viscoelastic finite-difference modeling using the rotated staggered grid. *Geophysics*, 69(2):583–591.

Saenger, E. H., Gold, N., and Shapiro, S. A. (2000). Modeling the propagation of elastic waves using a modified finite-difference grid. *Wave Motion*, 31(1):77–92.

Schoenberg, M. (1980). Elastic wave behavior across linear slip interfaces. *Journal of the Acoustical Society of America*, 68(5):1516–1521.

Shapiro, S. A., Dinske, C., Langenbruch, C., and Wenzel, F. (2010). Seismogenic index and magnitude probability of earthquakes induced during reservoir fluid stimulations. *The Leading Edge*, 29(3):S. 304–309.

Shapiro, S. A., Rothert, E., Rath, V., and Rindschwentner, J. (2002). Characterization of fluid transport properties of reservoirs using induced microseismicity. *Geophysics*, 67:212–220. Best Paper in Geophysics 2002.

Shearer, P. M. (2009). *Introduction to seismology*. Cambridge University Press.

Soma, N., Niitsuma, H., and Baria, R. (2000). Estimation of deep subsurface structure in european hot dry rock test site, soultz-sous-forêts, france, by use of the reflection method. In *Twenty-Fifth Workshop on Geothermal Reservoir Engineering, Stanford University, Stanford California, January 24-26, 2000*.

Stuermer, K., Kummerow, J., and Shapiro, S. A. (2011). Waveform similarity analysis at cotton valley, texas. *SEG, Expanded Abstracts*, 30:1669–1673.

Thomsen, L. et al. (2002). *Understanding seismic anisotropy in exploration and exploitation*, volume 5. Society of Exploration Geophysicist.

Tleukenov, S. K. (1991). Contact conditions of elastic media with a thin interlayer. *Journal of Mathematical Sciences*, 55:1763–1766.

USGS (2015a). Magnitude 7.0 - HAITI REGION. `http://earthquake.usgs.gov/earthquakes/eqinthenews/2010/us2010rja6/us2010rja6.php`. [Accessed: 14.07.2016].

USGS (2015b). Magnitude 8.8 - OFFSHORE BIO-BIO, CHILE. `http://earthquake.usgs.gov/earthquakes/eqinthenews/2010/us2010tfan/us2010tfan.php`. [Accessed: 14.07.2016].

XKCD (2016). XKCD - A webcomic of romance, sarcasm, math, and language. `http://xkcd.com/1662`. [Accessed: 23.08.2016].

Yu, C. and Shapiro, S. A. (2015). Rock physics constrained estimation of shale anisotropy for microseismic processing - from vti to orthorhombic. In *Extended Abstracts DVD of the 77th EAGE Conference & Exhibition incorporating SPE EUROPEC*, page We P507. EAGE Publications bv.

Zillmer, M., Müller, G., and Stiller, M. (2002). Seismic reflections from the crystalline crust below the continental deep drilling site ktb: Modeling and inference on reflector properties. *Journal of Geophysical Research: Solid Earth*, 107(B9):ESE 2–1–ESE 2–15. 2180.

Zoback, M., Hickman, S., and Ellsworth, W. (2010). Scientific Drilling Into the San Andreas Fault Zone. *EOS*, 91:197–204.

Zoback, M., Hickman, S., and Ellsworth, W. (2011). Scientific Drilling Into the San Andreas Fault Zone – An Overview of SAFOD's First Five Years. *Scientific Drilling*, 11:14–28.

Publications and Conference Abstracts

Some of the presented ideas and illustrations have appeared previously in the following publications or conference abstracts:

Oelke, A., Alexandrov, D., Abakumov, I., Shigapov, R., Kashtan, V. N. T., M., B., and Shapiro, S. A. (2012a). Full Solutions for Reflection and Conversion Coefficients at a Thin Fluid Layer Representing a Hydraulic Fracture. In *5th Saint-Petersburg International Conference & Exhibition 2012 Saint-Petersburg, Extended Abstract*, page P069.

Oelke, A., Alexandrov, D., Abakumov, I., Troyan, V., Kashtan, B. M., and Shapiro, S. A. (2011a). Reflection Coefficients at a Thin Fluid Layer as a Model of a Hydraulic Fracture. In *Extended Abstracts DVD of the 73rd EAGE Conference & Exhibition incorporating SPE EUROPEC*, page Artikel Nr. P353 (5 S.). EAGE Publications bv.

Oelke, A., Alexandrow, D., Abakumov, I., Glubovskikh, S., Shigapov, R., Krüger, O. S., Kashtan, B., Troyan, V. N., and Shapiro, S. A. (2013a). Seismic Reflectivity of Hydraulic Fractures Approximated by Thin Fluid Layers. *Geophysics*, 78(4):T79–T87.

Oelke, A., Bannister, S. C., and Buske, S. (2011b). Seismic Imaging of the Alpine Fault at Whataroa (NZ). In *Abstract T13G-06 presented at 2011 Fall Meeting, AGU, San Francisco, Calif., 5-9 Dec.*, page G6.

Oelke, A., Buske, S., and Bannister, S. (2010). Seismic Imaging of the Alpine Fault, New Zealand, at Whataroa River. In *14^{th} International Symposium on Deep Seismic Profiling of the Continents and their Margins: Program and Abstracts. Geoscience Australia, Record 2010/24*, page 94. D. M. Finlayson.

Oelke, A., Gutjahr, S., Kummerow, J., Reshetnikov, A., Asanuma, H., Häring, M., and Shapiro, S. (2016a). Fracture Zone Characterization by Quantitative Analysis of Reflected Phases from Microseismic Waveform Data. In *78th EAGE Conference and Exhibition 2016, Extended Abstract*.

Oelke, A., Gutjahr, S., Kummerow, J., Reshetnikov, A., and Shapiro, S. (2016b). Bruchzonen-Charakterisierung Mithilfe Quantitativer Auswertung Reflektierter Mikroseismischer Wellenformen. In *76. Jahrestagung der Deutschen Geophysikalischen Gesellschaft*.

Oelke, A., Gutjahr, S., Kummerow, J., Reshetnikov, A., and Shapiro, S. A. (2015). Reflection Coefficient Estimates at the Basel EGS. In *75. Jahrestagung der Deutschen Geophysikalischen Gesellschaft*, page 267.

Oelke, A., Krueger, O. S., and Shapiro, S. A. (2014a). Modeling Wave Propagation of Microseismic Events in Anisotropic Media. In *76th EAGE Conference and Exhibition 2014, Extended Abstract*.

Oelke, A., Krüger, O. S., and Shapiro, S. A. (2013b). 3-D Modeling of Reflection Coefficients at Thin Fluid Layers Representing a Hydraulic Fracture. In *75th EAGE Conference & Exhibition incorporating SPE EUROPEC 2013 London, Extended abstract*.

Oelke, A., Krüger, O. S., and Shapiro, S. A. (2014b). Modeling Wave Propagation in Anisotropic Media. *DGG 74. Jahrestagung der Deutschen Geophysikalischen Gesellschaft, Karlsruhe, Germany*, page 203.

Oelke, A., Krüger, O. S., Shapiro, S. A., and Abakumov, I. (2012b). Modeling Reflection Coefficients at a Thin Fluid Layer Representing a Hdraulic Fracture. In *SEG Technical Program Expanded Abstracts 2012: pp. 1-5*.

Shigapov, R., Oelke, A., Troyan, V. N., Kashtan, B. M., and Shapiro, S. A. (2012). Approximate Reflection Coefficients at a Fracture for Microseismic Needs. In *5th Saint-Petersburg International Conference & Exhibition 2012 Saint-Petersburg, Extended Abstract*, page P068.

Danksagung

Vielen Dank all denjenigen Menschen, die mich direkt oder indirekt bei der Entstehung dieser Arbeit unterstützt haben.

Mein herzlicher Dank gilt Herrn Professor Dr. Serge Shapiro, der mir diese Arbeit ermöglicht hat, für seine Betreuung, seine Anregungen und seine Unterstützung im gesamten Entstehungszeitraum der Arbeit.

Herrn Professor Dr. Shapiro sowie Herrn Professor Dr. Marco Bohnhoff möchte ich für die Begutachtung dieser Arbeit danken.

Für den nicht nur finanziellen Support über drei Jahre danke ich der Graduate School GEOSIM. Ebenso waren der fachübergreifende und auch außerfachliche Austausch sowie die Teilnahme an verschiedenen Workshops immer wieder spannend. Weiterhin danke ich dem *Phase*-Konsortium für die finanzielle Unterstützung. Diese hat mir auch den Besuch vieler interessanter Fachtagungen ermöglicht, was für mich immer sehr bereichernde Erfahrungen waren.

Mein Dank gilt auch meinen Kolleg*innen für das gute Umfeld: "meinen (Ex-) Roomies" Jonas Folesky und Wasja Bloch, Oliver Krüger und Jörn Kummerow, Stine Gutjahr und Karsten Stürmer, Carsten Dinske und Cornelius Langenbruch, 'Slava' Viacheslav und Anton Resehtnikov und vielen weiteren nicht namentlich erwähnten Menschen, denen ich im Zusammenhang mit der Geophysik immer wieder gerne begegnet bin. Mit Freude habe ich auch zusammen mit den *Phasers* am Geo-Soccer-Cup Lankwitz teilgenommen.

Vielen Dank an Chris, Jonas, Jörn und Wasja für das Korrekturlesen einzelner oder aller Passagen dieser Arbeit.

Natürlich haben mich auch außerhalb von Lankwitz viele Menschen auf meinem Weg begleitet und immer unterstützt. Diese Personen werde ich nicht im Einzelnen aufzählen, denn sie wissen, dass sie gemeint sind, sondern sage kurz und bündig: meiner Familie und meinen Freunden sei mein herzlichster Dank ausgesprochen!

Curriculum Vitae

“Der Lebenslauf ist in der Online-Version aus Gründen des Datenschutzes nicht enthalten.“

“Der Lebenslauf ist in der Online-Version aus Gründen des Datenschutzes nicht enthalten.“

Something funny in the end...

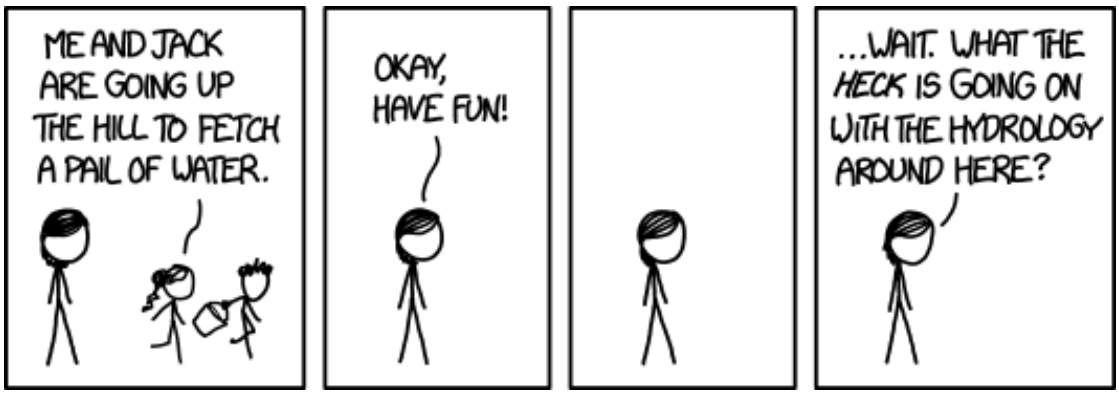

"Jill and Jack / began to frack. / The oil boosts their town. / But fractures make / the bedrock shake / and Jack came tumbling down." (XKCD, 2016).